Building a Sustainable Future through the Material design of
3D Printed Polymer Materials

by

Vinita Vinod Shinde

A dissertation submitted to the Graduate Faculty of
Auburn University
in partial fulfillment of the
requirements for the Degree of
Doctor of Philosophy

Auburn, Alabama
May 7, 2022

Keywords: Self-healing, Microcapsules, Additive manufacturing
Stereolithography, Fused Filament Fabrication, Polymers, Porous media

Approved by

Bryan S. Beckingham, Assistant Professor of Chemical Engineering, Auburn University
Virginia A. Davis, Alumni Professor of Chemical Engineering, Auburn University
Maria L. Auad, Professor of Chemical Engineering, Auburn University
Asha-Dee N. Celestine, Assistant Professor of Aerospace Engineering, Auburn University
Lauren E. Beckingham, Reader, Assistant Professor of Civil and Environmental Engineering,
Auburn University

Abstract

3D printing technologies are coming to the forefront of scientific, industrial, and public attention as it allows customized manufacturing of complex parts with a high degree of control over design, processing parameters, and time. However, compared to parts fabricated by traditional methods, 3D printed composites typically show poorer mechanical strength and thereby increased potential for material damage and failure during fabrication and use. Here, we incorporate self-healing properties towards extending the lifetimes of 3D printed polymeric objects. Inspired by biological self-healing, in which a damage event triggers an autonomic healing response, microcapsules containing healing agents can be embedded into a host material. During a damage event, these microcapsules rupture, release the healing agent, and heal the surrounding material by polymerization, entanglement, or cross-linking. Double shell wall polyurethane/poly-(urea-formaldehyde) microcapsules are synthesized by in-situ-interfacial polymerization. Microcapsules with solvent and monomer core fluids are prepared to investigate solvent-healing and monomer self-healing mechanisms. Microcapsules containing healing agents are either incorporated into the host polymer matrix or are coated onto 3D printing polymer filaments to create 3D printed objects capable of self-healing. Microcapsule distribution within composites is visualized using X-ray Nano-CT imaging. Microcapsule survivability and self-healing properties of these composite materials after 3D printing are evaluated via examining the healing efficiency and mechanical strength of the 3D printed objects. These results lay the foundation for including self-healing behavior into 3D printed polymer composites. Additionally, the application of 3D printing as a platform for geoscience applications by using a variety of polymer materials to replicate reactive porous media samples is investigated towards understanding of subsurface systems towards improving the human and planetary conditions in the future.

2

Table of Contents

List of Figures

10

List of Abbreviations

σ_f	Flexural Stress
δ_x	Solubility Parameter
ABS	Acrylonitrile butadiene styrene
AM	Additive Manufacturing
ATR-FTIR	Attenuated Total Reflectance-Fourier Transform Infrared
CAD	Computer-aided Design
$CaCO_3$	Calcium carbonate
$Ca_3(PO_4)_2$	Calcium phosphate
$CaSO_4$	Calcium sulfate
$CDCl_3$	Deuterated chloroform
CO_2	Carbon dioxide
CT	Computed Tomography
CV	Coefficient of Variance
DCPD	Dicyclopentadiene
DMA	Dynamic Mechanical Analysis
DMSO	Dimethyl sulfoxide
DSC	Differential Scanning Calorimetry
DTS	Direct Tensile Strength
E'	Storage Modulus
EMA	Ethylene-maleic-anhydride
EMAA	Poly(ethylene-co-methacrylic acid)
EPA	Ethyl phenylacetate
FFF	Fused Filament Fabrication

FTIR	Fourier Transform Infrared
HIPS	High Impact Polystyrene
IR	Infrared
$K_{Q, healed}$	Fracture Toughness of the healed material
$K_{Q, virgin}$	Fracture Toughness of the virgin material
$NaHCO_3$	Sodium bicarbonate
NaOH	Sodium hydroxide
NMR	Nuclear Magnetic Resonance
PAAm	Polyacrylamide
PDMS	Poly(dimethylsiloxane)
PLA	Poly(lactic acid)
PPM	Parts Per Million
PU	Polyurethane
PU-UF	Polyurethane- Poly (urea-formaldehyde)
ROMP	Ring Opening Metathesis
SEM	Scanning Electron Microscopy
SENB	Single Edge Notch Bean\m
SLA	Stereolithography
SLS	Selective Laser Sintering
T_g	Glass Transition Temperature
TGA	Thermogravimetric Analysis
THF	Tetrahydrofuran
UCS	Unconfined Compressive Strength
UV	Ultraviolet
XRD	X-ray Diffraction
X-ray Nano CT	X-ray Nano Computed Tomography

Chapter 1

Introduction

Chapter 1 Introduction

Polymers are materials made of many small molecules called monomers covalently linked together to form long chain molecules of high molecular weight [1]–[3]. Goods and products made from polymers are present all around us: polyurethane foam cushions, polyethylene cups, cloths of synthetic fiber, acrylic paints and many more and thus, they have huge impact on our lives [4], [5]. However, high strength and stiffness equivalent to that of metal products is desirable for some applications in aerospace, automotive, marine, electronics and biomedical industries while maintaining the lower density of polymer materials [6]–[8]. This is where a key advantage of polymer composites comes into play. Polymer composites are multi-material systems where reinforcing additives are included within polymer matrices to achieve synergistic properties of both polymer and the reinforcing material [9]. Thus, polymer composites are an increasingly popular choice for structural applications due their high modulus, light weight, and excellent performance.

In addition, additive manufacturing also known as 3D printing of polymer composites has recently shown dramatic increase in both attention and industrial applications. The expansion of interest is driven by its high degree of customization, ability to construct complex designs and due to decreasing costs of 3D printing materials and equipment [10], [11]. Two popular choices of 3D

printing techniques for polymer materials are: stereolithography (SLA) and fused filament fabrication (FFF). FFF utilizes a polymer filament or wire that is extruded through a hot nozzle in a layer-by-layer fashion to print an object from a 3D model and has found increasing application for rapid prototyping. SLA also builds an object layer-by-layer but does so by using photopolymerization. During SLA a beam of light is focused to a spot within a liquid resin bath where it causes a reaction that forms the solid polymer. By controlling the light position and resin chemistry, desired objects are printed from this liquid resin bath into the final solid object. SLA printing has high resolution and excellent surface finish. However, 3D printing of polymer materials remains somewhat limited due to limitations in mechanical properties and functionalities of fabricated parts [12], [13]. Also, many of the polymer material options for 3D printing are not intrinsically recyclable requiring disposal if they suffer any damage. During daily usage, polymer materials face mechanical stresses, atmospheric oxygen, and moisture, etc., all of which can lead to damage in the materials [14]. In nature, biological systems overcome these issues by using self-healing as their strategy to heal the injuries [15]. Thus, taking inspiration from nature, here, we aim to integrate self-healing properties with polymeric materials to extend lifetime of 3D printed composite materials [16].

Another area where researchers in the geosciences have been using 3D printing to fabricate porous media replicating the physical, hydraulic, mechanical and chemical properties of natural samples. A wide variety of materials, including thermoplastics polymers, photosensitive epoxy resin, etc., and printing methods have been explored to fabricate complex porous structures. So, here we also aim to evaluate the rock sample replicate's mineral reaction and precipitation within the porous structures using different 3D printing methods, mimicking geochemical reactions from geochemical systems.

1.1. Objectives

1.1.1. Stereolithography (SLA) 3D printing of Self-healing Polymer Composites

Polymer-based components manufactured by stereolithographic-based (SLA) 3D printing tend to show relatively poor mechanical strength compared to polymer-based components fabricated by conventional methods such as compression molding. Some of this difference is tied to the thermoset nature of typical SLA 3D printed materials, where high cross-linking density and brittle material behavior can result in catastrophic material failure, limiting the lifespan of SLA 3D printed composite materials. Previous studies have investigated potential techniques for improving mechanical strength of SLA 3D printed polymer components such as the addition of various strengthening fillers, however, few studies have investigated incorporation of self-healing materials for SLA 3D printing to extend material lifetimes. In this dissertation, the use of a microcapsule-catalyst self-healing system in conjunction with commercially available photocurable resin towards increasing SLA 3D printed specimen lifetime and material sustainability is investigated. Microcapsules filled with healing fluids are synthesized using in situ interfacial polymerization and dispersed in commercial resin prior to SLA 3D printing of self-healing composite specimens. The ability of these microcapsules to survive the SLA 3D printing process intact is demonstrated and X-ray nano-CT imaging shows microcapsules to be distributed throughout printed specimens. The self-healing behavior of these SLA 3D printed composite materials is evaluated via quantification of mechanical properties, and healing efficiency. Overall, this is a facile and promising approach for incorporation of self-healing behavior into SLA 3D printing resins.

1.1.2. Self-healing of High Impact Polystyrene Composites

Polymer composites are widely used in many industries due to their desirable, and commonly superior properties. However, the replacement of damaged composite materials can be very costly and time-consuming, motivating the development of self-healing composites that recover their properties after a damage event. This work demonstrates the microcapsule-based self-healing of compression molded thermoplastic high impact polystyrene (HIPS) composites using a non-toxic and environmentally friendly solvent, ethyl phenylacetate (EPA). EPA is incorporated within double-walled polyurethane-poly(urea-formaldehyde) (PU-UF) microcapsules which are then integrated within the HIPS specimens. Flexure and fracture behavior, with and without microcapsules, is used to investigate the microcapsules' impact on composite physical properties and to determine the composite's self-healing efficiency (up to 64%) after healing in response to fracture. Overall, this work demonstrates the inclusion of self-healing properties in a commercially important polymer material with a non-toxic and environmentally friendly solvent and motivates further development of thermoplastic self-healing composites for industrial applications.

1.1.3. Fused Filament Fabrication of Self-healing Polymer Composites

Fused filament fabrication (FFF) is a widely used 3D printing process that is increasingly adopted for prototyping and growing in popularity for manufacturing. Simultaneously, there is increasing consideration of material lifecycles in choosing and designing materials and material processing techniques. One approach to extending material lifetimes is enabling recovery of material properties after damage through autonomous self-healing behavior. Here, we investigate microcapsule-solvent based self-healing of high impact polystyrene, a common thermoplastic polymer, towards increasing FFF printed specimen lifetimes and improving material sustainability.

Microcapsules filled with environmentally friendly ethyl phenylacetate (EPA) are synthesized using in-situ interfacial polymerization and coated on polymer filaments prior to FFF 3D printing. The ability of these microcapsules to survive the FFF 3D printing process is demonstrated and the self-healing behavior of FFF 3D printed composite materials evaluated via quantification of mechanical strength and healing efficiency (up to 81% healing efficiency is achieved).

1.1.4. 3D Printing of reactive porous media

Increased atmospheric carbon dioxide captures outgoing infrared radiation (IR) from Earth's surface, leading to a subsequent increase in near-surface global temperatures. Therefore, scientists are trying various ways to reduce carbon dioxide released into the atmosphere. Geologic carbon sequestration secures carbon dioxide (CO_2) in deep geologic formations to prevent its release to the atmosphere and contributes to climate change and global warming as a greenhouse gas. Geological systems are heterogeneous, containing different layers of rock, differentiating in pores and grains. Hence, to ensure the environmental sustainability of this option, we must understand the rates and mechanisms of essential geochemical reactions. However, understanding the impacts of porous media properties on geochemical reactions is challenging due to the highly heterogeneous nature of rock samples. Therefore, one of the ways to replicate these reactive rock samples and investigate the impact of mineral dissolution and precipitation on porosity and permeability is 3D printing. 3D printing allows customized fabrication of complex 3D parts from X-ray Micro CT images. This study uses the Fused filament fabrication 3D printing approach to fabricate multiple replicates of identical pore structures. Here, to fabricate reactive porous media, the surface functionalization approach is used. High impact polystyrene (HIPS) polymer is used for surface treatment via sulfonation to present sulfonic acid moieties to seed the growth of calcite.

Firstly, fabrication and surface functionalization of 2D polymer films shows the presence of polar groups investigated by ^{1}H-NMR and FTIR spectroscopy. And then, the precipitation of calcite crystals on 2D reactive HIPS films is evaluated by X-ray Nano CT and XRD analysis. This approach is extended to surface functionalization and precipitation of calcite crystals within 3D printed pore structures. Overall, this study provides a platform to use a 3D printing approach for creating reactive rock sample replicates to evaluate mineral reaction and precipitation within porous structures, mimicking geochemical reactions from geochemical systems.

1.2. Organization

In Chapter 2, the necessary background information about types and mechanisms of self-healing materials is presented and discussed in addition to a summary about additive manufacturing technologies, their types and application for self-healing composites and an overview of the research objectives of this dissertation. Also, background information on the use of 3D printing of porous structures is presented. Chapter 3 discusses stereolithography 3D printing of self-healing polymer composites. Chapter 4 discusses the self-healing of high impact polystyrene composites, and Chapter 5 discusses the fused filament fabrication 3D printing for self-healing polymer composites. Chapter 6 discusses the 3D printing of reactive porous media. Lastly, Chapter 7 summarizes conclusions and presents plans for future study.

1.3. References

[1] Ward, M. A.; Georgiou, T. K. Thermoresponsive Polymers for Biomedical Applications. *Polymers (Basel)* **2011**, *3* (3), 1215-1242. https://doi.org/10.3390/polym3031215.

[2] Hou, W.; Xiao, Y.; Han, G.; Lin, J. Y. The Applications of Polymers in Solar Cells: A Review. *Polymers* **2019**, *11*, 143. https://doi.org/10.3390/polym11010143.

[3] Vroman, I.; Tighzert, L. Biodegradable Polymers. *Materials* **2009**, *2*, 307-344. https://doi.org/10.3390/ma2020307.

[4] Ghosh, B.; Urban, M. W. Self-Repairing Oxetane-Substituted Chitosan Polyurethane Networks. *Science* **2009**, *323* (5920), 1458-1460. https://doi.org/10.1126/science.1167391.

[5] Haider, T. P.; Völker, C.; Kramm, J.; Landfester, K.; Wurm, F. R. Plastics of the Future? The Impact of Biodegradable Polymers on the Environment and on Society. *Angewandte Chemie - International Edition*. **2019**, *58*, 50-62 https://doi.org/10.1002/anie.201805766.

[6] Won, J. P.; Kang, H. B.; Lee, S. J.; Kang, J. W. Eco-Friendly Fireproof High-Strength Polymer Cementitious Composites. *Constr. Build. Mater.* **2012**, *30*, 406-412. https://doi.org/10.1016/j.conbuildmat.2011.12.034.

[7] Sukumaran, J.; Pauw, J. De; Neis, P. D.; Tóth, L. F.; De Baets, P. Revisiting Polymer Tribology for Heavy Duty Application. *Wear* **2017**, *376–377*, 1321-1332. https://doi.org/10.1016/j.wear.2017.01.018.

[8] Cullen, D. A.; Neyerlin, K. C.; Ahluwalia, R. K.; Mukundan, R.; More, K. L.; Borup, R. L.; Weber, A. Z.; Myers, D. J.; Kusoglu, A. New Roads and Challenges for Fuel Cells in Heavy-Duty Transportation. *Nature Energy* **2021**, *6*, 462-474. https://doi.org/10.1038/s41560-021-00775-z.

[9] Nurazzi, N. M.; Asyraf, M. R. M.; Khalina, A.; Abdullah, N.; Sabaruddin, F. A.; Kamarudin, S. H.; Ahmad, S.; Mahat, A. M.; Lee, C. L.; Aisyah, H. A.; Norrrahim, M. N. F.; Ilyas, R. A.; Harussani, M. M.; Ishak, M. R.; Sapuan, S. M. Fabrication, Functionalization, and Application of Carbon Nanotube-Reinforced Polymer Composite: An Overview. *Polymers*

2021, *13*, 147. https://doi.org/10.3390/polym13071047.

[10] Han, T.; Kundu, S.; Nag, A.; Xu, Y. 3D Printed Sensors for Biomedical Applications: A Review. *Sensors (Switzerland)* **2019**, *19* (7), 1706. https://doi.org/10.3390/s19071706.

[11] Berman, B. 3-D Printing: The New Industrial Revolution. *Bus. Horiz.* **2012**, *55* (2), 155–162. https://doi.org/10.1016/j.bushor.2011.11.003.

[12] Mwema, F. M.; Akinlabi, E. T. Basics of Fused Deposition Modelling (FDM). In *SpringerBriefs in Applied Sciences and Technology* **2020**, 1–15. https://doi.org/10.1007/978-3-030-48259-6_1.

[13] Arefin, A. M. E.; Khatri, N. R.; Kulkarni, N.; Egan, P. F. Polymer 3D Printing Review: Materials, Process, and Design Strategies for Medical Applications. *Polymers (Basel)* **2021**, *13* (9), 1–24. https://doi.org/10.3390/polym13091499.

[14] Okan, M.; Aydin, H. M.; Barsbay, M. Current Approaches to Waste Polymer Utilization and Minimization: A Review. *Journal of Chemical Technology and Biotechnology* **2019**, *94* (1), 8-21. https://doi.org/10.1002/jctb.5778.

[15] Thomas S; Surendran, A. *Self-Healing Polymer-Based Systems. Elsevier* **2020**. https://doi.org/10.1016/c2018-0-03002-9.

[16] Shinde, V. V.; Celestine, A. D.; Beckingham, L. E.; Beckingham, B. S. Stereolithography 3D Printing of Microcapsule Catalyst-Based Self-Healing Composites. *ACS Appl. Polym. Mater.* **2020**, *2* (11), 5048-5057. https://doi.org/10.1021/acsapm.0c00872.

Chapter 2

Background

Ch. 2 Background

Polymers and polymer composites can suffer damage during the manufacturing process or during their daily usage. There can be many difficulties associated with detecting and repairing composite material damage which can limit their application. To overcome these limitations, self-healing properties may be incorporated in these polymer materials to prevent catastrophic failure, heal minor damage, and extend material lifetimes. In this chapter, different approaches to self-healing are detailed and major prior research on self-healing of polymer materials is reviewed. Also, additive manufacturing of polymer materials using different techniques and previous research on additive manufacturing of self-healing composite is discussed. Finally, the research objectives including self-healing of polymer composites using different fabrication techniques are presented.

2.1. Additive Manufacturing

Polymer and polymer composites can be fabricated using various manufacturing techniques. Conventional methods have limitations over polymers and composites manufacturing due to the need for precise molds for every single design and inability to manufacture complex and customized parts. Additive manufacturing (AM) has key advantages as it allows for production of customized and complex polymer composites parts in an economical way [1]. Additive manufacturing enables the production of complex part geometries generated by computer-aided 3D design with minimal material waste through the additive layer-by-layer fashion of manufacturing [1]–[3]. There are a variety of different additive manufacturing technologies as shown in Figure 1, many of which have found use for rapid prototyping for different industrial applications [4], [5].

	Process	Acronyms	Feedstock	Material	Bonding and join
	Extrusion (or fused filament fabrication or fused deposition modeling)	FFF, FDM	Filament, rod, pellets	Polymer	Fused with heat
	Photopolymerization (or stereolithography)	SLA	Liquid	Photopolymer, metal, ceramics, composite	Cured with laser, projector, UV light
	Material Jetting (or Binder Jetting)	MJ (BJ)	Powder, liquid	Ceramic, wax, polymer, metal, sand	Cured with UV light, heat
	Laminated Object Manufacturing (or Sheet Lamination)	LOM	Sheet	Paper, metal, polymer	Joined with agent, heat and pressure
	Selective Laser Melting	SLM	Powder	Metal	Fused with laser and electron beam
	Directed Energy Deposition	DED, EBM	Wire, powder	Metal	Fused with laser and electron beam
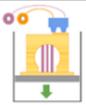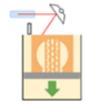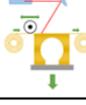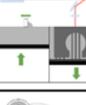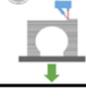
Figure 2.1. Additive manufacturing processes. Reprinted (adapted) with permission from Ref. [5]. Copyright 2020. MDPI Materials.

2.1.1. Types of Additive manufacturing

In this dissertation, we focus on unique applications of 3D printing technologies, and so the following is not focused on reviewing the various 3D printing technologies, however the succeeding sections give a general overview of the primary technologies. For example, selective laser sintering utilizes thermal energy to fuse a material powder into a solid part on a printing bed in successive layers using high temperature laser to construct the structure. This process is perhaps the least utilized for polymer materials, however it has found use for polyamide polymer matrices with different types of fillers. For instance, Goodridge et al. have investigated the impact of carbon nanofibers (CNF) addition on the processing parameters and mechanical properties of laser sintered parts [6]. The second type of additive manufacturing technique is through vat polymerization. UV light is used to cure a photo-resin in a vat using either a laser (stereolithography) or 2D projector (digital light projection) to generate the structural pattern for each layer. These vat photopolymerization techniques are commonly used techniques for printing polymer composites, where polymer matrix materials are usually epoxy resin, polyester resin or acrylate resin [7]–[10]. One advantage of this technology is the high resolution (25-100 μm) and smooth surface finish, which favors its application in constructing smaller and complex devices with high precision. However, one drawback is the rather limited number and type of available resin materials as well as the high cost of high-performance resins.

The third type of process is through material extrusion. In material extrusion, filaments or material paste is extruded through a nozzle, and deposited on a build platform in the form of layers. The first category in the material extrusion is liquid deposition modeling. In liquid deposition modeling, paste or liquid material is stored in syringe and deposited selectively on a build platform based on the target design [1]. Shear thinning behavior is an important feature of

material liquid deposition modeling as the material must be extruded smoothly through the nozzle during the fabrication process but remain in a place once deposited at the target locations [1]. While this technique is often cost effective, it requires specific rheological and viscoelastic properties of the material and agglomeration of the dispersed phase (in the case of composites) can lead to clogging of the nozzle [11]. Alternatively, inkjet printing is a similar process where an ink is released from a nozzle by piezoelectric action where the subsequent evaporation of solvent results in solidification of the material from the ink dispersion [12]. While both ceramic components and complex polymer parts can be fabricated using inkjet printing [13], [14], it also requires tight control over the material dispersion and utilizes delicate extruder heads and expensive ink cartridges [12].

A second category of material extrusion is fused filament fabrication (FFF) or fused filament fabrication (FFF). Fused filament fabrication is a well-known technology for fabrication of prototypes and end-use parts of thermoplastic materials because of its simplicity, reliability, and affordability [15]. In fused filament fabrication, thermoplastic materials are melted and extruded through a nozzle where they subsequently cool and solidify in place to form the targeted structure. A combination of the relatively broad variety of polymer materials and polymer composites compatible with FFF 3D printing, and the fairly low cost of entry level FFF printers has led to the popularity and comparably broader application of FFF 3D printing [16]–[19].

2.2. Materials design for inherent properties

3D printing is a challenging process, as several factors are employed for achieving superior mechanical strength including material design, printing parameters, and post processing. The following summarizes recent research in 3D printing of self-healing polymer composites which allow materials to autonomously recover mechanical strength/toughness in response to a damage event is discussed including different polymer systems and mechanisms used for fabricating self-healing polymer composites.

2.2.1. Self-healing

All engineered materials are susceptible to deterioration, damages, and failure [20]. Damage in a material can occur during the material processing, due to accidental external events or by wear and tear during use [21]. Also, the combined impacts of heat, light, chemical medium, and environmental factors can lead to degradation of materials [22]–[26]. In nature, biological systems address this issue by self-healing, where the overall goal of living systems is to survive and healing is the primary option used by animals and plants [27] –[29]. This influential biological self-healing concept has inspired scientists to incorporate similar functionality within synthetic materials to build "self-healing materials" [24], [25], [30]. Self-healing is an intrinsic ability of a material to repair damage (partially or completely) and recover the lost or degraded physical properties and functional performance of the material using the resources inherently available to the material systems [27], [31], [32]. Self-healing thereby aims to increase the robustness and prolong service life span of a material when repair or replacement of material is economically not affordable, not possible, or unsafe [26]. The following sections describe self-healing polymer systems which repair the injuries without human intervention, as inspired by living materials, and their application to 3D printing of polymer composites [21].

2.2.1.1. Types of Self-healing

Self-healing can either be an autonomous process where external intervention is not required or it can be non-autonomous where external force, heat, [27], [28] organic solvent, [29]–[31] or UV-light [32], [33] is necessary to initiate the process. Autonomous self-healing does not require external stimulus to initiate the healing because the material damage itself is enough to trigger the process [34]–[38]. Autonomous self-healing is valuable in difficult to access environmental conditions such as inside devices like implants, deep sea pipelines, and for aerospace applications [23]. Self-healing systems can be further categorized into two primary conceptual approaches intrinsic and extrinsic. In intrinsic self-healing the material itself incorporates the ability to heal via reversible bonding typically in presence heat or UV-light whereas in extrinsic this ability is incorporated through addition of a second material such as a microcapsule or microvascular network which incorporate the autonomic self-healing ability [21]. The type of self-healing approach and its implementation impact the damaged volume that can be repaired, the repeatability of healing at same location, and the speed at which the healing occurs [21].

2.2.1.1.1. Intrinsic Self-healing

Intrinsic self-healing materials recover from a damage event through inherent reversible bonding or reversible reactions in the polymer matrix [21], [39]. Intrinsic self-healing does not require addition of an external healing agent, avoiding many issues with incorporation of healing systems in the material and their compatibility with the material [21]. One common route to intrinsic self-healing materials is through reversible reactions such as reversible polymerization of crosslinking where the polymer itself can be reversed to their monomeric or un-crosslinked state during the damage event and subsequently repairs itself autonomously or utilizing an external stimuli such as heat or light [40]. Intrinsic self-healing systems are capable of multiple

healing events due to the repeatability of the utilized reversible reactions. However, as intrinsic self-healing systems mostly rely on external stimulus (heat or light) their application space is limited somewhat to material specific temperature windows or application specific accessibility to light [39], [40].

One example of reversible reaction based intrinsic self-healing is through Diels-alder cycloaddition [27], [28], [41]–[45]. Intrinsic self-healing has also been demonstrated utilizing ionomer chemistries such as poly(ethylene-co-methacrylic acid) [46], [47] where thermally assisted ionic interactions near the crack area lead to formation of clusters of ionic segments resulting in self-healing [48]. Additional routes to intrinsic self-healing include incorporation of reversible hydrogen bonds [49],[50] and molecular diffusion [51]. Intrinsic self-healing systems are capable of multiple healing events due to reversible reactions. However, a majority of the studies in intrinsic self-healing systems are limited to thermoplastic polymers which restricts its application for heavy-duty systems due to their low strength, stiffness and low T_g [39]. Intrinsic self-healing systems mostly rely on the external stimulus limiting their application in difficult-to-access conditions [39] motivating future studies developing intrinsic self-healing systems without external stimulus requirement or easily available external stimulus [39].
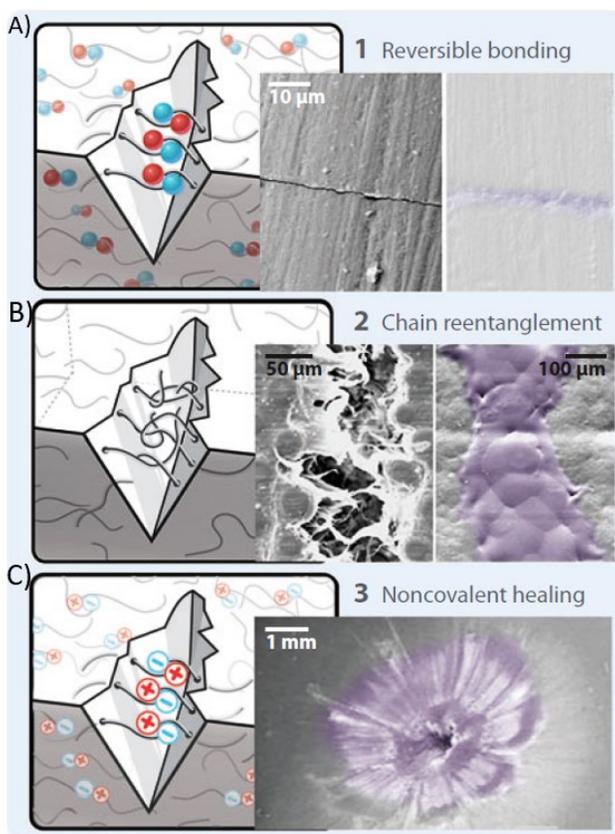
Figure 2.2. Schematic representation of intrinsic self-healing materials: A) Reversible bonding system based on reversible chemical reactions B) Chain entanglement based on structural mobility and entanglement of polymeric chains around the damage area C) Non-covalent healing scheme based on reversible hydrogen bonding, adapted from Blaiszik et al. (2010), Ref. [21]. Copyright 2010 Annual Reviews.

2.2.1.1.2. Extrinsic Self-healing

The type of autonomous healing is extrinsic self-healing, where healing fluids are incorporated in the form of capsules or vascular networks that are isolated in a separate phase from the host material. Extrinsic self-healing system contains encapsulated containers in form of capsules or

vascular networks which release a healing fluid during the crack event and initiates the self-healing process [52], [53].
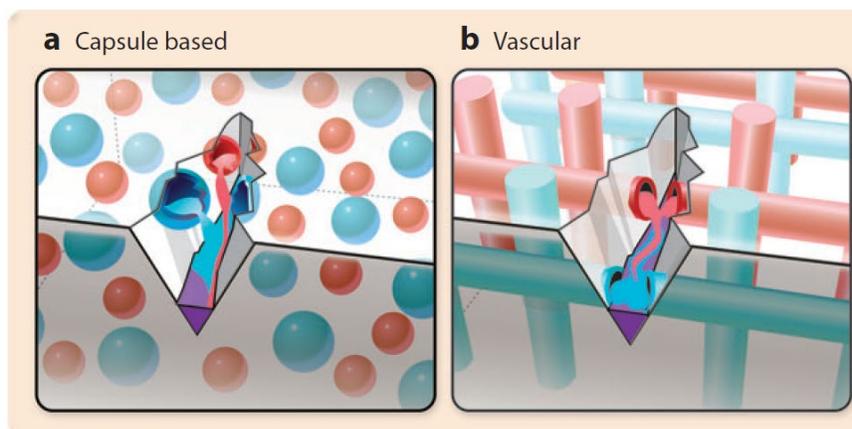
Figure 2.3. Schematic representation of extrinsic self-healing materials: a) Capsule based self-healing materials b) Vascular based self-healing materials, adapted from Blaiszik et al. (2010), Ref. [21]. Copyright 2010 Annual Reviews.

The first category in extrinsic self-healing is capsule based self-healing materials where a healing fluid is stored inside discrete microcapsules [25]. Microcapsules are micron sized particles consisting of one or more core reactive materials surrounded by a single or multiple shell walls [53]. When these capsules are ruptured by a propagating crack, the self-healing process initiates due to the release of healing fluid and subsequent reaction near the crack plane. Microcapsule based self-healing systems are highly localized systems and can heal the crack right where it is initiated, but its main drawback is that it is restricted to single damage event at given site [54]. Additionally, the healing fluid is depleted after this one release, leading to a singular local healing event [55]. Reactive materials are encapsulated using various techniques including in-situ, interfacial polymerization, melt-dispersion or coacervation. In-situ and

interfacial emulsion polymerization are common encapsulation techniques due to their simplified process described below [37], [38], [53].

Microcapsule based self-healing systems can be achieved by different methods for sequestering the healing agent(s). The first is a capsule-catalyst healing system, where the healing fluid is an encapsulated monomer, and a corresponding catalyst is dispersed in the polymer matrix. White et al. [25] demonstrated for the first time dicyclopentadiene (DCPD)-Grubbs' first-generation catalyst based self-healing system based on ring-opening metathesis polymerization. These capsule-catalyst based systems have been incorporated into epoxy matrices [56], [57] and epoxy composites [58] due to ability of poly(dicyclopentadiene) to form cross-linked networks across the damage front leading to high healing efficiency [56]. Another related approach is a multi-capsule system in which both core fluid and catalyst are encapsulated separately and both microcapsules are incorporated in the composite. Multi-capsule self-healing of elastomers has been reported by Keller et al. where platinum catalyst and poly(dimethylsiloxane) (PDMS) monomer were encapsulated separately in different microcapsules and dispersed in PDMS resin matrix to produce a self-healing composite material [59]. Another capsule-based system utilizes a latent functionality of the polymer matrix itself where microcapsules containing healing fluid are dispersed in the polymer matrix and during the crack event, this incorporated functionality initiates the polymerization upon the release of healing fluid. Self-healing coatings are a great example of capsule-based systems utilizing latent functionality [60]. A different approach utilizing a latent system characteristic is solvent-based self-healing [61]. In solvent based self-healing systems, the healing fluid is a solvent that uses its solvation of the bulk polymer to initiate the self-healing. In solvent-based system, a crack in the

polymer matrix releases the solvent to the crack site, locally dissolving the polymer leading to rebonding of crack surfaces of polymer matrix on evaporation of the solvent [62].

The second category in extrinsic self-healing is vascular self-healing materials. Vascular self-healing materials operate analogously to the above-described capsule-based systems, however the store and distribute healing fluid through capillary sized hollow tubes in the form of an interconnected network within the material [63]. For instance, vascular channels can be incorporated using hollow glass fibers [64]. Vascular networks with multiple connectivity have been prepared to have larger accessible reservoir of healing fluid and to attain easier refilling of fluid after depletion [54]. A key advantage of vascular based self-healing system is the ability to achieve repetitive healing of damage events due to high volume fraction of healing fluid and interconnected delivery through the network [65]. However, these systems can also suffer channel blockages that can restrict healing fluid access to new crack sites, fractured channels can lead to large scale leakage that can soften the polymer matrix (plasticization), and incorporation of interconnected vascular networks can be a complex endeavor [65].
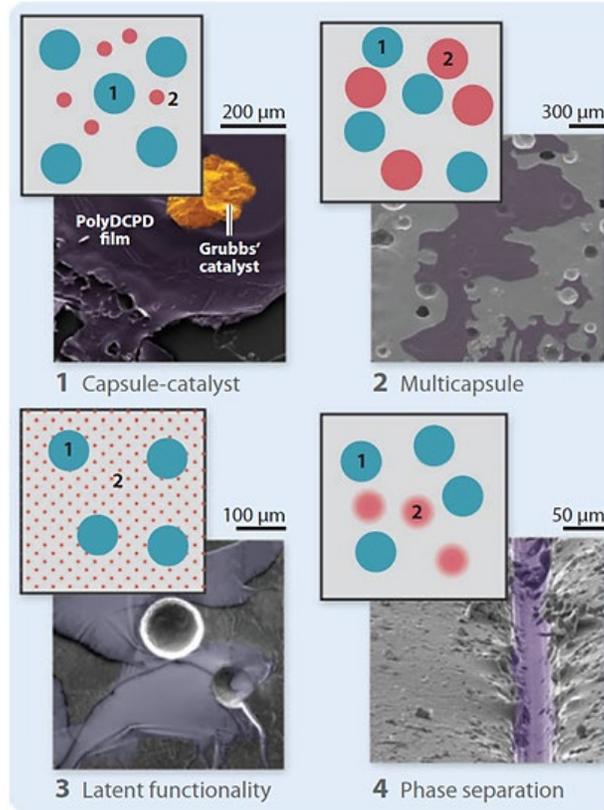
Figure 2.4. Schematic representation of microcapsule based self-healing materials, adapted from Blaiszik et al. (2010), Ref. [21]. Copyright 2010 Annual Reviews.

2.2.1.2. Additive manufacturing of self-healing polymer composites

As discussed above, thermoplastics and thermoset materials have been used to fabricate polymer parts or composites parts using different additive manufacturing technologies due to easy accessibility of 3D printers and its ability to create complex and customized part in an economical way. Thermoplastics are a popular choice for additive manufacturing due to their flexibility, manageable melting temperature, and fast cooling rate and user-friendly safe processing [66] . Poly(lactic acid) (PLA) is a common polymer used for 3D printing due to its biocompatibility, renewability and low extrusion temperature favoring its application in

biomedical industries [67]. Fabrication of PLA and PLA composites using fused filament fabrication has been reported [68]. High impact polystyrene (HIPS) is another polymer commonly used for 3D printing application due easy fabrication and machinability [68]. HIPS has various benefits as a 3D printing material due to its high impact strength, high dimensional stability, and low cost. It is used on a large scale to fabricate prototypes for design validation. It is also used as support material during 3D printing of complex parts containing overhangs and bridging. The main challenges faced by 3D printed thermoplastic materials are poor mechanical properties, poor interlayer adhesion and delamination as compared to traditionally constructed parts which in the long term can lead to material failure. For these reasons, thermoplastics are genuine contenders for self-healing applications using additive manufacturing technologies. The concept of additive manufacturing of self-healing composites is still new. For self-healing of thermoplastic materials Villajos et al. reported on poly(ethylene-co-methacrylic acid) (EMAA) copolymers reinforced with carbon nanotubes for 3D printing of self-healing composites [66].

The second category of polymer composites is thermoset polymer composites. Thermoset polymers in the form epoxy and acrylate resins are popularly used for fabricating composite material due to their excellent mechanical stability at elevated temperature, good chemical resistance, and compatibility with commercial 3D printers [69]. Although, in the case of thermoset materials it is not generally possible to recycle or reshape thermosets if they develop damage. Moreover, in case of a thermoset polymer material, the brittle nature and high crosslinking density of materials can result in catastrophic failure upon damage. Therefore, researchers are trying to find ways to combine self-healing and 3D printing technologies for recovering damages in thermoset polymer materials. Yu et al. studied self-healing properties in elastomers by incorporating thiol and disulfide groups within the structure, which undergo

reversible reactions enabling healing upon addition of force (0.5N), shown in Figure 3A, [70]. Liu et al. studied self-healing in 3D-printed double-network of Polyacrylamide (PAAm) in the presence of k-carrageenan (Figure 3B), and demonstrated recovery of fractures upon heating the samples at high temperature [71].

There are some limitations when it comes to 3D printing of hydrogel based intrinsic self-healing systems, as it depends on external stimulus. Therefore, research on 3D printing of autonomous self-healing polymer systems has been done and there are several studies reported. In 2019, Sanders et al. reported on the self-healing of stereolithographic 3D printing of thermoset composites using the solvent welding mechanism where self-healing of photocured commercial resin was shown using anisole (solvent) filled microcapsules which showed 87% of fracture recovery, shown figure 3A [72]. However, this route is dependent on the solubility of polymer matrix in the solvent, and therefore a more approachable and viable route was investigated by Shinde et al. (Chapter 3) [37]. In this study, Shinde et al. studied stereolithographic (SLA) 3D printing of a self-healing composite system consisting of a commercial photocurable resin with embedded catalyst (Grubbs') and microcapsules containing dicyclopentadiene (DCPD) monomer. This study provided a versatile platform for SLA 3D printing of self-healing thermoset polymer materials as it does not require manipulation of the resin chemistry and has less reliance on solvent for fracture recovery, shown in Figure 3C, [37]. Another route is designing vascular self-healing networks as explained by Postiglione et al., where self-healing polymers based on embedded microvascular networks are 3D printed and resin material is stored in individual microchannel, which upon damage releases the material and diffuses through cracks and heal the crack at microscopic and macroscopic level, shown in Figure 3D, where (a-i) represent images of vascular microchannels and its self-healing after crack event [73].
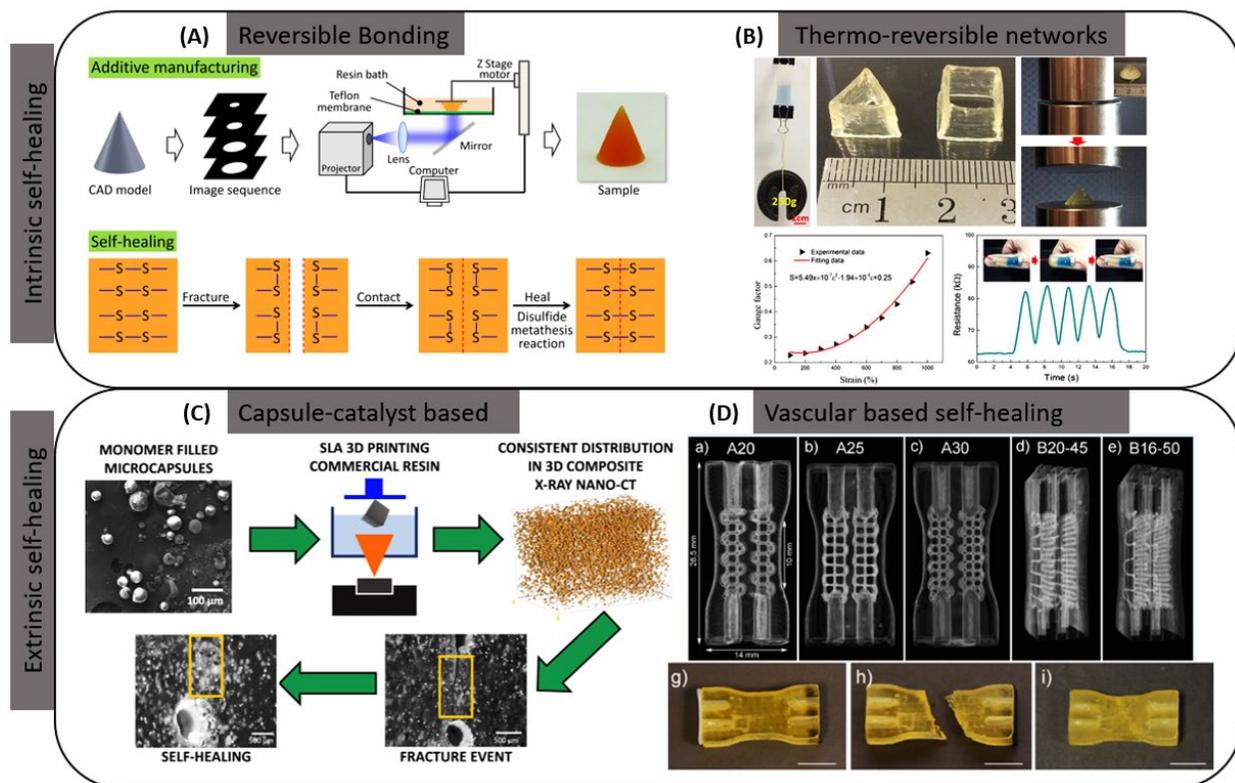
Figure 2.5. (A) Stereolithography 3D printing of self-healing thiol-based elastomer system, showing disulfide bond-assisted self-healing process. Reprinted (adapted) with permission from Ref. [70]. Copyright 2019 Springer Nature. (B) Direct ink writing of polyacrylamide (PAAm) based hydrogel-based self-healing system in presence of k-carrageenan. Reprinted (adapted) with permission from Ref. [71]. Copyright 2017 American Chemical Society. (C) Stereolithography 3D printing of autonomous self-healing microcapsule-based polymer composite system. Reprinted (adapted) with permission from Ref. [37]. Copyright 2020 American Chemical Society. (D) Dual extrusion 3D printing of micro-vascular networks using PVA polymers to design self-healing vascular based system where (a-i) represent images of vascular microchannels and its self-healing after crack event. Reprinted (adapted) with permission from Ref. [73]. Copyright 2017 American Chemical Society.

2.2.2. 3D Printing of Porous Media

Researchers in the geosciences have been using additive manufacturing to fabricate porous media replicating the physical, hydraulic, mechanical and chemical properties of natural samples. A wide variety of materials, including filament, thermoplastics, polymers, photosensitive epoxy resin, etc., and printing methods have been explored to fabricate complex porous structures [74]. Creating the digital model, which is the first step in any 3D printing project, can be based either on the design of an ideal porous media system or one extracted from real samples. In the first approach, a simple fracture network or porous structure is designed in a computer-aided design (CAD) software like AutoCAD, OpenSCAD, etc. [75], or an artificial digital porous model is built by distributing 3D shapes (commonly spheres and cylinders) in a given volume based on a prescribed algorithm [76], [77]. Then these models are converted into an object file which can be read by the printing software. This approach provides the freedom to create various shapes and structures to fit the desired experimental requirements. On the other hand, non-destructive advanced imaging tools can be utilized to capture macro and micropores from undisturbed soil [78], [79], sandstone [80], [81], or shale [82], [83] samples. Nowadays, high-performance computers and advanced imaging tools like 3D X-ray computed tomography (X-ray CT) can reconstruct 3D models of pore geometries of natural samples at high resolution (microns). The 3D images can be segmented and further processed to create a 3D mesh for printing. After printing and post-processing, the printed samples can be imaged again in 3D to extract various properties.

The quality of the printed specimens can vary with printing approach and material, even between replicates. Comparing binder jetting, fused filament fabrication (FFF) and stereolithography apparatus (SLA) methods, Almetwally & Jabbari observed samples printed

with a gypsum-based ProJet printer with binder jetting technology had the closest porosity and permeability to the real sandstone sample [84]. In a later study, they observed SLA 3D printing also provides precise porosity and permeability [75]. It should be noted, however, that some studies have observed a lower porosity in SLA printed specimens compared to the original samples due to trapping of residual resin in micropores [85], [86]. Post-processing steps, like pressurized flushing with ethanol, have been shown to improve porosities for SLA printed replicas of sedimentary rock [85]. Kong et al. employed a binder jetting printing system with silica sand as the base material to study the microstructure in sandstone samples [87]. They observed a variation in porosity in the printed sample compared to the real Berea sandstone sample; however, the pore size distribution of the printed sample agreed well with the real sample.

3D printing has also shown utility to investigate hydraulic properties of soil samples where experiments can be challenging due to alteration of internal pore structures. Bacher et al. explored the use of four different 3D printing techniques: fused filament fabrication (FFF), selective laser sintering (SLS), PolyJet and stereolithography apparatus (SLA) to replicate macropore networks in undisturbed soil samples for water and solute transport experiments [78]. They used acrylonitrile-butadiene-styrene (ABS), alumide and polyamide, high detail resin, and prime gray epoxy resin as printing materials and measured the hydraulic conductivity of the printed samples using the constant head method [78]. Out of the five materials, the specimen printed using the prime gray epoxy resin material was free of residual clogging and hence had the largest and most similar hydraulic conductivity to that of the original undisturbed soil sample [78]. They also noted that the SLS technique is prone to micropore clogging by the residual unsolidified printing material that needs to be removed by mechanical means [78]. Hence this

method is unsuitable for investigating hydraulic and solute transport properties unless the clogging issue is resolved [78]. Dal Ferro & Morari did a similar study aiming to fabricate porous media reflecting the hydraulic conductivity of soil samples utilizing the MultiJet 3D printing technology using resin containing an organic mixture as the printing material [79]. The resulting printed prototype had a one order of magnitude higher saturated hydraulic conductivity compared to the undisturbed soil sample. The observed higher hydraulic conductivity likely result from microstructure printing limitations where Ishutov et al. noted that a minimum pore throat diameter of 400 μm can be printed accurately with stereolithography 3D printing technology [85].

The macroscopic response of hydraulic properties due to changes in the pore network structure can also be investigated by manipulating printing mesh of porous media. Head & Vanorio successfully tested two different 3D printers, a stereolithography desktop printer and MultiJet industrial printer, to explore the ability to manipulate printed microstructures and measure the changes in flow properties [88]. For both printers, they used photosensitive resin as the printing material [88]. They downscaled a vertically connected pore structure in a carbonate sample to mimic the pore volume compaction and observed a decreasing trend in measured and simulated permeability with decreasing porosity [88]. However, for the dissolution model, they enlarged the pore throat diameter without changing the overall length and noted a dramatic change in permeability for a minor change in porosity [88].

Additive manufacturing has also shown utility for investigating rock mechanics. Jiang & Zhao studied the unconfined compressive strength (UCS) and direct tensile strength (DTS) of specimens with different shapes and structures printed by FFF using PLA [89]. Their study found that under compression the specimen exhibits more ductile behavior, and in tensile

strength tests, it tends to be more brittle [89]. Similar stress strain behavior of printed samples to natural rock samples as measured with the mechanical compressive strength test was noted in by Jiang et al. who used a ProJet printer with sand powder and binder material [90]. Moreover, the crack propagation also agreed well with the fracturing behavior of real rock samples under compression. The binder material plays a critical role in the UCS of printed specimens as noted in Hodder et al. for sandstone samples fabricated using an M-Flex sand printer using silica sand coated with p-toluene sulphonic acid (activator) as the base material [91]. Upon addition of the binder material (main component furfuryl alcohol), a condensation reaction takes place, creating polymer necks between the solid grains [91]. UCS tests conducted on the cylindrical replicas showed an increase in the UCS with a higher amount of binder material, however above 8 vol%, they saw instability as the binder material started to clog the pore network and fracture [91].

Printing porous media with geochemically reactive properties was first explored in Anjikar et al. as a means to enhance understanding of geochemical reactions in porous media [80]. They replicated a sandstone sample using the FFF using novel reactive filament fabricated by combining high-impact polystyrene and calcite at varying amounts [80]. 3D images of the printed specimens revealed that the amount of calcite in the printed sample agreed well with the amount mixed with filament; however, the normalized calcite surface area in the printed sample was an order of magnitude lower than real samples having similar amount of calcite. The resulting accessible calcite surface areas, however, agreed well with those determined for real sandstone samples in the literature suggesting this is a promising means of creating reactive porous media specimens [80].

2.3. Research objective

Employing current approaches of self-healing materials, we propose to seek development of self-healing composites using additive manufacturing technologies to investigate the relationships between microcapsule molecular design, microcapsule incorporation within filament (for FFF) and resin (for SLA), and microcapsule healing efficiency of 3D printed polymer composites. Thus, in this work, robust fluid-filled, self-healing microcapsules are prepared by in-situ-interfacial polymerization using previously established methods [71], that can survive 3D printing process. Once self-healing microcapsules have been synthesized, they will be incorporated into the bulk polymer to evaluate their stability within the polymer and their effect on overall material properties. These microcapsules loaded polymer specimen or uncured resin formulations are used to develop 3D printed self-healing composites. Here, the durability of microcapsules when incorporated into the host polymer is a critical element in their overall performance and especially towards their application in 3D printing where processing conditions (namely temperature and flow-imposed shear stresses) pose distinct challenges compared to traditional self-healing composites which is investigated by thermogravimetric analysis or solvent extraction method and by ^{1}H nuclear magnetic resonance (NMR) spectroscopy.

Dynamic Mechanical Analysis (DMA) tests of the 3D printed self-healing composites is performed to ascertain the microcapsules' impact on the modulus and glass transition temperature of the host polymer. Once it has been established that the microcapsules do not have a deleterious effect on the polymer matrix material properties, the healing efficiency of the microcapsule-loaded system, as a function of microcapsule size and concentration is investigated. Healing efficiency is calculated as the ratio of healed fracture toughness (i.e., fracture toughness after healing) to virgin fracture toughness: $\eta = K_Q$ *healed*$/K_Q$ *virgin*.

Specimens will undergo an initial fracture test to determine their virgin fracture toughness. They will be allowed to heal for fixed time intervals and then retested to determine the properties after healing occurs. The results of these tests will identify the optimum microcapsule concentration needed for quick and efficient self-healing to be evaluated for additive manufacturing.

Another goal of this project is to enhance understanding of mineral dissolution and precipitation reactions and impacts on porosity and permeability in porous media using 3D printing approach. Therefore, to achieve that, main objective of this research is to utilize 3D printing to fabricate reactive porous media using fused filament fabrication technology and study the impact of variations in porous media structures and flow rates on where, within individual pores and the greater pore network, mineral reactions occur and the corresponding change in porosity and permeability. The approach will be used to create a series of 3D printed "reactive" porous media and carry out replicate laboratory mineral dissolution and precipitation experiments on these samples measuring permeability evolution and use imaging to identify the time lapsed evolution of porosity.

2.4. References

[1] Zindani, D.; Kumar, K. An insight into additive manufacturing of fiber reinforced polymer composite. *Int. J. Lightweight Mater. Manuf.* **2019**, *2*, 267–278. https://doi.org/10.1016/j.ijlmm.2019.08.004.

[2] Parandoush, P.; Lin, D. A review on additive manufacturing of polymer-fiber composites. *Compos. Struct.* **2017**, *182*, 36–53. https://doi.org/10.1016/j.compstruct.2017.08.088.

[3] S. Mohr.;O. Khan. "3D Printing and the Future of Supply Chains," P*roc. Hambg. Int. Conf.*

Logist., **2015**, 31. (accessed on 01/31/2022).

[4]   Kumar, S.; Kruth, J.-P. Composites by rapid prototyping technology. *Mater. Des.* **2009**, *31*, 850–856. https://doi.org/10.1016/j.matdes.2009.07.045.

[5]   Razavykia, A.; Brusa, E.; Delprete, C.; Yavari, R. An Overview of Additive Manufacturing Technologies—A Review to Technical Synthesis in Numerical Study of Selective Laser Melting. *Materials* **2020**, *13*, 3895. https://doi.org/10.3390/ma13173895.

[6]   Goodridge, R.; Shofner, M.; Hague, R.; McClelland, M.; Schlea, M.; Johnson, R.; Tuck, C. Processing of a Polyamide-12/carbon nanofibre composite by laser sintering. *Polym. Test.* **2011**, *30*, 94–100. https://doi.org/10.1016/j.polymertesting.2010.10.011.

[7]   Cheah, C.; Fuh, J.; Nee, A.; Lu, L. Mechanical characteristics of fiber-filled photo-polymer used in stereolithography. *Rapid Prototyp. J.* **1999**, *5*, 112–119. https://doi.org/10.1108/13552549910278937.

[8]   Chiu, S.-H.; Wicaksono, S.T.; Chen, K.-T.; Chen, C.-Y.; Pong, S.-H. Mechanical and thermal properties of photopolymer/CB (carbon black) nanocomposite for rapid prototyping. *Rapid Prototyp.* J. **2015**, *21*, 262–269. https://doi.org/10.1108/rpj-11-2011-0124.

[9]   Sakly, A.; Kenzari, S.; Bonina, D.; Corbel, S.; Fournée, V. A novel quasicrystal-resin composite for stereolithography. *Mater. Des.* **2014**, *56*, 280–285. https://doi.org/10.1016/j.matdes.2013.11.025.

[10]   Gurr, M.; Hofmann, D.; Ehm, M.; Thomann, Y.; Kübler, R.; Mülhaupt, R. Acrylic Nanocomposite Resins for Use in Ste-reo-lithography and Structural Light Modulation Based Rapid Prototyping and Rapid Manufacturing Technologies. *Adv. Funct. Mater.* **2008**, *18*, 2390–2397. https://doi.org/10.1002/adfm.200800344.

[11] Kim, J.H.; Lee, S.; Wajahat, M.; Jeong, H.; Chang, W.S.; Jeong, H.J.; Yang, J.-R.; Kim, J.T.; Seol, S.K. Three-Dimensional Printing of Highly Conductive Carbon Nanotube Microarchitectures with Fluid Ink. *ACS Nano*. **2016**, *10*, 8879–8887. https://doi.org/10.1021/acsnano.6b04771.

[12] El Moumen, A.; Tarfaoui, M.; Lafdi, K. Additive manufacturing of polymer composites: Processing and modeling approaches. *Compos. Part B Eng.* **2019**, *171*, 166–182. https://doi.org/10.1016/j.compositesb.2019.04.029.

[13] Perelaer, J.; Smith, P.J.; Mager, D.; Soltman, D.; Volkman, S.K.; Subramanian, V.; Korvink, J.G.; Schubert, U.S. Printed elec-tronics: The challenges involved in printing devices, interconnects, and contacts based on inorganic materials. *J. Mater. Chem.* **2010**, *20*, 8446–8453. https://doi.org/10.1039/c0jm00264j.

[14] Seerden, K.A.M.; Reis, N.; Evans, J.R.G.; Grant, P.S.; Halloran, J.W.; Derby, B. Ink-Jet Printing of Wax-Based Alumina Sus-pensions. *J. Am. Ceram. Soc.* **2001**, *84*, 2514–2520. https://doi.org/10.1111/j.1151-2916.2001.tb01045.x.

[15] Masood, S.H.; Song, W.Q. Development of new metal/polymer materials for rapid tooling using Fused deposition modelling. *Mater. Des.* **2004**, *25*, 587–594. https://doi.org/10.1016/j.matdes.2004.02.009.

[16] Plymill, A.; Minneci, R.; Greeley, D.A. TRACE : Tennessee Research and Creative Graphene and Carbon Nanotube PLA Composite Feedstock Development for Fused Deposition Modeling Graphene and Carbon Nanotube PLA Composite Feedstock Development for Fused Deposition Modeling, Chancellor's Honors Program Projects, **2016**. https://trace.tennessee.edu/utk_chanhonoproj/1955

[17] Nikzad, M.; Masood, S.; Sbarski, I. Thermo-mechanical properties of a highly filled

polymeric composites for Fused Depo-sition Modeling. *Mater. Des*. **2011**, *32*, 3448–3456. https://doi.org/10.1016/j.matdes.2011.01.056.

[18] Carneiro, O.S.; Silva, A.F.; Gomes, R. Fused deposition modeling with polypropylene. *Mater. Des.* **2015**, *83*, 768–776. https://doi.org/10.1016/j.matdes.2015.06.053.

[19] Milosevic, M.; Stoof, D.; Pickering, K.L. Characterizing the Mechanical Properties of Fused Deposition Modelling Natural Fiber Recycled Polypropylene Composites. *J. Compos. Sci.* **2017**, *1*, 7. https://doi.org/10.3390/jcs1010007.

[20] Bond, I.; Trask, R.; Williams, H.R. Self-Healing Fiber-Reinforced Polymer Composites. *MRS Bull.* **2008**, *33*, 770–774. https://doi.org/10.1557/mrs2008.164.

[21] Blaiszik, B .; Kramer, S.; Olugebefola, S.; Moore, J.; Sottos, N.; White, S. Self-Healing Polymers and Composites. *Annu. Rev. Mater. Sci.* **2010**, *40*, 179–211. https://doi.org/10.1146/annurev-matsci-070909-104532.

[22] Xu, H.; Tang, Y.; Liu, Z.; Cai, Y.; Wang, Y. The study of typical failure modes and failure mechanism of polymer materials. *IOP Conf. Ser. Mater. Sci. Eng.* **2017**, *231*, 12123. https://doi.org/10.1088/1757-899x/231/1/012123.

[23] Kim, C.; Ejima, H.; Yoshie, N. Polymers with autonomous self-healing ability and remarkable reprocessability under ambient humidity conditions. *J. Mater. Chem.* **2018**, *6*, 19643–19652. https://doi.org/10.1039/c8ta04769c.

[24] Terryn, S.; Mathijssen, G.; Brancart, J.; Lefeber, D.; Van Assche, G.; Vanderborght, B. Development of a self-healing soft pneumatic actuator: A first concept. *Bioinspiration Biomimetics.* **2015**, *10*, 046007. https://doi.org/10.1088/1748-3190/10/4/046007.

[25] White, S.R.; Sottos, N.R.; Geubelle, P.H.; Moore, J.S.; Kessler, M.R.; Sriram, S.R.; Brown, E.N.; Viswanathan, S. Autonomic healing of polymer composites. *Nature.* **2001**, *409*, 794–

797. https://doi.org/10.1038/35057232.

[26] Zhai, L.; Narkar, A.; Ahn, K. Self-healing polymers with nanomaterials and nanostructures. *Nano Today* **2019**, *30*, 100826. https://doi.org/10.1016/j.nantod.2019.100826.

[27] Chen, X.; Dam, M.A.; Ono, K.; Mal, A.; Shen, H.; Nutt, S.R.; Sheran, K.; Wudl, F. A Thermally Re-mendable Cross-Linked Polymeric Material. *Science.* **2002**, *295*, 1698–1702. https://doi.org/10.1126/science.1065879.

[28] Chen, X.; Wudl, F.; Mal, A.K.; Shen, H.; Nutt, S.R. New Thermally Remendable Highly Cross-Linked Polymeric Materials. *Macromolecules.* **2003**, *36*, 1802–1807. https://doi.org/10.1021/ma0210675.

[29] Hong, G.; Zhang, H.; Lin, Y.; Chen, Y.; Xu, Y.; Weng, W.; Xia, H. Mechanoresponsive Healable Metallosupramolecular Polymers. *Macromolecules* **2013**, *46*, 8649–8656. https://doi.org/10.1021/ma4017532.

[30] Peterson, A.M.; Jensen, R.E.; Palmese, G.R. Room-Temperature Healing of a Thermosetting Polymer Using the Diels−Alder Reaction. *ACS Appl. Mater. Interfaces* **2010**, *2*, 1141–1149. https://doi.org/10.1021/am9009378.

[31] Zeng, C.; Seino, H.; Ren, J.; Hatanaka, K.; Yoshie, N. Bio-Based Furan Polymers with Self-Healing Ability. *Macromolecules* **2013**, *46*, 1794–1802. https://doi.org/10.1021/ma3023603.

[32] Zhao, D.; Du, Z.; Liu, S.; Wu, Y.; Guan, T.; Sun, Q.; Sun, N.; Ren, B. UV Light Curable Self-Healing Superamphiphobic Coatings by Photopromoted Disulfide Exchange Reaction. *ACS Appl. Polym. Mater.* **2019**, *1* (11), 2951-2960. https://doi.org/10.1021/acsapm.9b00656.

[33] Moniruzzaman, M.; Christogianni, P.; Kister, G. Self-Healing in Epoxy Thermoset

Polymer Films Triggered by UV Light. In Procedia Engineering; 2016, *148*, 114-121. https://doi.org/10.1016/j.proeng.2016.06.472.

[34] Scheiner, M.; Dickens, T.J.; Okoli, O. Progress towards self-healing polymers for composite structural applications. *Polymer* **2016**, *83*, 260–282. https://doi.org/10.1016/j.polymer.2015.11.008.

[35] Kessler, M.; White, S. Self-activated healing of delamination damage in woven composites. *Compos. Part A Appl. Sci. Manuf.* **2001**, *32*, 683–699. https://doi.org/10.1016/s1359-835x(00)00149-4.

[36] Kessler, M.; Sottos, N.; White, S. Self-healing structural composite materials. *Compos. Part A: Appl. Sci. Manuf.* **2003**, *34*, 743–753. https://doi.org/10.1016/s1359-835x(03)00138-6.

[37] Shinde, V.V.; Celestine, A.-D.; Beckingham, L.E.; Beckingham, B.S. Stereolithography 3D Printing of Microcapsule Cata-lyst-Based Self-Healing Composites. *ACS Appl. Polym. Mater.* **2020**, *2*, 5048–5057. https://doi.org/10.1021/acsapm.0c00872.

[38] Shinde, V.V.; Shelke, S.D.; Celestine, A.N.; Beckingham, B.S. Self-healing in high impact polystyrene (HIPS) composites via embedded non-toxic solvent-filled microcapsules. *J. Appl. Polym. Sci.* **2021**, *139*, 51463. https://doi.org/10.1002/app.51463.

[39] Garcia, S.J.; Fischer, H.R. Self-healing polymer systems: Properties, synthesis and applications. In Smart Polymers and their Applications; Woodhead Publishing: Cambridge, UK, **2014**.

[40] Fischer, H. Self-repairing material systems—A dream or a reality? *Nat. Sci.* **2010**, *2*, 873–901. https://doi.org/10.4236/ns.2010.28110.

[41] Plaisted, T.A.; Nemat-Nasser, S. Quantitative evaluation of fracture, healing and re-healing

of a reversibly cross-linked polymer. *Acta Mater.* **2007**, *55*, 5684–5696. https://doi.org/10.1016/j.actamat.2007.06.019.

[42] Park, J.S.; Takahashi, K.; Guo, Z.; Wang, Y.; Bolanos, E.; Hamann-Schaffner, C.; Murphy, E.; Wudl, F.; Hahn, H.T. Towards Development of a Self-Healing Composite using a Mendable Polymer and Resistive Heating. *J. Compos. Mater.* **2008**, *42*, 2869–2881. https://doi.org/10.1177/0021998308097280.

[43] Park, J.S.; Kim, H.-S.; Hahn, H.T. Healing behavior of a matrix crack on a carbon fiber/mendomer composite. *Compos. Sci. Technol.* **2009**, *69*, 1082–1087. https://doi.org/10.1016/j.compscitech.2009.01.031.

[44] Murphy, E.B.; Bolanos, E.; Schaffner-Hamann, C.; Wudl, F.; Nutt, S.R.; Auad, M. Synthesis and Characterization of a Sin-gle-Component Thermally Remendable Polymer Network: Staudinger and Stille Revisited. *Macromolecules* **2008**, *41*, 5203–5209. https://doi.org/10.1021/ma800432g.

[45] Peterson, A.M.; Jensen, R.E.; Palmese, G.R. Reversibly Cross-Linked Polymer Gels as Healing Agents for Epoxy−Amine Thermosets. *ACS Appl. Mater. Interfaces* **2009**, *1*, 992–995. https://doi.org/10.1021/am900104w.

[46] Pestka, K. A.; Buckley, J. D.; Kalista, S. J.; Bowers, N. R. Elastic Evolution of a Self-Healing Ionomer Observed via Acoustic and Ultrasonic Resonant Spectroscopy. *Sci. Rep.* **2017**, *7* (1), 14417. https://doi.org/10.1038/s41598-017-14321-z.

[47] Eisenberg, A.; Rinaudo, M. Polyelectrolytes and ionomers. *Polym. Bull.* **1990**, *24*, 671–671. https://doi.org/10.1007/bf00300165.

[48] Tanasi, P.; Santana, M.H.; Carretero-González, J.; Verdejo, R.; López-Manchado, M.A. Thermo-reversible crosslinked natural rubber: A Diels-Alder route for reuse and self-

healing properties in elastomers. *Polymer* **2019**, *175*, 15–24.

https://doi.org/10.1016/j.polymer.2019.04.059.

[49] Cordier, P.; Tournilhac, F.; Soulié-Ziakovic, C.; Leibler, L. Self-healing and

thermoreversible rubber from supramolecular assembly. *Nature* **2008**, *451*, 977–980.

https://doi.org/10.1038/nature06669.

[50] Montarnal, D.; Tournilhac, F.; Hidalgo, M.; Couturier, J.-L.; Leibler, L. Versatile One-Pot

Synthesis of Supramolecular Plastics and Self-Healing Rubbers. *J. Am. Chem. Soc.* **2009**,

131, 7966–7967. https://doi.org/10.1021/ja903080c.

[51] O'Connor, K.M.; Wool, R.P. Optical studies of void formation and healing in styrene-

isoprene-styrene block copolymers. *J. Appl. Phys.* **1980**, *51*, 5075.

https://doi.org/10.1063/1.327423.

[52] An, S.; Lee, M.W.; Yarin, A.L.; Yoon, S.S. A review on corrosion-protective extrinsic self-

healing: Comparison of microcap-sule-based systems and those based on core-shell

vascular networks. *Chem. Eng. J.* **2018**, *344*, 206–220.

https://doi.org/10.1016/j.cej.2018.03.040.

[53] Bakry, A.M.; Abbas, S.; Ali, B.; Majeed, H.; Abouelwafa, M.Y.; Mousa, A.; Liang, L.

Microencapsulation of Oils: A Compre-hensive Review of Benefits, Techniques, and

Applications. *Compr. Rev. Food Sci. Food Saf.* **2015**, *15*, 143–182.

https://doi.org/10.1111/1541-4337.12179.

[54] Toohey, K.S.; Sottos, N.R.; Lewis, J.A.; Moore, J.; White, S. Self-healing materials with

microvascular networks. *Nat. Mater.* **2007**, *6*, 581–585. https://doi.org/10.1038/nmat1934.

[55] Ullah, H.; Azizli, K.A.M.; Man, Z.B.; Ismail, M.B.C.; Khan, M.I. The Potential of

Microencapsulated Self-healing Materials for Microcracks Recovery in Self-healing

Composite Systems: A Review. *Polym. Rev.* **2016**, *56*, 429–485.

https://doi.org/10.1080/15583724.2015.1107098.

[56] Brown, E.N.; Sottos, N.R.; White, S.R. Fracture Testing of a Self-Healing Polymer

Composite. *Exp. Mech.* **2002**, *42*, 372–379. https://doi.org/10.1177/001448502321548193.

[57] Brown, E.; White, S.; Sottos, N. Retardation and repair of fatigue cracks in a microcapsule

toughened epoxy composite—Part II: In situ self-healing. *Compos. Sci. Technol.* **2005**, *65*,

2474–2480. https://doi.org/10.1016/j.compscitech.2005.04.053.

[58] Kirkby, E.; Michaud, V.; Månson, J.-A.; Sottos, N.; White, S. Performance of self-healing

epoxy with microencapsulated healing agent and shape memory alloy wires. *Polymer* 2009,

50, 5533–5538. https://doi.org/10.1016/j.polymer.2009.05.014.

[59] Keller, M.W.; White, S.R.; Sottos, N.R. A Self-Healing Poly(Dimethyl Siloxane)

Elastomer. *Adv. Funct. Mater.* **2007**, *17*, 2399–2404.

https://doi.org/10.1002/adfm.200700086.

[60] Kumar, A.; Stephenson, L.; Murray, J. Self-healing coatings for steel. *Prog. Org. Coat.*

2006, *55*, 244–253. https://doi.org/10.1016/j.porgcoat.2005.11.010.

[61] Caruso, M.M.; Delafuente, D.A.; Ho, .V.; Sottos, .N.R.; Moore, .J.S.; White, .S.R. Solvent-

Promoted Self-Healing Epoxy Mate-rials. *Macromolecules* **2007**, *40*, 8830–8832.

https://doi.org/10.1021/ma701992z.

[62] Celestine, A.-D.N.; Sottos, N.R.; White, S.R. Autonomic healing of PMMA via

microencapsulated solvent. *Polymer* **2015**, *69*, 241–248.

https://doi.org/10.1016/j.polymer.2015.03.072.

[63] White, S.R.; Moore, J.S.; Sottos, N.R.; Krull, B.P.; Cruz, W.A.S.; Gergely, R.C.R.

Restoration of Large Damage Volumes in Polymers. *Science* **2014**, *344*, 620–623.

https://doi.org/10.1126/science.1251135.

[64] Williams, G.; Trask, R.; Bond, I. A self-healing carbon fibre reinforced polymer for aerospace applications. *Compos. Part A Appl. Sci. Manuf.* **2007**, *38*, 1525–1532. https://doi.org/10.1016/j.compositesa.2007.01.013.

[65] Shields, Y.; De Belie, N.; Jefferson, A.; Van Tittelboom, K. A review of vascular networks for self-healing applications. *Smart Mater. Struct.* **2021**, *30*, 063001. https://doi.org/10.1088/1361-665x/abf41d.

[66] Calderón-Villajos, R.; López, A.; Peponi, L.; Manzano-Santamaría, J.; Ureña, A. 3D-printed self-healing composite polymer reinforced with carbon nanotubes. *Mater. Lett.* **2019**, *249*, 91–94. https://doi.org/10.1016/j.matlet.2019.04.069.

[67] Mondal, S.; Nguyen, T.P.; Pham, V.H.; Hoang, G.; Manivasagan, P.; Kim, M.H.; Nam, S.Y.; Oh, J. Hydroxyapatite nano bioc-eramics optimized 3D printed poly lactic acid scaffold for bone tissue engineering application. *Ceram. Int.* **2020**, *46*, 3443–3455. https://doi.org/10.1016/j.ceramint.2019.10.057.

[68] Caminero, M.Á.; Chacón, J.M.; García-Plaza, E.; Núñez, P.J.; Reverte, J.M.; Becar, J.P. Additive Manufacturing of PLA-Based Composites Using Fused Filament Fabrication: Effect of Graphene Nanoplatelet Reinforcement on Mechanical Properties, Dimensional Accuracy and Texture. *Polymers* **2019**, *11*, 799. https://doi.org/10.3390/polym11050799.

[69] Afif, A.; Rahman, S.M.; Azad, A.T.; Zaini, J.; Islam, A.; Azad, A. Advanced materials and technologies for hybrid supercapacitors for energy storage—A review. *J. Energy Storage* **2019**, 25. https://doi.org/10.1016/j.est.2019.100852.

[70] Yu, K.; Xin, A.; Du, H.; Li, Y.; Wang, Q. Additive manufacturing of self-healing elastomers. *NPG Asia Mater.* **2019**, *11*, 7. https://doi.org/10.1038/s41427-019-0109-y.

[71] Liu, S.; Li, L. Ultrastretchable and Self-Healing Double-Network Hydrogel for 3D Printing and Strain Sensor. *ACS Appl. Mater. Interfaces* **2017**, *9*, 26429–26437. https://doi.org/10.1021/acsami.7b07445.

[72] Sanders, P.; Young, A.; Qin, Y.; Fancey, K.S.; Reithofer, M.R.; Guillet-Nicolas, R.; Kleitz, F.; Pamme, N.; Chin, J.M. Stereo-lithographic 3D printing of extrinsically self-healing composites. *Sci. Rep.* **2019**, *9*, 1–6. https://doi.org/10.1038/s41598-018-36828-9.

[73] Postiglione, G.; Alberini, M.; Leigh, S.; Levi, M.; Turri, S. Effect of 3D-Printed Microvascular Network Design on the Self-Healing Behavior of Cross-Linked Polymers. *ACS Appl. Mater. Interfaces* **2017**, *9*, 14371–14378. https://doi.org/10.1021/acsami.7b01830.

[74] Guddati, S.; Kiran, A.S.K.; Leavy, M.; Ramakrishna, S. Recent advancements in additive manufacturing technologies for porous material applications. *Int. J. Adv. Manuf. Technol.* **2019**, *105*, 193–215. https://doi.org/10.1007/s00170-019-04116-z.

[75] Almetwally, A.G.; Jabbari, H. 3D-Printing Replication of Porous Media for Lab-Scale Characterization Research. *ACS Omega* **2021**, *6*, 2655–2664. https://doi.org/10.1021/acsomega.0c04825.

[76] Ozelim, L.C.D.S.M.; Cavalcante, A.L.B. Combining Microtomography, 3D Printing, and Numerical Simulations to Study Scale Effects on the Permeability of Porous Media. *Int. J. Géoméch.* **2019**, *19*, 04018194. https://doi.org/10.1061/(asce)gm.1943-5622.0001340.

[77] Suzuki, A.; Watanabe, N.; Li, K.; Horne, R.N. Fracture network created by 3-D printer and its validation using CT images. *Water Resour. Res.* **2017**, *53*, 6330–6339. https://doi.org/10.1002/2017wr021032.

[78] Bacher, M.; Schwen, A.; Koestel, J. Three-Dimensional Printing of Macropore Networks

of an Undisturbed Soil Sample. *Vadose Zone J.* **2015**, 14.

https://doi.org/10.2136/vzj2014.08.0111.

[79] Ferro, N.D.; Morari, F. From Real Soils to 3D-Printed Soils: Reproduction of Complex

Pore Network at the Real Size in a Silty-Loam Soil. *Soil Sci. Soc. Am. J.* **2015**, *79*, 1008–

1017. https://doi.org/10.2136/sssaj2015.03.0097.

[80] Anjikar, I.S.; Wales, S.; Beckingham, L.E. Fused Filament Fabrication 3-D Printing of

Reactive Porous Media. *Geophys. Res. Lett.* **2020**, 47.

https://doi.org/10.1029/2020gl087665.

[81] Ishutov, S.; Hasiuk, F.; Harding, C.; Gray, J.N. 3D printing sandstone porosity models.

Interpretation **2015**, *3*, 49–61. https://doi.org/10.1190/int-2014-0266.1.

[82] Goral, J.; Deo, M. Nanofabrication of synthetic nanoporous geomaterials: From nanoscale-

resolution 3D imaging to nano-3D-printed digital (shale) rock. *Sci. Rep.* **2020**, *10*, 1–12.

https://doi.org/10.1038/s41598-020-78467-z.

[83] Garum, M.; Glover, P.W.J.; Lorinczi, P.; Scott, G.; Hassanpour, A. Ultrahigh-Resolution

3D Imaging for Quantifying the Pore Nanostructure of Shale and Predicting Gas Transport.

Energy Fuels **2020**, *35*, 702–717. https://doi.org/10.1021/acs.energyfuels.0c03225.

[84] Almetwally, A.; Jabbari, H. Experimental investigation of 3D printed rock samples

replicas. *J. Nat. Gas Sci. Eng.* **2020**, *76*, 103192.

https://doi.org/10.1016/j.jngse.2020.103192.

[85] Ishutov, S.; Hasiuk, F.J.; Jobe, D.; Agar, S. Using Resin-Based 3D Printing to Build

Geometrically Accurate Proxies of Porous Sedimentary Rocks. *Groundwater* **2017**, *56*,

482–490. https://doi.org/10.1111/gwat.12601.

[86] Song, R.; Wang, Y.; Sun, S.; Liu, J. Characterization and microfabrication of natural

porous rocks: From micro-CT imaging and digital rock modelling to micro-3D-printed rock analogs. *J. Pet. Sci. Eng.* **2021**, *205*, 108827. https://doi.org/10.1016/j.petrol.2021.108827.

[87] Kong, L.; Ostadhassan, M.; Hou, X.; Mann, M.; Li, C. Microstructure characteristics and fractal analysis of 3D-printed sandstone using micro-CT and SEM-EDS. *J. Pet. Sci. Eng.* **2019**, *175*, 1039–1048. https://doi.org/10.1016/j.petrol.2019.01.050.

[88] Head, D.; Vanorio, T. Effects of changes in rock microstructures on permeability: 3-D printing investigation. *Geophys. Res. Lett.* **2016**, *43*, 7494–7502. https://doi.org/10.1002/2016gl069334.

[89] Jiang, C.; Zhao, G.-F. A Preliminary Study of 3D Printing on Rock Mechanics. *Rock Mech. Rock Eng.* **2014**, *48*, 1041–1050. https://doi.org/10.1007/s00603-014-0612-y.

[90] Jiang, Q.; Feng, X.; Song, L.; Gong, Y.; Zheng, H.; Cui, J. Modeling rock specimens through 3D printing: Tentative experiments and prospects. *Acta Mech.* Sin. **2015**, *32*, 101–111. https://doi.org/10.1007/s10409-015-0524-4.

[91] Hodder, K.J.; Nychka, J.A.; Chalaturnyk, R.J. Process limitations of 3D printing model rock. *Prog. Addit. Manuf.* **2018**, *3*, 173–182. https://doi.org/10.1007/s40964-018-0042-6.

Chapter 3

Stereolithographic 3D Printing of Self-healing Polymer Composites

3.1. Introduction

Stereolithographic (SLA) 3D printing of thermoset polymers for industrial applications has been rapidly evolving over the last decade [1]-[5]. The expansion of interest is driven by its high degree of customization, ability to construct complex designs with high precision and excellent surface finish [6], [7]. SLA 3D printing builds an object layer-by-layer by using photopolymerization. During SLA, a beam of light is focused to a spot within a liquid resin bath; activating a photoinitiator that begins the polymerization process. By controlling the light position and resin chemistry, desired objects are printed from this liquid resin bath into the final solid object; the objects' architectures are manipulated utilizing a variety of computer-aided design (CAD) programs [8]. Crosslinking of 3D printed structures leads to various properties including high glass transition temperature, high modulus, good solvent resistance, and high tensile strength [9]. In conjunction with the increasing ease and accessibility of 3D printing processes, the interplay of these properties have led to extensive use of 3D printing of thermoset resins for rapid prototyping for industrial applications and as matrix materials for reinforced composites. However, 3D printing

of thermoset polymer materials remains constrained by limitations in mechanical properties and functionalities afforded by the various SLA resin chemistries as compared to traditionally constructed components [6], [7]. The crosslinked nature of SLA printed specimens leads to relatively low toughness and elongation resulting in brittle fracture and catastrophic material failure which, combined with poor resistance to crack initiation, limits the useful life of these SLA 3D printed materials [10]-[12].

Additionally, many options for 3D printing of thermoset polymer materials are not intrinsically sustainable or recyclable due to their crosslinked networks requiring disposal if they suffer any damage during processing or use. In nature, biological systems overcome this issue by using self-healing as their survival strategy to heal injuries [13]. Thus, taking inspiration from nature, we investigate the fabrication of self-healing thermoset composites using SLA 3D printing to extend material lifetimes. Self-healing materials can be categorized as either intrinsic or extrinsic [14], [15]. Intrinsic self-healing materials repair damage using latent functionality of a polymer material and recover the material's properties either by reversible polymerization, hydrogen bonding or molecular diffusion and typically requires an external trigger to initiate the healing [16]-[19]. Extrinsic self-healing materials repair their damage without external intervention using embedded healing materials in the form of microcapsules or vascular capillaries containing healing fluids [20]-[23]. During the fracture event, healing fluid releases into the damage site and seals the crack by polymerization or entanglement process [24]. As intrinsic self-healing systems work on the principle of molecular diffusion, they are typically limited to thermoplastic materials and elastomers [21]. However, in the case of microcapsule-based self-healing, thermoset polymers can also be used, as molecular diffusion of polymer chains is not a requirement for healing [19]. In 2001, White et al. showed for the first time autonomous, extrinsic,

microcapsule-based self-healing by embedding Grubbs' catalyst particles and dicyclopentadiene (DCPD)-filled microcapsules into an epoxy matrix [21]. When microcapsules are ruptured, DCPD fluid releases to the crack location and with the help of a catalyst, it forms crosslinked networks around the crack plane, healing the fracture and restoring mechanical integrity of thermoset materials [21]. Since that first demonstration, several studies have explored different encapsulation chemistries in microcapsule synthesis, and their capability of healing fractures within polymer matrices or at the polymer-fiber interface in composites [20], [21], [25]-[32].

Recently, coupled with the increasing interest in 3D printing technologies, there has been increasing attention paid to improving material properties and incorporating functionalities developed for traditional composites into 3D printing platforms [33], [34]. Studies on 3D printing of self-healing thermoset polymer composites have only recently been reported [24], [35]-[37]. For instance, Yu et al. included self-healing properties in elastomers by incorporating thiol and disulfide groups within the structure; which undergo reversible reactions enabling healing.[37] Also, direct 3D printing of hydrogels for developing strain sensors for wide applications in health monitors, sports, and electronic skin have been reported [38]-[41]. However, these reports typically use intrinsic physical and chemical properties of the matrix polymer or external trigger such as heat to initiate self-healing [37], [38]. In addition, in 2019, Sanders et. al. reported on the self-healing of stereolithographic 3D-printed thermoset composites using anisole (solvent) filled microcapsules to enable self-healing upon microcapsule rupture; a solvent welding mechanism [24]. Using this route, a healing efficiency (ratio of fracture toughness of healed material to that of the virgin material) of 87% was achieved after 3 days [24]. However, this route is dependent on solubility of matrix resin in the solvent. The use of solvent-healing cannot be generalized for all resin materials as the requisite solvent characteristics for each resin material will vary based on

their solubility parameter. Moreover, the presence of solvent can soften the polymer matrix after the healing process [25], [42]-[44]. These drawbacks can be overcome by using a microcapsule-catalyst system, the focus of this work, where healing requires dispersed catalyst for polymerization of an encapsulated monomer (healing fluid) to provide self-healing in response to a damage event. In addition, such microcapsule-catalyst systems can be used for a wide variety of thermoset resins as it is essentially independent of the matrix material chemistry.

Herein, we demonstrate stereolithographic (SLA) 3D printing of a self-healing composite system consisting of a commercial photocurable resin with embedded catalyst (Grubbs') and microcapsules containing dicyclopentadiene (DCPD) monomer. The mechanism of this system relies on monomer (DCPD) release at the fracture site and its subsequent catalytic polymerization to restore mechanical properties and local structural integrity of the surrounding polymer matrix. This autonomous self-healing mechanism of microcracks within 3D printed composite structures can enable retention of material matrix integrity towards preventing or delaying mechanical failure of SLA 3D printed materials. Microcapsule survivability after SLA 3D printing is demonstrated using ^{1}H nuclear magnetic resonance (NMR) spectroscopy. Microcapsule dispersion in the polymer matrix and response to induced fracture and fracture sealing is characterized using optical microscopy, scanning electron microscopy (SEM), and 3D X-ray Nano-CT. Self-healing behavior of these 3D printed composite structures is investigated using single edge notch bend (SENB) tests, demonstrating recovery of material's fracture toughness over 72 hours. Overall, this investigation demonstrates SLA 3D printed self-healing composites based on microcapsule-catalyst autonomous self-healing are a promising and flexible approach for fabricating 3D objects with self-healing characteristics.

3.2. Experimental Methods

3.2.1. Materials

All chemicals and solvents were used as received unless otherwise noted. 1st generation Grubbs' catalyst and Ethyl phenylacetate (EPA) were purchased from Sigma-Aldrich. Polyurethane (PU) prepolymer (Desmodur L 75) was graciously donated by Covestro. Desmodur L 75 is a prepolymer solution in ethyl acetate with a reported equivalent weight of 315 g and an isocyanate content of 13.3 $\pm$ 0.4 wt.%. Ethylene-maleic anhydride (EMA) copolymer (Zemac-400) powder was purchased from Polyscience Inc. and used as a 2.5 wt.% aqueous solution. Dichloromethane, urea, ammonium chloride (NH_4Cl), and sodium hydroxide (NaOH) pellets were purchased from BDH chemicals. 0.5 N NaOH and 0.5 M hydrochloric acid solution were prepared and used to adjust the pH of the emulsion. Formaldehyde solution (formalin, 37 w/v %) was purchased from BTC chemicals. Dicyclopentadiene (DCPD) and hydrochloric acid (95% purity) were purchased from Merck Chemicals. 1-Octanol was purchased from Fischer Chemicals. Anycubic SLA UV curing resin was purchased from Shenzhen ANYCUBIC Technology Co., Ltd.. Isopropanol and acetone were purchased from VWR. Deuterated chloroform ($CDCl_3$) was purchased from EMD Millipore. All solvents and chemicals used for preparation of EMA solution, acid and base solutions and 1-octanol were of analytical grade.

3.2.2. Preparation of PU-UF microcapsules with DCPD core fluid

Double-walled microcapsules were synthesized following the general procedure of Caruso et. al.[22] which synthesizes polyurethane/poly (urea-formaldehyde) (PU-UF) microcapsules in a single batch process. The procedure combines in-situ poly(urea-formaldehyde) microencapsulation with an interfacial microencapsulation using a PU prepolymer (Desmodur L 75) [22]. Briefly, 2.5 wt.% of poly (ethylene-alt-maleic anhydride), EMA, in water was prepared by adding 3.75 g of EMA to

150 mL of water and allowing to stir for 24 hours. 50 mL of this 2.5 wt.% aqueous solution of EMA copolymer and 200 mL of deionized water were blended at 550 rpm with a magnetic stirrer in a 500 mL beaker placed in a temperature-controlled water bath (25 °C). Under blending, 5.00 g urea, 0.50 g ammonium chloride and 0.50 g resorcinol were added sequentially to the previous solution. The pH was raised from ~2.60 to 3.50 by drop-wise addition of 0.5 N sodium hydroxide solution. One to two drops of 1-octanol were then added to expel surface air bubbles. Separately, 3 g of Desmodur L-75 was dissolved in 20 mL of dichloromethane in a water bath maintained at 80 °C. Subsequently, 60 mL of dicyclopentadiene, DCPD was slowly added to this solution, and the solution was stirred continuously for an hour before adding to the above-described aqueous solution to form an emulsion under stirring for 10-20 min. Once stabilized, 12.67 g of 37 wt.% aqueous solution of formaldehyde was added to achieve a 1:1.9 molar proportion of formaldehyde to urea. The emulsion was covered with aluminum foil and heated to 55 °C with continuous mixing at 600-800 rpm. Following 4 hours of mixing the hot plate was turned off and the solution was cooled to room temperature. Microcapsules were then captured from the suspension with a coarse-fritted funnel under vacuum, washed with deionized water, and air dried for 24–48 h. After drying, microcapsules were sieved using a stack of laboratory sieve trays with mesh sizes of 90 μm, 106 μm, 150 μm and 212 μm under mechanical shaking to isolate fractions of the synthesized microcapsule size distribution. A batch of EPA-containing microcapsules was also prepared using an analogous procedure for inclusion in SLA 3D printed specimens for X-ray Nano-CT characterization to ensure microcapsule stability during shipping and handling, details below.

3.2.3. Characterization of neat microcapsules

Optical microscope images of microcapsules were captured using an OLYMPUS 52X7 optical microscope at varied magnifications and analyzed for microcapsule diameter (175 microcapsules)

using ImageJ. Thermogravimetric analysis (TGA) was carried out on a TA Instruments Q500 equipped with an autosampler to evaluate thermal stability of microcapsules. TGA samples were heated at a rate 10 °C/min from 25 to 600 °C under nitrogen flow.

3.2.4. SLA 3D printing of microcapsule-containing composites

Double-walled DCPD microcapsules of average diameter of 96 μm ± 11 were used to probe microcapsule-composite material self-healing capabilities. Formulations of microcapsules (5 wt.%) in commercial ANYCUBIC resin were prepared by addition of the microcapsules and 0.5 wt.% of 1st generation Grubbs' catalyst to the resin, followed by mixing the dispersion at 500-600 rpm for 10-15 minutes to distribute the microcapsules and catalyst in the resin. The mixture was poured into the resin tank of an ANYCUBIC SLA printer and an STL file of a desired 3D structure was loaded into the ANYCUBIC Photon Slice64 software, provided by ANYCUBIC to generate a photon file, and a layer height of 100 microns was selected. Finished prints were immediately washed with isopropyl alcohol to remove uncured resin on the outer surface of the specimen, and the sample was placed under a UV lamp for 3-5 minutes for finishing. Rectangular composite bars of dimensions 52.8 mm × 12 mm × 6 mm were 3D printed and used for mechanical testing, SEM, and confirmation of microcapsules surviving the printing process. Solid cubes (20 mm × 20 mm × 20 mm) and cubical grid lattices (15 mm × 15 mm ×15 mm) were 3D printed with and without EPA-containing microcapsules and used for X-ray Nano-CT characterization, details below.

3.2.5. Characterization of 3D-printed self-healing composites

3.2.5.1. ^{1}H Nuclear Magnetic Spectroscopy

The survivability of the microcapsules in SLA 3D printed composite specimens was evaluated through the release of the core healing fluid (DCPD) after mechanically crushing specimens. Fabricated SLA 3D-printed specimens containing 5 wt.% microcapsules and 0.5 wt.% catalyst

were physically crushed and rinsed with $CDCl_3$. The $CDCl_3$ rinse was filtered to remove SLA resin debris and catalyst. The filtrate was loaded into an NMR tube, and characterized using low-field (60 MHz) ^{1}H NMR spectroscopy. ^{1}H-NMR spectra were collected on an Oxford Instruments Pulsar 60 MHz spectrometer.

3.2.5.2. Scanning Electron Microscopy

Scanning electron microscopy (SEM) was performed using a Zeiss EVO50 SEM to visualize the fracture plane of a SLA printed composite containing monomer filled microcapsules. The fracture surface was obtained by cutting the specimen with a Buehler Isomet 1000 precision cutter, and washing with isopropyl alcohol to remove any residual DCPD monomer released by microcapsule rupture. Cut specimens were then sputter-coated with gold using an EMS 550X Auto Sputter Coating Device with carbon coating attachment prior to analysis.

3.2.5.3. X-ray Nano-CT

X-ray Nano-CT is non-destructive technique to visualize the inner morphology of materials. Here, X-ray Nano-CT is used to visualize the presence and distribution of microcapsules within 3D printed composites. X-ray Nano-CT images of square samples (2 cm x 2 cm x 2 cm) printed with and without 5 wt.% EPA-containing microcapsules with a mean diameter and standard deviation (determined by optical imaging analysis) of 129 μm ± 16 μm were obtained at the University of Florida Research Service Center with a Nano-CT-GE V/TOME/X M 240 with an image resolution of 21.4 μm. Acquired images of the solid square cubes were segmented into microcapsule and matrix polymer voxels by intensity using MATLAB where the threshold was determined manually in ImageJ. The image stack was then converted into a 3D binary image and the properties of microcapsules analyzed using bwconncomp in MATLAB to determine the volume and centroid location of clusters larger than 70 μm diameter. The diameter of identified microcapsules was

determined assuming a spherical geometry of microcapsules. X-ray Nano-CT of cubical grid lattice structures (15 mm × 15 mm × 15 mm) with and without analogous 5 wt.% EPA-containing microcapsules were obtained using 155 Zeiss 620 Versa located at Auburn University with a image resolution of 22.2 μm. The brightness of cubical grid lattice images was adjusted for clarity and examined for microcapsule presence and general features.

3.2.5.4. Dynamic Mechanical Analysis

Thermomechanical behavior of the SLA 3D printed self-healing composites was characterized by dynamic mechanical analysis (DMA) using a TA instruments RSA III DMA. Storage modulus (E') at a room temperature and glass transition temperature (Tg, extracted as the peak in tan delta) of 3D-printed SLA composites were determined using a dynamic temperature ramp test with a frequency of 1 Hz and heat rate of 5 °C/min.

3.2.5.5. Fracture toughness

Single-edged notched beam (SENB) (ASTM D5045-14) testing was used to evaluate fracture toughness, and self-healing efficiency of microcapsule-loaded SLA 3D printed composites [44] ,[45]. The self-healing efficiency of a material is defined as a ratio of the fracture toughness, K_Q, of the healed material to that of the virgin material; Equation 1.

$$Healing\ efficiency = \frac{K_{Q(healed)}}{K_{Q(virgin)}} \tag{1}$$

Displacement-controlled SENB tests were performed using a screw-driven Instron mechanical test frame (Model Instron 5565) with a 5 kN load cell at a loading rate of 5 mm/min. Specimens of dimensions 52.8 mm × 12 mm × 6 mm with a pre-induced notch and a natural crack were used. An initial crack length of 6 mm was used corresponding to an approximate *a/W* value of 0.5; where *a* is the length of the crack and *W* is the width of the specimen. The value of *f(x)* is then calculated using Equation 2,

$$f(x) = 6x^{1/2} \frac{[1.99 - x(1-x)(2.15 - 3.93 + 2.7x^2)]}{(1+2x)(1-x)^{3/2}} \tag{2}$$

where, x is the a/W value. Fracture toughness (K_Q) of the specimen was calculated using Equation 3,

$$K_Q = \left(\frac{P_Q}{BW^{\frac{1}{2}}} \right) f(x) \tag{3}$$

where, K_Q is the fracture toughness, P_Q is the offset intercept, B is the specimen thickness, and W is the specimen width. The value of P_Q for each specimen is obtained from the load versus extension plot using a 5% reciprocal slope offset.

3.3. Result and Discussion

In this chapter, we integrate monomer–containing microcapsules and catalyst with photocurable resin for stereolithographic 3D printing. When a crack occurs, capsules are ruptured along the crack propagation pathway, releasing the monomer-dicyclopentadiene (DCPD) to the crack site. Ring opening metathesis polymerization (ROMP) can then occur using the Grubbs' catalyst embedded within the polymer and formation of solid polymer across the crack leads to crack healing [16]. This method is advantageous because of rapid polymerization at ambient temperature and formation of highly cross-linked polymer network suitable for brittle polymers [16]. Dicyclopentadiene (DCPD) is a commonly-used monomer for self-healing due to its ability to polymerize quickly with minimal shrinkage during healing, low viscosity, long shelf life, and low volatility [16]. DCPD is a clear light-yellow liquid at room temperature and can be easily emulsified with a water. Dicyclopentadiene (DCPD) is a monomer, amenable to ring-opening-metathesis polymerization (RPMP) using Grubbs' catalyst, and the resulting poly-(DCPD) is

considered as good healing material [16]. During ROMP, the double bond within the 6-carbon ring (Scheme 3.1) is broken and reformed with another broken double bond from a second DCPD monomer [16]. This step is repeated, adding DCPD to the poly(dicyclopentadiene) chain.
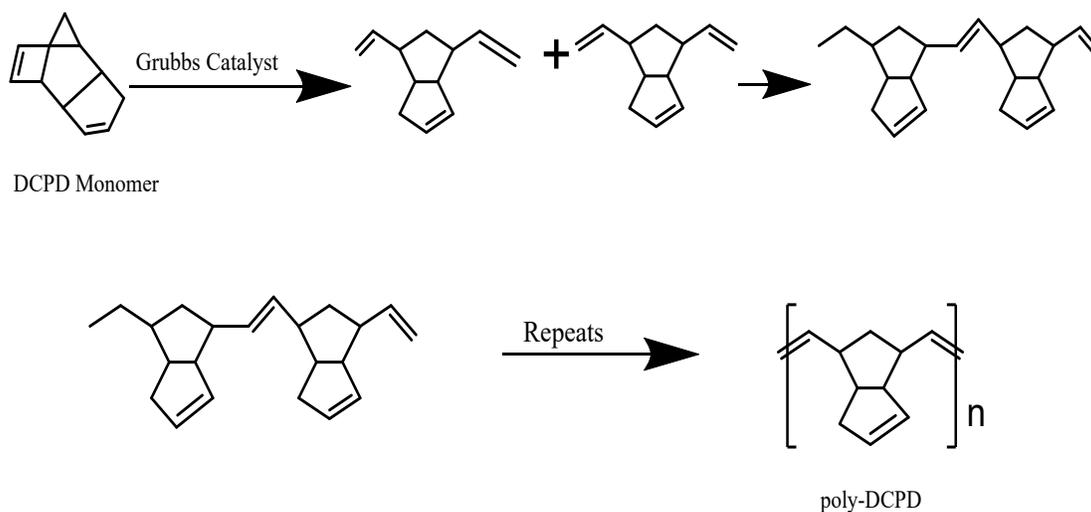
Scheme 3.1 Ring opening metathesis polymerization of DCPD

3.3.1. Synthesis and characterization of PU-UF double-walled microcapsules.

Double-walled microcapsules with DCPD as a core fluid were synthesized by in situ interfacial polymerization due to their thicker and more robust shell walls as compared to single walled microcapsules [26], [27], [47], [48]. This is important for obtaining long-term microcapsule stability at elevated temperatures and high shear stress environments such as those in the processing of polymer materials and composites for additive manufacturing. This process successfully synthesized intact microcapsules with encapsulated healing fluid (DCPD). Optical microscope images of as-prepared microcapsules (Figure 3.1A) and subsequently crushed microcapsules (Figure 3.1B) are shown in Figure 3.1 where the presence of healing fluid is confirmed by its release upon microcapsule compression.
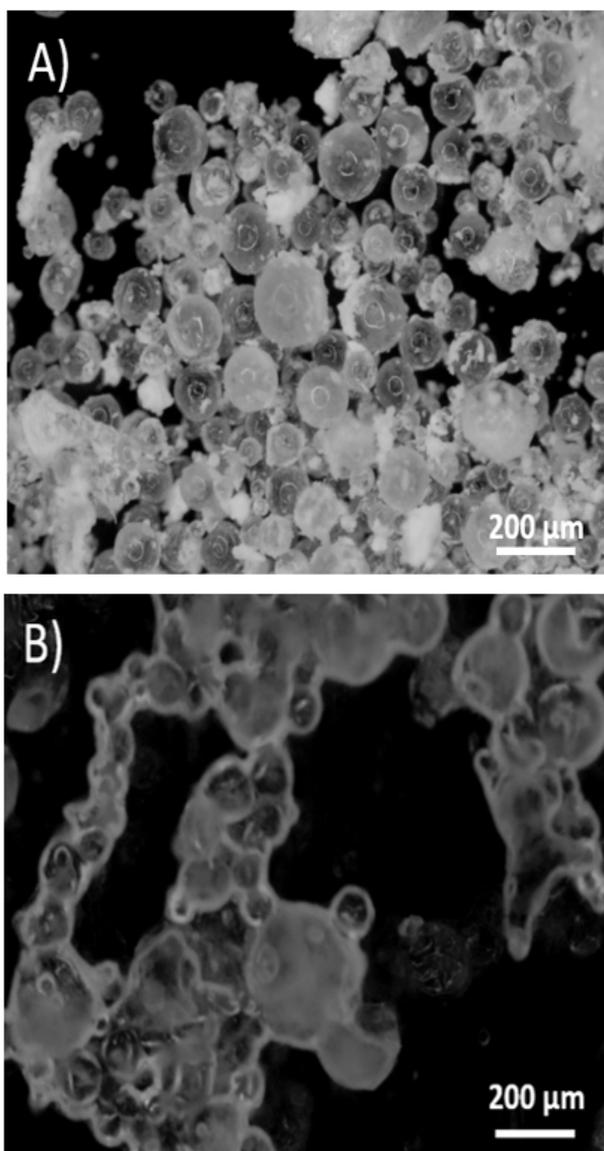
Figure 3.1. Optical microscopy image showing A) spherical microcapsules and B) microcapsules ruptured under the cover slip showing of release of healing fluid.

TGA was performed on neat DCPD-containing microcapsules (Figure 3.2) for a heating cycle from 25 to 600 ºC to evaluate the microcapsule thermal stability and verify the presence of DCPD core fluid after encapsulation. As shown in Figure 3.2, a dramatic loss in microcapsule

weight is observed above 200 °C; 5% weight loss occurs at 163 °C. We attribute this weight loss to microcapsule rupture and loss of DCPD as vapor at and above the normal boiling point of DCPD (170 °C) [16]. As DCPD vaporizes, the rapid volumetric expansion causes the microcapsules to rupture. The appearance of this large drop at the DCPD boiling point is thereby a useful means of confirming that microcapsules contain the core healing fluid. Conversely, this is also an apt demonstration of how the boiling point of the healing fluid (here DCPD) is a limiting factor for the thermal stability of microcapsules for self-healing.
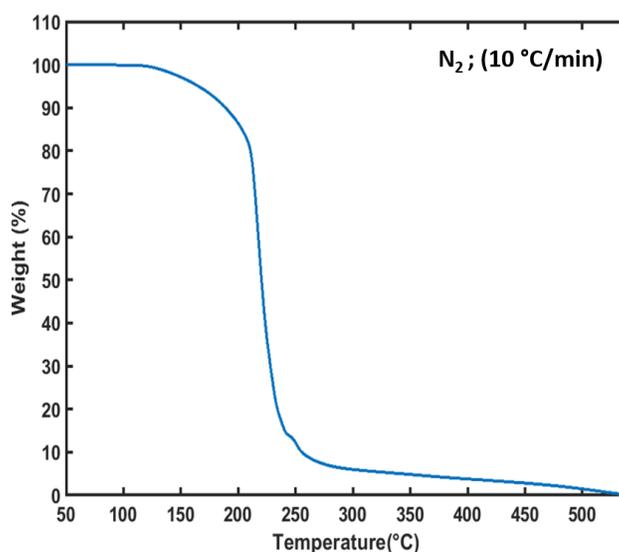
Figure 3.2. Representative TGA curve for PU-UF DCPD microcapsules.

Microcapsule size distribution was evaluated through optical microscopy (Figure 3.3). A random selection of 175 microcapsules were chosen and measured yielding a mean microcapsule diameter of 82 μm ± 17 μm for the as-synthesized microcapsule batch. The particle size distribution of the as-synthesized microcapsules is quite broad with microcapsule diameter varying from 50 to 130 μm (Figure 3.3B). As described in the Experimental section, this microcapsule batch was then sieved, and the microcapsules captured on a 90 μm tray (and below a 106 μm tray) were used for subsequent work in this study; an optical image of sieved microcapsules shown in

Figure 3.3C. The size distribution of the sieved microcapsule batch was similarly quantified Figure

3.3D and was found to have an average diameter of 96 μm ± 11 μm. In Table 3.1, particle size

distributions of the DCPD-containing microcapsules (as-synthesized as well as sieved), and EPA-

containing microcapsules used in this work is shown. EPA-containing microcapsules were used

for the X-ray Nano-CT characterization.
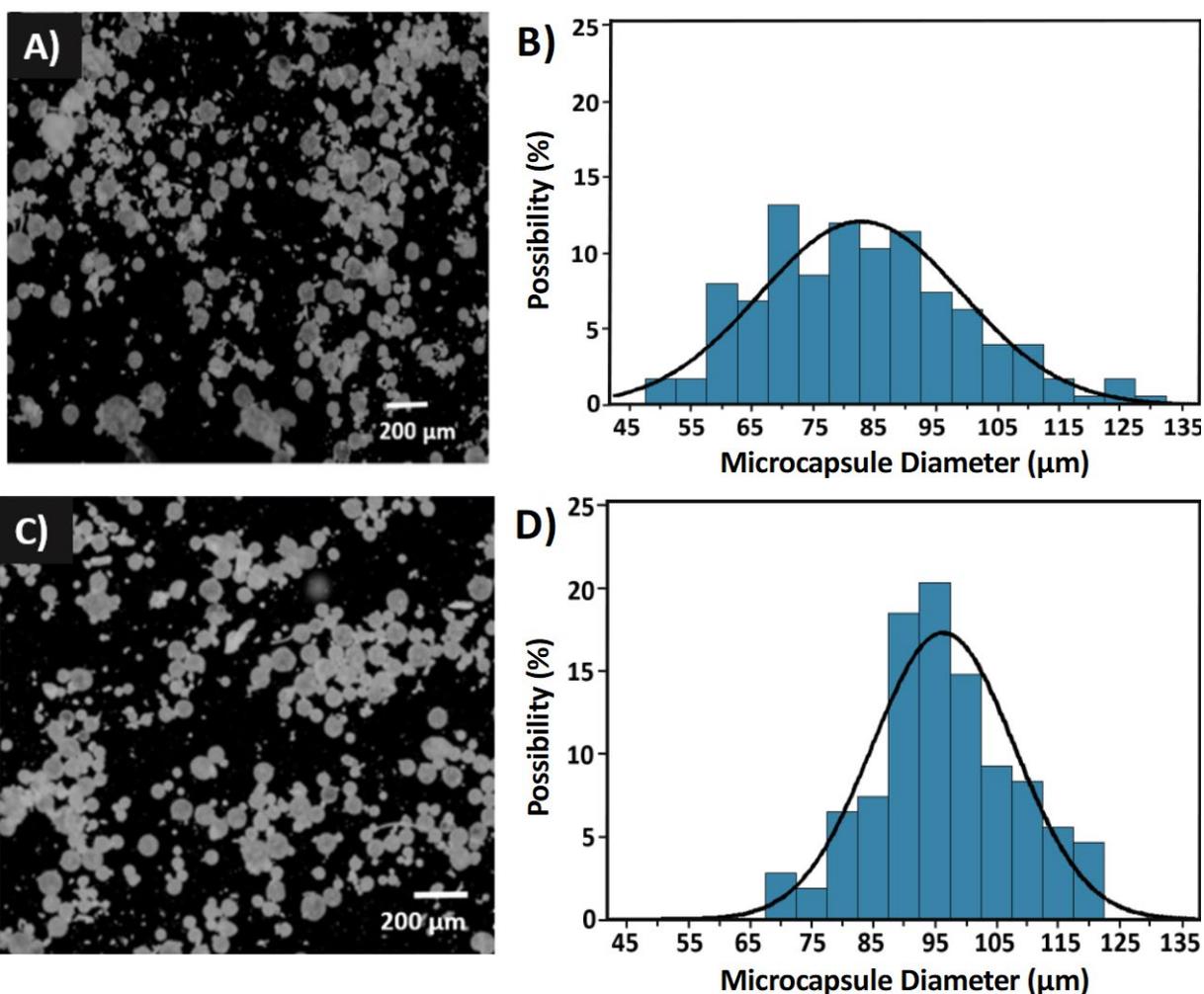
Figure 3.3. A) Optical microscopy image of PU-UF (DCPD core) unsieved microcapsules, and

their B) particle size distribution (mean diameter and standard deviation – 82 μm ± 17 μm). C)

Optical microscopy image of sieved PU-UF (DCPD core) microcapsules and D) their particle size

distribution (mean diameter and standard deviation – 96 μm ± 11 μm).

Table 3.1. Particle size distribution of microcapsules

Microcapsules	Core fluid	Mean Capsule Diameter (μm)	Standard Deviation (μm)
As-synthesized	DCPD	82	17
Sieved	DCPD	96	11
As-synthesized	EPA	129	16

3.3.2. Microcapsule survivability in SLA printed composites

3.3.2.1. ^{1}H NMR Spectroscopy

Existence of unbroken microcapsules in SLA 3D printed composites was evaluated through the presence of DCPD in crushed composite specimens (52.8 mm x 12 mm x 6 mm) containing 5 wt.% sieved double walled DCPD microcapsules and 0.5 wt.% catalyst. The crushed SLA 3D printed specimens were rinsed with $CDCl_3$, the rinse was filtered, and the filtrate was analyzed by ^{1}H-NMR spectroscopy; Figure 3.4. The ^{1}H-NMR spectra in Figure 4 clearly shows the presence of DCPD as the two expected distinct allylic peaks at 5.49 and 5.98 ppm appear in the area ratio of 1:1. Several peaks in the aliphatic region in the range of 1.3 to 3.21 ppm are also observed which also correspond to DCPD. allylic protons at 5.49 and 5.98 ppm. This process demonstrates the presence of intact DCPD-filled microcapsules in the SLA 3D printed specimen.
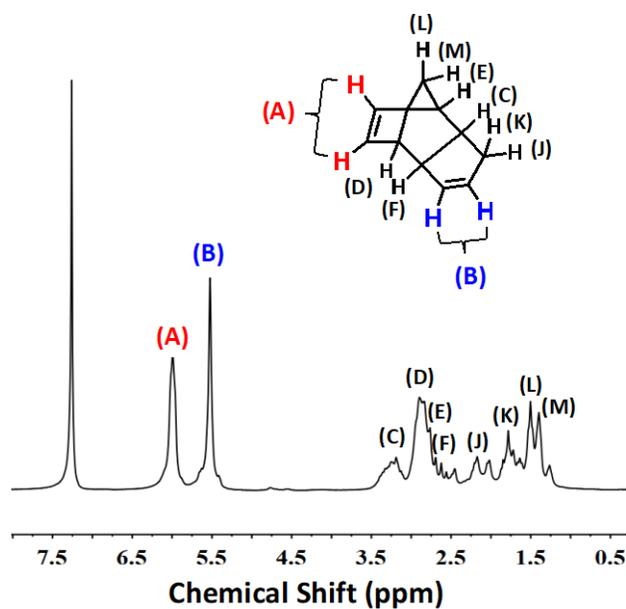
Figure 3.4. ^{1}H NMR spectra of DCPD extracted from SLA 3D-printed composite.

3.3.2.2. Scanning electron microscopy

The internal morphology of the SLA 3D printed self-healing composites was examined with scanning electron microscopy (SEM). The fracture plane (Figure 3.5) shows spherical voids of various sizes where microcapsules were present within the material prior to fracture. These voids are within the range of microcapsule diameters present in the specimen; where we note the different sizes of the voids are due to the 2D fracture plane representing a projection through different slices of the spherical microcapsules present in the 3D structure prior to fracture [49], [50]. The SEM image in Figure 3.5 also shows features in the fracture plane creating a tail-like appearance in the wake of the spherical voids. These tail markings originating from the voids have been previously attributed to the arresting of crack growth by the microcapsules, followed by rapid advancement of the crack front from the microcapsule-matrix interface [51].

73
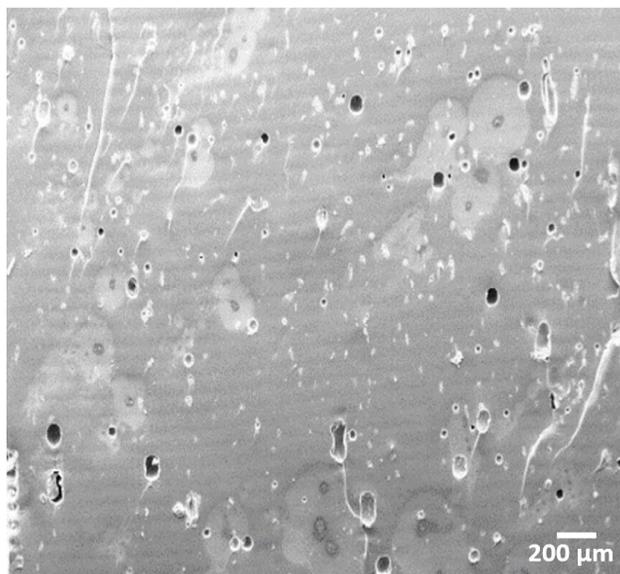
Figure 3.5. SEM image of self-healing composite showing spherical microcapsule voids.

3.3.2.3. X-ray Nano-CT

The presence of microcapsules in the 3D printed part was also examined using X-ray Nano-CT by examining the 3D image stack and 2D cross-sections of the 3D image (Figure 3.6B and 3.6C respectively). The particle size distribution frequency (number basis) of the microcapsules is extracted and shown in Figure 3.6D. The microcapsule size distribution could also be determined from the 3D image stack and was relatively broad, with 70% of microcapsules being 100–120 µm in diameter, and a mean diameter of 114 µm ± 25 µm. Overall, this microcapsule size distribution is in good agreement with that obtained from optical microscopy (mean diameter 129 µm ± 16 µm). A heatmap of the microcapsule centroid locations within the 3D printed cube is shown in Figure 3.6F and gives a generalized view of the microcapsule size distributions within 12.5 µm thick horizontal cross-sections of the 3D object. In this heatmap, a higher frequency of microcapsules is indicated by the color scale (blue to yellow—dark to light—for low to high microcapsule count). Microcapsules of diameter range from 100 to 130 µm show the highest

proportion though a majority of the specimen. This is expected as these are the most abundant microcapsules in the size distribution. The cumulative microcapsule probability distribution on a volume basis extracted from the centroid analysis is shown in Figure 3.6E. In this volume weighted distribution, the contribution of each microcapsule relates to its volume such that it is a good proxy for the quantity of healing fluid throughout the specimen. The obtained cumulative volume distribution curve generally tracks with a linear increase (shown via the solid blue line) along the vertical axis of the specimen. This indicates a relatively uniform distribution of microcapsule volume within the specimen and thereby a relatively uniform probability that a given random fracture would interact with microcapsules and thereby lead to localized self-healing.
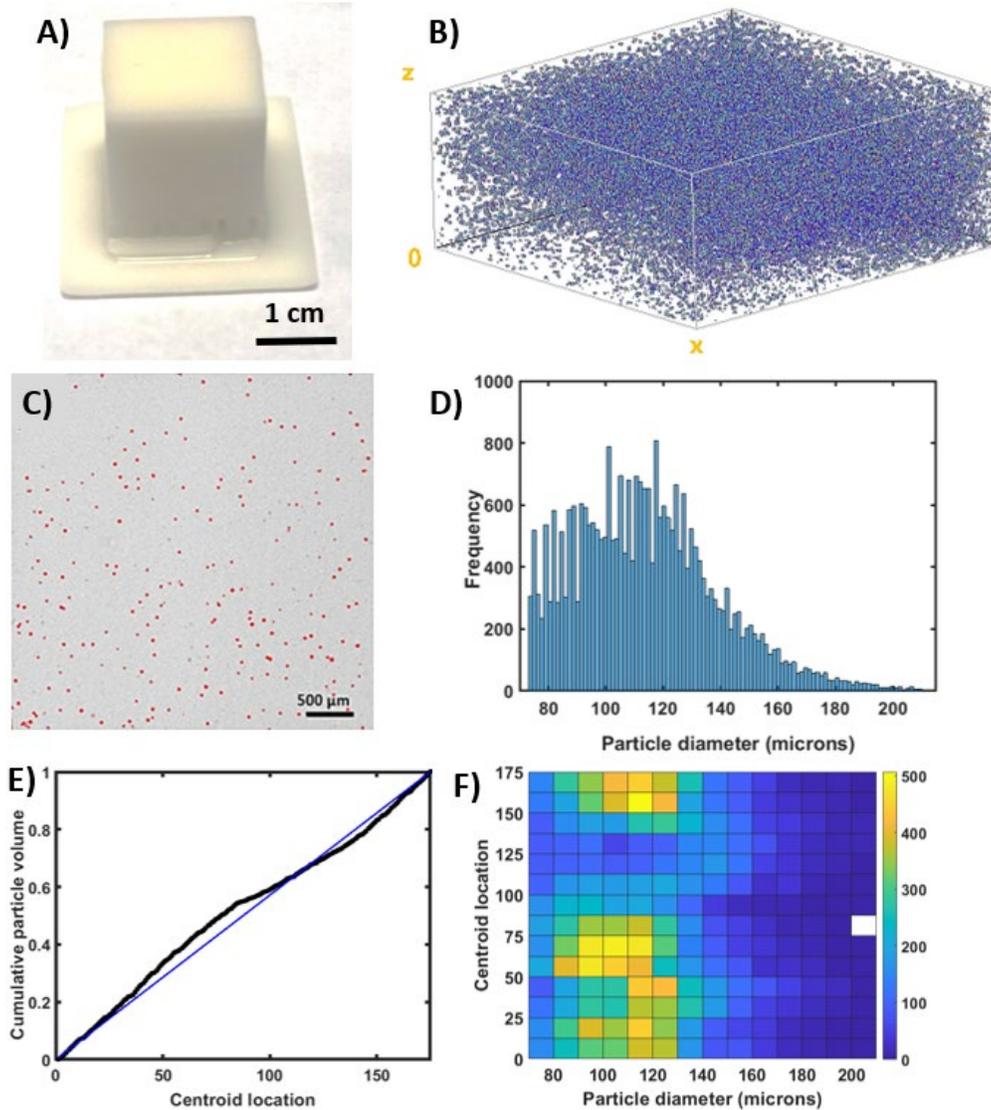
Figure 3.6. Visualization of X-ray Nano-CT data of SLA 3D printed composites: A) image of SLA 3D printed composite containing EPA-filled microcapsules, B) 3D visualization of microcapsules (colored) within the specimen (transparent) from X-ray Nano-CT data, C) x-y cross section of 3D Nano-CT image, D) size frequency distribution of microcapsules, E) (black line) cumulative particle distribution on volume basis for microcapsules located at geometric center of 3D printed composite, and (blue line) a linear cumulative particle volume vs centroid location fit corresponding to a uniform volume distribution, F) heatmap of microcapsules from blue to yellow (dark to light) for low to high microcapsule count.

Another consideration is the impact of microcapsules on surface features of the 3D printed specimens. Here, we examine the surface using the edge as visualized in each 2D x-y cross-section of the X-ray Nano-CT data. Representative images of the edge plane for specimens with and without capsules are shown in Figure 3.7. These images show an edge of the cubes (light gray) with the surrounding air (dark grey) for a single slice through the sample for comparison. Overall, we found little difference in the surfaces and the surface variation for both was generally within the voxel resolution of the images. To examine the surface across the entire sample the crossectional images were compiled into short videos scanning through the samples both with and without microcapsules.

A) Without capsules

1 mm

B) With capsules

Figure 3.7. X-ray Nano-CT image of the edge of SLA 3D printed specimens (A) without microcapsules, and (B) with microcapsules.

To interrogate the impact of microcapsules on finer features, specimens with more complex geometry, a square lattice grid structure containing internal voids, were printed with and without 5 wt.% EPA-containing microcapsules (see photograph in Figure 3.8). The specimen with microcapsules was printed into the desired structure without any change in printing parameters, confirming the ability to print more complex features containing microcapsules. A set of 3D X-ray CT images of each sample were obtained in order to visualize the microcapsules within the

structure and qualitatively compare the printed structures (Figure 3.8). Microcapsules are clearly evident in the specimen printed from the microcapsule-loaded resin and appear to be generally dispersed throughout the specimen. Here, we do note some visible differences between the surface structures between the specimens with and without microcapsules. The specimen printed with microcapsules appears to show additional defects compared to the specimen printed without microcapsules. Overall, this demonstrates the ability to incorporate microcapsules readily into complex geometries, but additional optimization of printing parameters as well as the microcapsule size and loading are necessary to ensure geometric integrity, if necessary, for more intricate structures with smaller geometric features in the printed specimens.
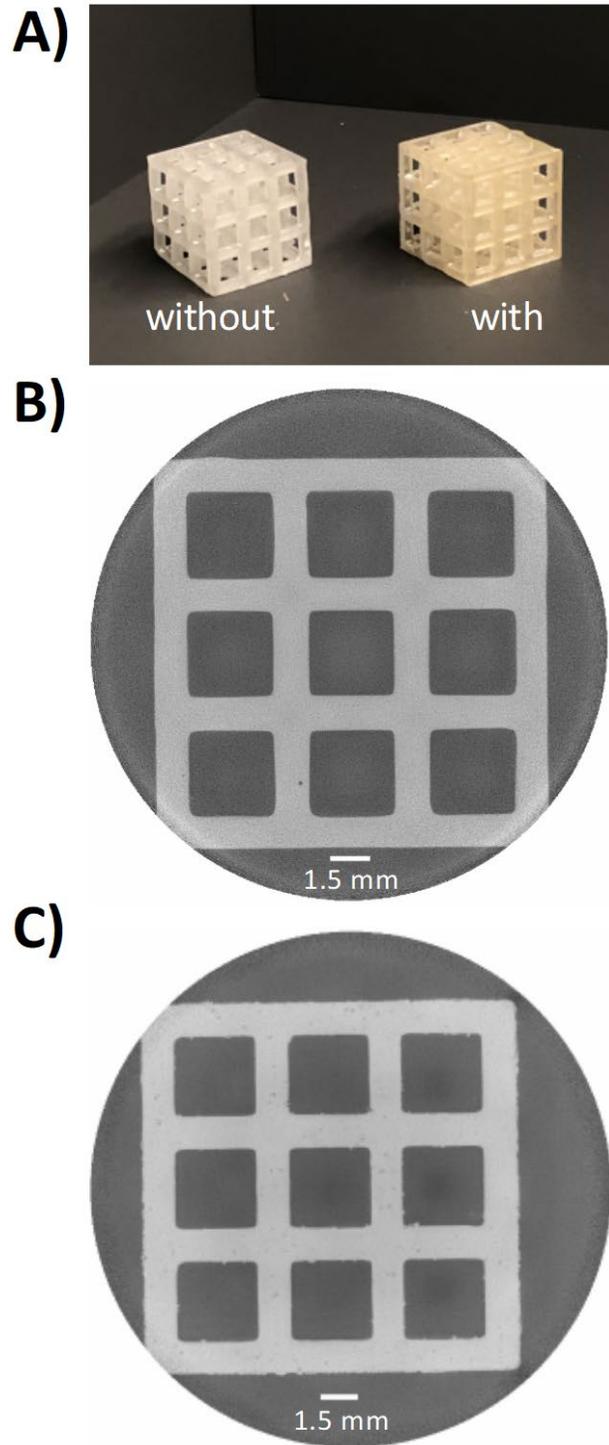
Figure 3.8. A) photographic image of 15 mm x 15 mm x15 mm SLA 3D printed grid lattice structures (left) without and (right) with EPA-filled microcapsules. Representative 2D slices from the 3D X-ray CT data for specimens B) without capsules and C) with capsules.

3.3.3. Physical Properties of SLA 3D printed composites

3.3.3.1. Dynamic mechanical analysis of SLA printed composites

The effect of the addition of microcapsules and catalyst on the storage modulus (E') and the glass transition temperature (Tg) of SLA printed composites was evaluated using dynamic mechanical analysis (DMA). As shown in Table 3.2, the addition of microcapsules slightly lowers the E' while Tg remained essentially unchanged. To investigate the extent of change in E' and Tg of SLA composites in the presence of capsules, mean and standard deviation of all values of both E' and Tg were determined to find the coefficient of variance (CV) across all measurements. CV was calculated as ratio of standard deviation to mean, thereby representing the extent of variation in relation to the mean. The CV for the E' and Tg are 0.067 and 0.066 respectively. CV for both the storage modulus and Tg are less than 0.1 (10 %), which is a typical metric for denoting negligible difference between values [52]. These low standard deviations and CVs indicate low spread of data such that the addition of microcapsules and catalyst resulted in negligible change in these physical properties of the SLA printed composites.

Table 3.2. Storage modulus and glass transition temperature of SLA 3D printed composites

Microcapsule Content (% w/w)	E' (MPa)	Tg (°C)
0	389 ± 14	62 ± 4
5	354 ± 18	61 ± 2

3.3.3.2 Self-healing efficiency of SLA 3D printed composites

The healing efficiencies of specimens with 5 wt.% sieved DCPD-containing microcapsules and 0.5 wt.% of catalyst were determined via Single Edge Notch Beam (SENB) fracture test. SENB fracture toughness tests provide an accurate protocol for investigating fracture behavior and healing efficiency of SLA printed self-healing composites. After the fracture event, specimens were allowed to heal at room temperature for 24 and 72 hours. These times were chosen to allow sufficient time for the healing and are commonly used temporal metrics in the literature for self-healing materials [46]-[48]. However, upon preliminary SENB testing it was difficult to control the length of the propagated crack of these photocured composites after the fracture event which tended to result in continued crack propagation through the width of the specimen. As the SENB test requires control over the initial crack length to target an approximate a/W value this behavior prevents the use of this test method for evaluating healing efficiency. To alleviate this issue a fracture relief defect (small hole of area 7.06 mm^2) was incorporated into the specimen in order to control the initial crack length and extract accurate fracture toughness from the SENB tests (Table 3.3).

Table 3.3. Fracture toughness before and after healing of photocured composites after 24 and 72 hours.

Capsule Loading (wt.%)	Pre-healing Fracture Toughness (MPa.m$^{1/2}$)	Post Healing Fracture Toughness (MPa.m$^{1/2}$)	Self-healing efficiency (%)	Post Healing Fracture Toughness (MPa.m$^{1/2}$)	Self-healing efficiency (%)
		24 hours		72 hours	
0	0.719 ± 0.08	-	-	-	-
5	0.524 ± 0.18	0.279 ± 0.07	53	0.384 ± 0.09	73

When first comparing the fracture toughness of the initial samples a 27% decrease in virgin fracture toughness and larger standard deviation was observed for the microcapsule-containing specimens compared to the specimens without microcapsules. Here, the spread was larger (especially for the microcapsule-containing specimens), however the resulting standard deviation ranges of the measured fracture toughness for these 3D printed specimens do overlap considerably. As observed with other composites, the microcapsules could be acting as defects in the polymer matrix, thus affecting fracture toughness [49], [50]. However, material healing was obtained for the microcapsule-containing specimens at both 24 and 72 hours with 53% and 73% of the pre-healing fracture toughness recovered after healing, respectively. 3D printed specimen, optical images of the crack developed after the fracture test, and its healing at 24 and 72 hours were obtained (Figure 3.9), clearly showing the initial healing of the fracture within 24 hours and complete sealing of the fracture at 72 hours. The increased healing efficiency with time is consistent with the literature on related self-healing materials [25], [53], [54], and this dependence

is mainly a consequence of the diffusion of polymer chains [53]. In future studies other strategies including microcapsule loading and manipulating microcapsule size distributions will be investigated toward further increasing the healing efficiency and pre-healing fracture toughness of these SLA 3D printed composites.
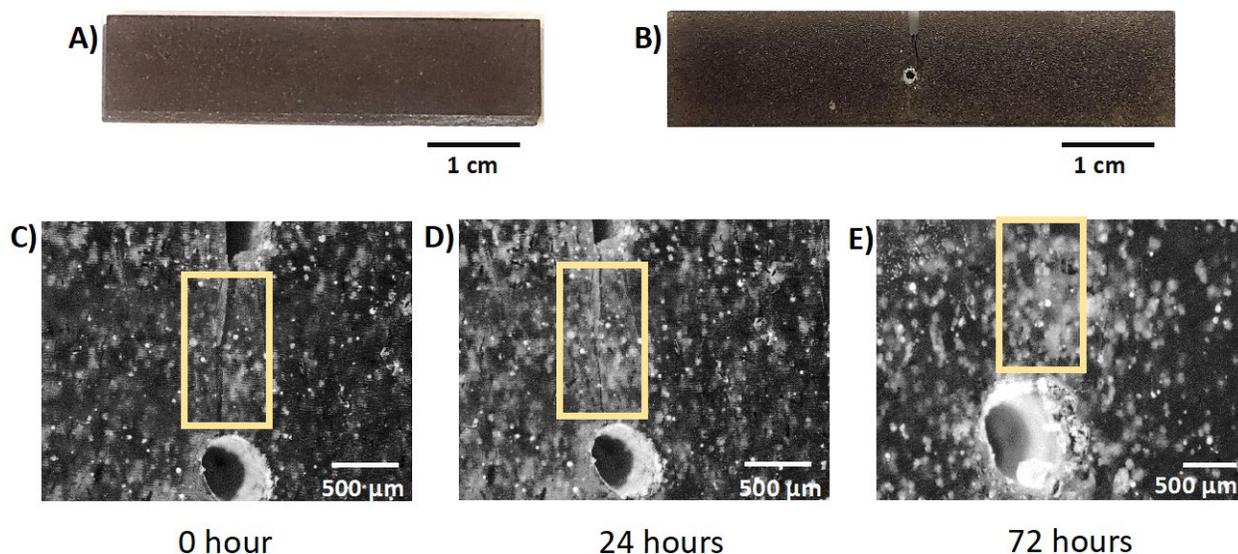
Figure 3.9. A) 3D printed composite structure containing DCPD-filled microcapsules and Grubbs' catalyst, B) pre-notched and pre-cracked 3D printed composite structure with a fracture relief defect, C) optical microscopic images of pre-notched and pre-cracked composite, D) and their crack healing in the photocured self-healing composite after 24 hours, E) and 72 hours.

3.4. Conclusion

In this work, we synthesized double-walled microcapsules encapsulating DCPD for incorporation in SLA 3D printed materials. This is a versatile platform for SLA 3D printing of self-healing thermoset materials as it does not require manipulation of the resin chemistry and has less reliance on compatibility with the healing fluid than a solvent healing-based microcapsule approach. The SLA 3D printing of commercial resin incorporating these self-healing microcapsules where the

microcapsules remain intact after printing is demonstrated. X-ray Nano-CT imaging confirms an essentially uniform distribution of microcapsules within SLA 3D printed cubes. This is desirable for self-healing composites to ensure a given fracture will trigger self-healing through interaction with embedded microcapsules. Self-healing efficiency was investigated using SENB tests where a healing efficiency of 73 % was achieved within 72 hours of fracture. The ability of the DCPD monomer to polymerize in the presence of catalyst after a fracture event at room temperature without external stimulus is an important consideration for application of these systems. This study provides a platform for extending material lifetimes of 3D printed materials via self-healing for recovery of structural integrity.

3.5. References

[1]   Schimpf, V.; Asmacher, A.; Fuchs, A.; Bruchmann, B.; Mülhaupt, R. Polyfunctional Acrylic Non-isocyanate Hydroxyurethanes as Photocurable Thermosets for 3D Printing. *Macromolecules* **2019**, *52* (9), 3288-3297. https://doi.org/10.1021/acs.macromol.9b00330.

[2]   Tofail, S.; Koumoulos, E.; Bandyopadhyay, A.; Bose, S.; O'Donoghue, L.; Charitidis, C. Additive manufacturing: scientific and technological challenges, market uptake and opportunities. *Mater. Today*. **2018**, *21* (1), 22-37. https://doi.org/10.1016/j.mattod.2017.07.001.

[3]   Hegde, M.; Meenakshisundaram, V.; Chartrain, N.; Sekhar, S.; Tafti, D.; Williams, C.; Long, T. 3D Printing All-Aromatic Polyimides using Mask-Projection Stereolithography: Processing the Nonprocessable. *Adv. Mater. Weinheim*. **2017**, *29* (31), 1701240. https://doi.org/10.1002/adma.201701240.

[4]   Zhao, Z.; Peng, F.; Cavicchi, K.; Cakmak, M.; Weiss, R.; Vogt, B. Three-Dimensional Printed Shape Memory Objects Based on an Olefin Ionomer of Zinc-Neutralized Poly(ethylene-co-methacrylic acid). *ACS Appl. Mater. Interfaces.* **2017**, *9* (32), 27239-27249. https://doi.org/10.1021/acsami.7b07816.

[5]   Shi, Q.; Yu, K.; Kuang, X.; Mu, X.; Dunn, C.; Dunn, M.;Wang, T.; Qi, H. Recyclable 3D printing of vitrimer epoxy. *Materials Horizons* **2017**, *4* (4), 598-607. https://doi.org/10.1039/c7mh00043j.

[6]   Moumen, A.; Tarfaoui, M.; Lafdi, K. Additive manufacturing of polymer composites: Processing and modeling approaches. *Composites Part B: Engineering* **2019**, *171*, 166-182. https://doi.org/10.1016/j.compositesb.2019.04.029.

[7]   Shinde, V.V.; Wang, Y.; Salek, M.D.; Auad, M.L.; Beckingham, L.E.; Beckingham, B.S. Material design for enhancing properties of 3D printed polymer composites for target applications. *Technologies* **2022**, *10*, 45. https://doi.org/10.3390/ technologies10020045.

[8]   Arnold, C.; Monsees, D.; Hey, J.; Schweyen, R. Surface Quality of 3D-Printed Models as a Function of Various Printing Parameters. *Materials (Basel, Switzerland).* **2019**, *12* (12), 1970. https://doi.org/10.3390/ma12121970.

[9]   Singh, R.; Zhang, M.; Chan, D. Toughening of a brittle thermosetting polymer: Effects of reinforcement particle size and volume fraction. *J. Mater. Sci.* **2019**, *37* (4), 781-788. https://doi.org/10.1023/A:1013844015493.

[10]   Sultan, J.; McGarry, F. Effect of rubber particle size on deformation mechanisms in glassy epoxy. *Polym.Eng. Sci.* **1973**, *13* (1), 29-34. https://doi.org/10.1002/pen.760130105.

[11]   Manzione, L.; Gillham, J.; McPherson, C. Rubber-modified epoxies. II. Morphology and mechanical properties. *J. Appl. Polym. Sci.* **1981**, *26* (3), 907-919. https://doi.org/10.1002/app.1981.070260314.

[12] Yee, A.; Pearson, R. Toughening mechanisms in elastomer-modified epoxies: Part 1 Mechanical studies. *J. Mater. Sci*. **1986**, *21* (7), 2462-2474. https://doi.org/10.1007/BF01114293.

[13] Toohey, K.; Sottos, N.; Lewis, J.; Moore, J.; White, S. Self-healing materials with microvascular networks. *Nat. Mater.* 2007, *6* (8), 581-585. https://doi.org/10.1038/nmat1934.

[14] Amstad, E. Capsules: Their Past and Opportunities for Their Future. *ACS Macro Lett*. **2017**, *6* (8), 841-847. https://doi.org/10.1021/acsmacrolett.7b00472.

[15] Bekas, D.; Tsirka, K.; Baltzis, D.; Paipetis, A. Self-healing materials: A review of advances in materials, evaluation, characterization and monitoring techniques. *Composites Part B: Engineering* **2016**, *87*, 92-119. https://doi.org/10.1016/j.compositesb.2015.09.057.

[16] Blaiszik, B.; Kramer, S.; Olugebefola, S.; Moore, J.; Sottos, N.; White, S. Self-Healing Polymers and Composites. *Annu. Rev. Mater. Res.* **2010**, *40* (1), 179-211. https://doi.org/10.1146/annurev-matsci-070909-104532.

[17] Wang, Z.; Lu, X.; Sun, S.; Yu, C.; Xia, H. Preparation, characterization and properties of intrinsic self-healing elastomers. *Materials Chemistry B*. **2019**, *7* (32), 4876-4926. https://doi.org/10.1039/c9tb00831d.

[18] Li, G.; Meng, H. Recent Advances in Smart Self-Healing Polymers and Composites. *Elsevier* **2015**, 1-407. https://doi.org/10.1016/C2013-0-16515-4.

[19] Yang, Y.; Lu, X.; Wang, W. A tough polyurethane elastomer with self-healing ability. *Materials & Design* **2017**, *127*, 30-36. https://doi.org/10.1016/j.matdes.2017.04.015.

[20] Gladman, A.; Celestine, A.; Sottos, N.; White, S. Autonomic Healing of Acrylic Bone Cement. *Adv. Healthc. Mater.* **2014**, *4* (2), 202-207. https://doi.org/10.1002/adhm.201570009.

[21] White, S.; Sottos, N.; Geubelle, P.; Moore, J.; Kessler, M.; Sriram, S.; Brown, E.; Viswanathan, S. Autonomic healing of polymer composites. *Nature* **2001**, *409* (6822), 794. https://doi.org/10.1038/35057232.

[22] Caruso, M.; Blaiszik, B.; Jin, H.; Schelkopf, S.; Stradley, D.; Sottos, N.; White, S.; Moore, J. Robust, Double-Walled Microcapsules for Self-Healing Polymeric Materials. *ACS Appl. Mater. Interfaces.* **2010**, *2* (4), 1195-1199. https://doi.org/10.1021/am100084k.

[23] Jones, A.; Watkins, C.; White, S.; Sottos, N. Self-healing thermoplastic-toughened epoxy. *Polymer* **2015**, *74*, 254-261. https://doi.org/10.1016/j.polymer.2015.07.028.

[24] Sanders, P.; Young, A.; Qin, Y.; Fancey, K.; Reithofer, M.; Guillet-Nicolas, R.; Kleitz, F.; Pamme, N.; Chin, J. Stereolithographic 3D printing of extrinsically self-healing composites. *Sci. Rep.* **2019**, *9* (1), 388. https://doi.org/10.1038/s41598-018-36828-9.

[25] Celestine, A.; Sottos, N.; White, S. Autonomic healing of PMMA via microencapsulated solvent. *Polymer* **2015**, *69*, 241-248. https://doi.org/10.1016/j.polymer.2015.03.072

[26] Brochu, A.; Evans, G.; Reichert, W. Mechanical and cytotoxicity testing of acrylic bone cement embedded with microencapsulated 2-octyl cyanoacrylate. *J. Biomed. Mater. Res. B.* **2013**, *102* (1), 181-189. https://doi.org/10.1002/jbm.b.32994.

[27]   Moniruzzaman, M.; Christogianni, P.; Kister, G. Self-Healing in Epoxy Thermoset Polymer Films Triggered by UV Light. *In Procedia Engineering* **2016**, *148*, 114-121. https://doi.org/10.1016/j.proeng.2016.06.472.

[28]   Szabó, T.; Telegdi, J.; Nyikos, L. Linseed oil-filled microcapsules containing drier and corrosion inhibitor – Their effects on self-healing capability of paints. *Prog. Org. Coat.* **2015**, *84*, 136-142. https://doi.org/10.1016/j.porgcoat.2015.02.020.

[29]   Behzadnasab, M.; Esfandeh, M.; Mirabedini, S.; Zohuriaan-Mehr, M.; Farnood, R. Preparation and characterization of linseed oil-filled urea–formaldehyde microcapsules and their effect on mechanical properties of an epoxy-based coating. *Colloid. Surface. A.* **2014**, *457*, 16-26. https://doi.org/10.1016/j.colsurfa.2014.05.033.

[30]   De Espinosa, L. M.; Fiore, G. L.; Weder, C.; Johan Foster, E.; Simon, Y. C. Healable Supramolecular Polymer Solids. *Progress in Polymer Science. Elsevier* **2015**, *49-50*, 60-78 https://doi.org/10.1016/j.progpolymsci.2015.04.003.

[31]   Blaiszik, B.; Baginska, M.; White, S.; Sottos, N. Autonomic Recovery of Fiber/Matrix Interfacial Bond Strength in a Model. *Compos. Adv. Funct. Mater*. **2010**, *20* (20), 3547-3554. https://doi.org/10.1002/adfm.201000798.

[32]   Uzcategui, A.; Muralidharan, A.; Ferguson, V.; Bryant, S.; McLeod, R. Understanding and Improving Mechanical Properties in 3D printed Parts Using a Dual-Cure Acrylate-Based Resin for Stereolithography. *Adv. Eng. Mater.* **2018**, *20* (12), 1800876. https://doi.org/10.1002/adem.201800876.

[33]   Dizon, J.; Espera, A.; Chen, Q.; Advincula, R. Mechanical characterization of 3D-printed polymers. *Addit. Manuf.* **2018**, *20*, 44-67. https://doi.org/10.1016/j.addma.2017.12.002.

[34] Postiglione, G.; Alberini, M.; Leigh, S.; Levi, M.; Turri, S. Effect of 3D-printed microvascular network design on the self-healing behaviour of crosslinked polymers *ACS Appl. Mater. Inter.* **2017**, *9* (16), 14371-14378. https://doi.org/10.1021/acsami.7b01830.

[35] Deng, X.; Attalla, R.; Sadowski, L. P.; Chen, M.; Majcher, M. J.; Urosev, I.; Yin, D.-C.; Selvaganapathy, P. R.; Filipe, C. D. M.; Hoare, T. Autonomously Self-Adhesive Hydrogels as Building Blocks for Additive Manufacturing. *Biomacromolecules.* **2017**, *19*, 62–70. https://doi.org/10.1021/acs.biomac.7b01243.

[36] Almutairi, M.; Aria, A.; Thakur, V.; Khan, M. Self-Healing Mechanisms for 3D-Printed Polymeric Structures: From Lab to Reality. *Polymers* **2020**, *12* (7), 1534. https://doi.org/10.3390/polym12071534.

[37] Yu, K.; Xin, A.; Du, H.; Li, Y.; Wang, Q. Additive manufacturing of self-healing elastomers. *NPG Asia Materials* **2019**, *11* (1), 7. https://doi.org/10.1038/s41427-019-0109-y.

[38] Liu, S.; Li, L. Ultra-stretchable and Self-healing Double Network Hydrogel for 3D Printing and Strain Sensor. *ACS Appl. Mater. Inter.* **2017**, *9* (31), 26429-26437. https://doi.org/10.1021/acsami.7b07445.

[39] Nadgorny, M.; Xiao, Z.; Connal, L. 2D and 3D-printing of self-healing gels: design and extrusion of self-rolling objects. *Mol. Syst. Des. Eng.2.* **2017**, *2* (3), 283-292. https://doi.org/10.1039/c7me00023e.

[40] Highley, C.; Rodell, C.; Burdick, J. Direct 3D Printing of Shear-Thinning Hydrogels into Self-Healing Hydrogels. *Adv. Mater.* **2015**, *27* (34), 5075-5079. https://doi.org/10.1002/adma.201501234.

[41] Jang, T.; Jung, H.; Pan, H.; Han, W.; Chen, S.; Song, J. 3D printing of hydrogel composite systems: Recent advances in technology for tissue engineering. *Int. J. Bioprinting.* **2018**, *4* (1). https://doi.org/10.18063/IJB.v4i1.126.

[42] Neuser, S.; Michaud, V. Fatigue Response of Solvent-Based Self-Healing Smart Materials. *Exp. Mech.* **2013**, *54* (2), 293-304. https://doi.org/10.1007/s11340-013-9787-5.

[43] Postiglione, G.; Turri, S.; Levi, M. Effect of the Plasticizer on the Self-Healing Properties of a Polymer Coating Based on the Thermoreversible Diels–Alder Reaction*. Prog. Org. Coat.* **2015**, *78*, 526–531. https://doi.org/10.1016/j.porgcoat.2014.05.022.

[44] Wu, D. Y.; Meure, S.; Solomon, D. Self-Healing Polymeric Materials: a Review of Recent Developments. *Prog. Polym. Sci*. **2008**, *33*, 479–522. https://doi.org/10.1016/j.progpolymsci.2008.02.001.

[45] Sharma, A.; Pandey, A.; Shukla, D.; Pandey, K. Effect of Self-Healing Dicyclopentadiene Microcapsules on Fracture Toughness of Epoxy. *Materials Today: Proceedings* **2018**, *5* (10), 21256-21262. https://doi.org/10.1016/j.matpr.2018.06.526.

[46] Patrick, J.; Sottos, N.; White, S. Microvascular based self-healing polymeric foam. *Polymer* **2012**, 53(19), 4231-4240. https://doi.org/10.1016/j.polymer.2012.07.021.

[47] Gandini, A.; Cheradame, H. Advances in Polymer Science. Adv. Polym. Sci. **1980**, *34–35*. https://doi.org/10.1038/216619a0.

[48] Aniskevich, A.; Kulakov, V.; Bulderberga, O.; Knotek, P.; Tedim, J.; Maia, F.; Leisis, V.; Zeleniakiene, D. Experimental characterisation and modelling of mechanical behaviour of microcapsules. *J. Mater. Sci*. **2020**, *55* (27), 13457-13471. https://doi.org/10.1007/s10853-020-04925-8.

[49] Brown, E.; White, S.; Sottos, N. Microcapsule induced toughening in a self-healing polymer composite *J. Mater. Sci.* **2004**, *39* (5), 1703-1710. https://doi.org/10.1023/B:JMSC.0000016173.73733.dc.

[50] Albdiry, M.; Yousif, B. Toughening of brittle polyester with functionalized halloysite nanocomposites. *Compos. B. Eng.* **2019**,*160*, 94-109. https://doi.org/10.1016/j.compositesb.2018.10.032.

[51] Yang, C.; Huh, H.; Hahn, H. Investigation of effective material properties in composites with internal defect or reinforcement particles. *Int. J. Solids Struct.* **2005**, *42* (24-25), 6141-6165. https://doi.org/10.1016/j.ijsolstr.2005.06.094.

[52] Romano, F.; Ambrosano, G.; Magnani, M.; Nouer, D. Analysis of the coefficient of variation in shear and tensile bond strength tests. *J. Appl Oral Sci.* **2005**, *13* (3), 243-246. https://doi.org/10.1590/s1678-77572005000300008.

[53] Wool, R.; O'Connor, K. A theory crack healing in polymers. *J. Appl. Phys.* **1981**, *52* (10), 5953-5963. https://doi.org/10.1063/1.328526.

[54] Jud, K.; Kausch, H. Load transfer through chain molecules after interpenetration at interfaces. *Polym. Bull.* **1979**, *1* (10), 697-707. https://doi.org/10.1007/BF00255445.

Chapter 4

Self-healing of High Impact Polystyrene (HIPS) Composites

4.1. Introduction

Polymer composites are integral materials used by a wide range of industries due to their tunability, and enhanced structural and functional properties [1]-[3]. These amenable material properties offer many advantages of polymer composites; low weight, corrosion resistance, and improved mechanical properties with lower cost [4]-[6]. These advantages have led to the widespread application of polymer composites in different industrial sectors, including biomedicine, aerospace, defense, automotive, construction, and many others [7]-[10]. Although composite materials typically increase a polymer material's durability by reinforcing it with particles or fibers, a major concern has arisen regarding accumulation of polymer waste in the environment [11]-[13]. This concern has compelled researchers to investigate environmentally friendly polymer materials associated with cleaner manufacturing processes [14]-[16]. Moreover, conventional thermoset-based polymer composites with their covalently crosslinked networks directly result in limited

recyclability, and increased plastic waste [17]-[19]. Researchers are therefore looking for replacements for thermoset polymer composites.

Recycling and reprocessing of thermoplastic materials can generally be performed from a technological perspective as they can be remelted and reshaped with the provision of heat [20], [21]. Plastic recycling can reduce environmental problems, saving both materials, energy, and cost. These properties coupled with their flexibility, durability, user-friendly design, and low density give thermoplastic composite materials' the potential to become viable replacements for some thermoset materials [22], [23]. While thermoplastic composites show tremendous promise for recyclability at the end of their useful life [24], they show relatively poor mechanical strength and dimensional stability compared to crosslinked polymer composites, metals, and ceramics leading to shorter useful lifetimes [25], [26]. Although researchers have made various attempts to improve their mechanical strength by, for example, adding reinforcing fibers, very few studies have investigated the incorporation of self-healing properties to thermoplastic polymer composites to extend material lifespan and durability [27]-[30].

Self-healing is a material's ability to repair damage and restore lost properties, using resources inherently available to a material system [31]-[33]. Self-healing materials offer increased safety, reliability, and strength to structural components in which damage detection is often difficult or repair and maintenance after component failure are costly [34]. Self-healing materials can be categorized based on their damage response as either non-autonomous or autonomous. Non-autonomous self-healing systems require an external stimulus, such as heat or light, to trigger and execute the self-healing process [35], while autonomous self-healing systems do not require any additional stimulus for the self-healing process to be initiated and material damage such as crack growth is enough to trigger the self-healing process [36]-[38]. The primary autonomous healing

methods in polymer composites focus either on the introduction of dynamic bonds in the macromolecular backbone, i.e., intrinsic healing, or the incorporation of encapsulated healing agents in the form of microcapsules or vascular networks into the bulk polymer, i.e., extrinsic healing [39]-[45]. When the material is fractured, microcapsules or vascular networks are ruptured and release their self-healing contents into the crack plane, where further reaction or interactions with the host material initiates the process of self-healing [35].

A microcapsule-based self-healing system is highly localized and can heal a developing crack right where it is initiated. White et al. were the first to demonstrate the dicyclopentadiene (DCPD)-Grubbs' first-generation catalyst-based self-healing system based on ring-opening metathesis polymerization [31]. Solvent-based self-healing is also an example of a microcapsule-based system that uses a polymer's latent functionality to initiate self-healing. In a solvent-based system, a crack in a microcapsule-loaded polymer matrix releases solvent to the crack site, locally dissolving the polymer, leading to rebonding of fractured surfaces upon evaporation of solvent [46]. Solvent-based self-healing in thermoset epoxy materials has been explored by Caruso et. al. where fracture in the specimen was healed by solvent welding through the reaction of residual monomer [46]. Solvent-based self-healing in thermoplastic poly(methyl methacrylate) (PMMA) has been demonstrated by Celestine et. al. to investigate fracture toughness recovery in the presence of solvent-filled microcapsules [30]. Importantly, the solvent-based healing mechanism is efficient, simple, and cost effective as no additional catalyst or hardener is required [30], [46].

This work evaluates the self-healing performance of the thermoplastic high impact polystyrene (HIPS) via solvent-filled microcapsules. High impact polystyrene (HIPS) is a low-cost polymer with properties leading to easy machining and fabrication. It has low tensile strength for structural application but high impact strength, making it useful when low-cost impact strength,

machinability, and fabrication are required in a product [47]-[49]. Therefore, high impact polystyrene (HIPS) is a potential candidate to incorporate self-healing properties to fabricate composite materials of high toughness and self-healing ability. Here, we utilize ethyl phenyl acetate (EPA)-containing microcapsules that are synthesized via an emulsion polymerization process. Ethyl phenylacetate is a low toxicity, non-genotoxic, green solvent that is found in a wide variety of consumer products, including perfume and food, including beer, honey, citrus fruits, and whiskey [50], [51]. HIPS specimens embedded with ethyl phenylacetate (EPA) microcapsules are then fabricated via compression molding at elevated temperatures. The survivability of the microcapsules after this molding process is evaluated, and the mechanical properties and healing performance of composites at varied microcapsule concentrations are investigated. Incorporating self-healing properties in thermoplastic polymer composites can advance the development of safer, long-lasting, low cost and sustainable materials with a wide range of properties and functionalities for their application in packaging, transportation, electronics, and coatings.

4.2. Experimental Methods

4.2.1. Materials

All chemicals and solvents were used as received unless otherwise noted. Ethyl phenylacetate (EPA) was purchased from Sigma-Aldrich. Polyurethane (PU) prepolymer (Desmodur L 75) was donated by Covestro. Desmodur L 75 is a prepolymer solution in ethyl acetate with a reported equivalent weight of 315 g and an isocyanate content of 13.3 ± 0.4 wt.%. Ethylene-maleic anhydride (EMA) copolymer (Zemac-400) powder was purchased from Polyscience Inc. and used as a 2.5 wt.% aqueous solution. Dichloromethane, urea, ammonium chloride (NH_4Cl), sodium hydroxide (NaOH) pellets, and tetrahydrofuran were purchased from BDH chemicals.

Hydrochloric acid (95% purity) was purchased from Merck Chemicals. 0.5 N NaOH and 0.5 M hydrochloric acid solution were prepared and used to adjust the pH of the emulsion. All solvents and chemicals used for the preparation of EMA solution, acid and base solutions and 1-octanol were of analytical grade. Formaldehyde solution (formalin, 37 w/v %) was purchased from BTC chemicals. 1-Octanol was purchased from Fischer Chemicals. High Impact Polystyrene (HIPS) thermoplastic polymer pellets were purchased from 3DXTech. Deuterated chloroform ($CDCl_3$) was purchased from EMD Millipore.

4.2.2. Preparation of PU-UF microcapsules with EPA core fluid

Polyurethane-poly(urea-formaldehyde) (PU-UF) double-walled microcapsules containing EPA were synthesized using an in-situ interfacial polymerization technique developed by Caruso *et al.*[52] Briefly, 2.5 wt.% of poly(ethylene-alt-maleic anhydride), EMA, in water was prepared by adding 3.75 g of EMA to 150 ml of water and stirring for 24 hours. After the solution was fully dissolved, 5 g urea, 0.5 g ammonium chloride and 0.5 g resorcinol were added to the solution. Three grams (3 g) of PU (Desmodur L-75) was dissolved in 20 ml of dichloromethane in a water bath maintained at 80 °C and added to the urea solution. Solution pH was maintained between 2.5 to 3 using a sodium hydroxide solution to avoid demulsification. 60 ml of ethyl phenylacetate, EPA, was slowly added, and the solution was stirred continuously for 60 minutes. Finally, 12.7 g of formaldehyde (formalin, 37 w/v %) in an aqueous solution was added. The reaction batch was then heated to 55 °C using a temperature controlled hot plate and stirred at 500 rpm for 2 hours. 200 ml DI water was added to the solution to ensure an emulsion of microcapsules was maintained, and the microcapsule mixture was heated for a further two hours. Finally, the batch was cooled to room temperature, and microcapsules were separated using filter paper with a coarse-fritted funnel under vacuum. Microcapsules were washed in 200 ml of water, isolated via vacuum filtration, and dried

for 24-72 hours in a vacuum oven at room temperature (24-27 °C). Microcapsule average diameter and the presence of self-healing fluid were examined via optical microscopy using an Olympus 52x7 microscope with Cellsens software. Both thermogravimetric analysis (TGA) and differential scanning calorimetry (DSC) were performed to evaluate the thermal stability of the microcapsules.

4.2.3. Preparation of self-healing high impact polystyrene (HIPS)

Microcapsule-loaded HIPS samples were produced via compression molding as follows. Dried commercial HIPS pellets were mixed with microcapsules in concentrations ranging from 0 - 7.5 wt.% and the mixture added to a stainless-steel mold. The closed mold was placed in a Carver (Model 4389) manual heated press and the temperature maintained at 180 °C for 5 minutes while applying pressure. The heat was then turned off and the mold was allowed to cool to room temperature. Specimens were cut to their final dimensions of 50 mm x 10 mm x 2.45 mm for thermomechanical and mechanical characterization using a Buehler Isomet 1000 precision cutter.

4.2.4. Characterization by ^{1}H-NMR Spectroscopy

^{1}H-NMR spectrum of the purchased high impact polystyrene copolymer was acquired using a 500 MHz Bruker Neo NMR spectrometer using deuterated chloroform as the solvent (30 mg/mL) and 64 scans. Microcapsule survivability in the self-healing HIPS composite specimens was evaluated via the release of healing fluid (EPA) after mechanically crushing the specimens. For example, compression molded HIPS specimens containing 7.5 wt.% microcapsules were physically crushed and rinsed with $CDCl_3$. The $CDCl_3$ rinse was collected, loaded into an NMR tube, and characterized using low-field (60 MHz) ^{1}H-NMR spectroscopy, collected on an Oxford Instruments Pulsar 60 MHz spectrometer using 256 number of scans.

4.2.5. Characterization by thermogravimetric analysis and differential scanning calorimetry

Thermogravimetric analysis (TGA) was conducted on microcapsule-loaded HIPS specimens to confirm the presence of intact microcapsules after processing, using a TA Instruments Q500-0875 TGA instrument from 10 °C to 500 °C via a 10 °C/min ramp in a nitrogen gas atmosphere. Differential scanning calorimetry (DSC) analysis was also performed to analyze changes in thermal properties of the microcapsule-containing HIPS composite specimens using a TA Instruments Q20-3095 differential scanning calorimeter from 10 °C to 270 °C via a 10 °C/min ramp in a nitrogen gas atmosphere.

4.2.6. Flexure testing

Three-point bend flexure tests were performed on prepared self-healing HIPS specimens to examine the effect of microcapsule concentration on mechanical properties such as flexural strength and modulus. Tests were conducted under displacement control using a screw-driven 5 kN Instron test frame (Model 5565) with a support span of 35 mm, as per ASTM D790.[53] Specimens measuring 50 mm x 10 mm x 2.45 mm were loaded at a constant displacement rate of 3 mm/min. Load and displacement data were collected at 0.1 s intervals. Flexural stress (σ_f) and flexural strain were calculated as per ASTM D790 [53]. Flexural modulus and strength were determined from plots of flexural stress vs flexural strain. Four replicates were analyzed for each sample and the average and standard deviations computed and reported.
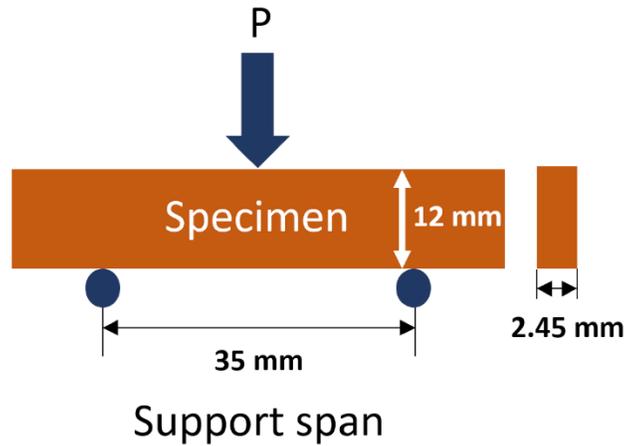
Figure 4.1. Flexure test specimen geometry and configuration where *P* is the fracture load (N).

4.2.7. Dynamic Mechanical Analysis

Thermomechanical behavior of prepared self-healing composites was characterized by dynamic mechanical analysis (DMA) using a TA instruments RSA III dynamic mechanical analyzer. Storage modulus (E') at room temperature and glass transition temperature (*Tg,* extracted as the peak in tan delta) of specimens were determined using a dynamic temperature ramp test with a frequency of 1 Hz and heating rate of 5 °C/min for a temperature range 28 °C to 130 °C. Four replicates were analyzed for each sample and the average and standard deviations computed and reported.

4.2.8. Fracture testing

The effect of the microcapsules on fracture toughness, K_Q, of HIPS composite was evaluated using the single-edge notched bend (SENB) test as per ASTM D5045 [54]. HIPS specimens (50 mm x 10 mm x 2.45 mm) with increasing concentrations of microcapsules were first pre-notched using a diamond tipped saw blade. A natural crack was then generated by tapping a fresh razor blade

placed in the notch. A fracture relief defect (small hole of area ~7 mm^2) was incorporated into the specimens to control the initial crack length and maintain crack length to width (*a/W*) ratio between 0.45 and 0.55. The initial crack length in each specimen was approximately 5 mm, corresponding to *a/W* = 0.5. Displacement controlled SENB tests were performed using the 1 kN Instron test frame with a displacement rate of 5 mm/min. The fracture toughness was calculated as

$$K_Q = \left(\frac{P_Q}{BW^{\frac{1}{2}}}\right) f(x) \tag{1}$$

$$f(x) = 6x^{1/2} \frac{[1.99 - x(1-x)(2.15 - 3.93 + 2.7x^2)]}{(1+2x)(1-x)^{3/2}} \tag{2}$$

where, K_Q is the fracture toughness, P_Q is the fracture load (N), *B* is the specimen thickness (cm), *W* is the specimen width (cm), and *x* is the crack to width ratio (*a/W*). The healing efficiency of the self-healing HIPS was investigated by allowing the fractured specimens to heal undisturbed for 24 and 72 hours and then performing a second fracture test. Healing efficiency, η, was calculated as the ratio of the healed fracture toughness (K_{Ic}^{healed}) to the virgin (initial) fracture toughness (K_{Ic}^{virgin}) as shown in Equation 3. Five replicates were analyzed for each sample and the average and standard deviations computed and reported.

$$\eta\ (\%) = \frac{(K_Q^{healed})}{(K_Q^{virgin})} \times 100 \tag{3}$$
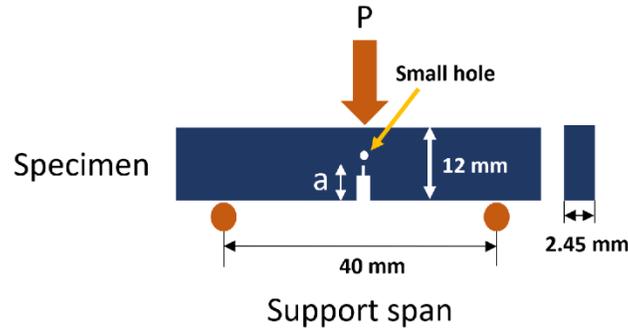
Figure 4.2. Fracture test specimen geometry and configuration where *a* is the initial crack length and *P* is the fracture load (N).

4.3. Results and Discussion

4.3.1. Synthesis and Characterization of PU-UF microcapsules with EPA self-healing fluid

Polyurethane-poly (urea-formaldehyde) (PU-UF) double-walled microcapsules containing EPA were synthesized using an in-situ emulsion polymerization technique developed by Caruso *et al.* [52]. This method satisfies the criteria necessary for successful incorporation of microcapsules in self-healing material systems, such as isolation of the healing liquid, good bonding with the matrix material due to better mechanical interlocking of capsules with polymer matrix, together with excellent microcapsule rupture and release of healing material into the crack plane upon damage [31], [35], [45], [52]. In addition, this method fabricates microcapsules with thicker and more robust shell walls as compared to single walled microcapsules (average shell wall thickness of 530 nm ± 30 nm for double-walled microcapsules compared to 175 nm ± 33 nm for single-walled as previously analyzed by Caruso *et. al.*), which is critically important in obtaining long term microcapsule stability at elevated temperatures as those in fabrication and processing of polymer composites [52], [55]-[57]. An optical micrograph of the as-synthesized microcapsules is shown in Figure 3A. The presence of healing fluid is confirmed by crushing the microcapsules and

optically observing the release of healing fluid (Figure 3B). Microcapsule size distribution was obtained by extracting microcapsule diameters from optical micrographs. To determine the microcapsule size distribution, the diameter of 100 randomly selected microcapsules were measured from these optical images. The particle size distribution of these as-synthesized microcapsules is quite broad with microcapsule diameters varying from 170 to 400 μm with an average diameter of 268 μm ± 49 μm, shown in Figure 4.3C.
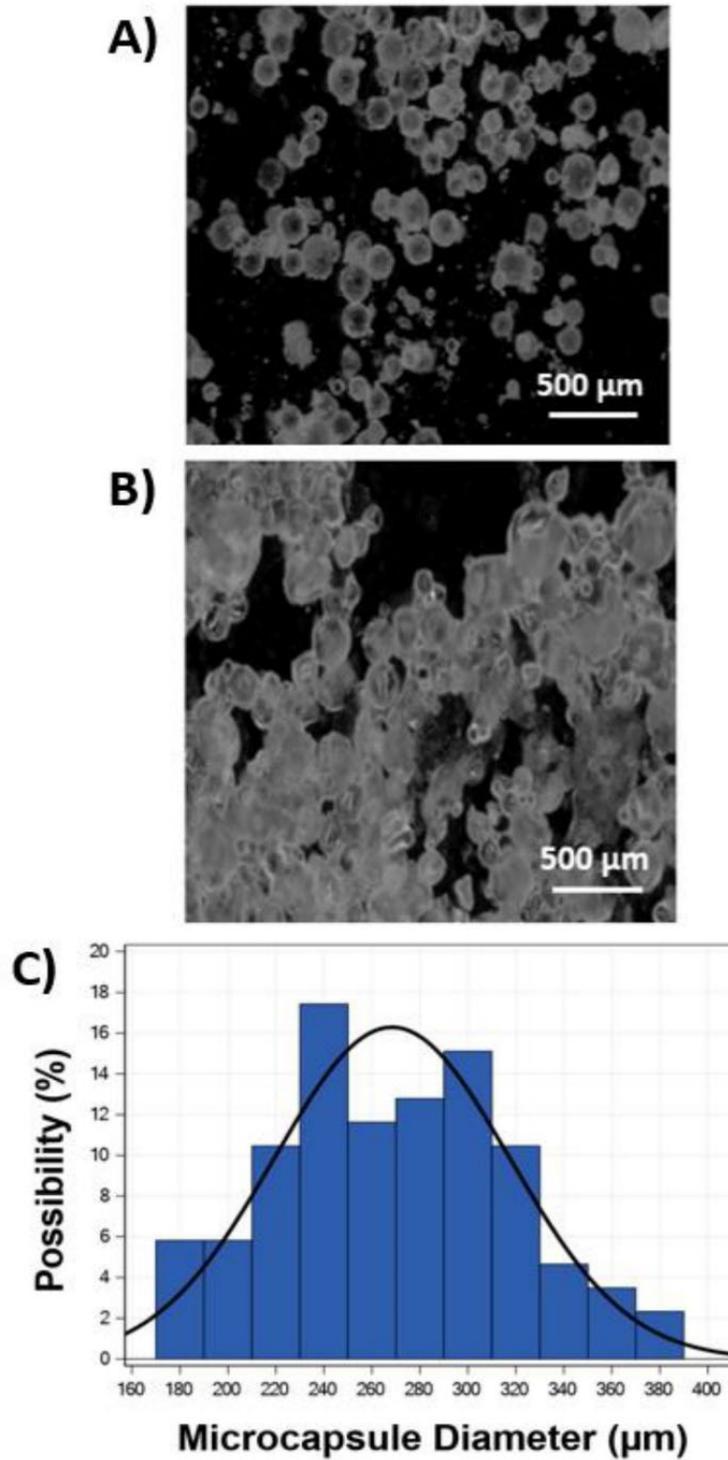
Figure 4.3. Microscopic images of EPA filled microcapsules: A) as synthesized, B) after compression, and C) particle size distribution (average diameter and standard deviation: 268 μm ± 49 μm).

TGA was performed to analyze the thermal stability of the EPA microcapsules (Figure 4.4). The microcapsules remain thermally stable up to a temperature of approximately 210 °C, after which there is a precipitous drop in sample weight with 5 wt.% loss observed at 225 °C and 95 wt.% loss occurring by 272 °C. We attribute this dramatic weight loss to microcapsules' rupture and loss of EPA at and above EPA's boiling point (~229 °C). The vaporization and rapid expansion of the EPA lead to a loss of microcapsule integrity and correspondingly EPA mass loss from the sample; note EPA is the primary contributor to microcapsule mass. This observed mass loss due to vaporization of the healing fluid (here EPA) can also be used to verify the presence of intact microcapsules in the HIPS composite.
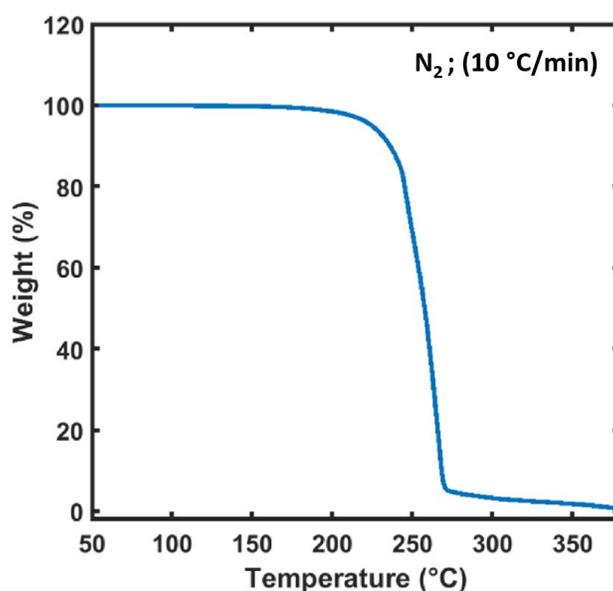
Figure 4.4. Thermogravimetric (TGA) plot of thermal behavior of EPA microcapsules.

4.3.2. Thermal analyses of compression molded self-healing HIPS composites.

Characterization of HIPS composites with embedded microcapsules by TGA was performed to evaluate the impact of microcapsules on thermal stability (Figure 4.5A). The thermogram for

virgin HIPS (0 wt.%) is stable and no significant weight loss is observed until above 300 °C; 5 wt.% loss is observed at 385 °C followed by thermal degradation of the virgin HIPS. Previous studies have found similar thermogravimetric results for virgin HIPS where thermal decomposition was observed between 340 – 490 °C [49], [58]. For samples with embedded EPA microcapsules, a distinctive slight weight loss is observed beginning at lower temperatures with more pronounced weight loss occurring at and above the boiling point of EPA (~229 °C). The relative magnitude of the observed weight loss increases with increasing microcapsule content (as expected based on the TGA characterization of microcapsules discussed above) and provides evidence for the presence and survival of intact microcapsules in the HIPS composites after compression molding.
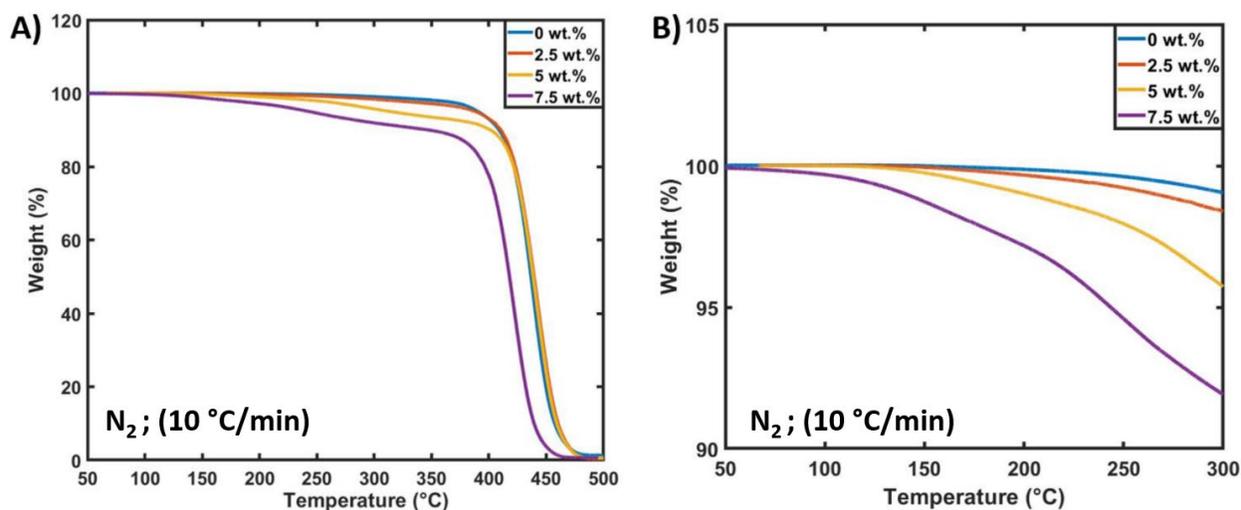
Figure 4.5. TGA thermograms of compression molded HIPS composites with increasing microcapsule concentrations (0, 2.5, 5.0, and 7.5 wt.%).

A clearer picture of this region of initial mass drop is gained by focusing on the initial 10 wt.% loss up to 300 °C as shown in Figure 4.5B. The HIPS sample without microcapsules is thermally stable up to 300 °C with less than 1 wt.% loss at 300 °C. The HIPS composite with 2.5

wt.% microcapsules is also quite stable with only 2 wt.% loss up to 300 °C. This mass loss is attributed to the loss of EPA fluid through vaporization, microcapsule rupture, and EPA release, as it mainly occurs near EPA's boiling point. Analogous behavior is observed for the HIPS composites with 5 wt.% microcapsules; only 3 wt.% loss up to 270 °C and 5 wt.% loss at around 300 °C. However, the TGA thermogram for the HIPS sample with 7.5 wt.% microcapsules displays a significant weight loss beginning around 100 °C which is possibly due to the presence of moisture in the sample. Afterward, a larger mass loss (approximately 6.5 wt.%) is observed in the range of 150 to 270 °C which we attribute to the loss of EPA from the sample. Overall, the weight loss in each of these samples corresponds roughly to their microcapsule content (and thereby primarily EPA content). Lastly, no appreciable difference in thermal behavior of the composite samples with and without microcapsules is observed via differential scanning calorimetry (DSC), where analogous glass transition temperatures (approximately 100 °C) are observed (Figure 4.6).
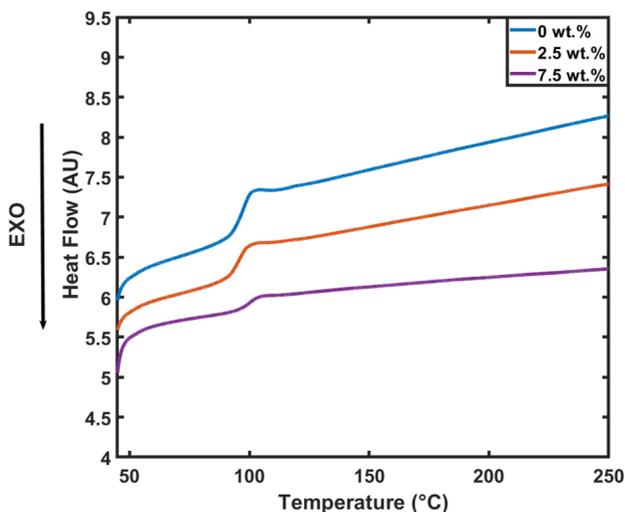
Figure 4.6. DSC thermograms for HIPS composites with increasing microcapsule concentration (0, 2.5, 7.5 wt.%).

4.3.3. HIPS characteristics and Microcapsule survivability via ^{1}H-NMR Spectroscopy.

In order to characterize the procured HIPS composition and polybutadiene microstructure, the as-received HIPS was examined using ^{1}H-NMR spectroscopy; Figure 4.7. Both the allylic polybutadiene peaks (4.8 - 5.6 ppm) and the aromatic polystyrene peaks (6.3-7.2 ppm) are clearly visible [59]. From the known proton assignments and extracted integrals, the HIPS contains 6 % polybutadiene with a microstructure consisting of 93 % 1,4-addition; both of which are within the typical range for HIPS. This polybutadiene microstructure corresponds to an expected glass transition temperature of approximately -97 °C [60].
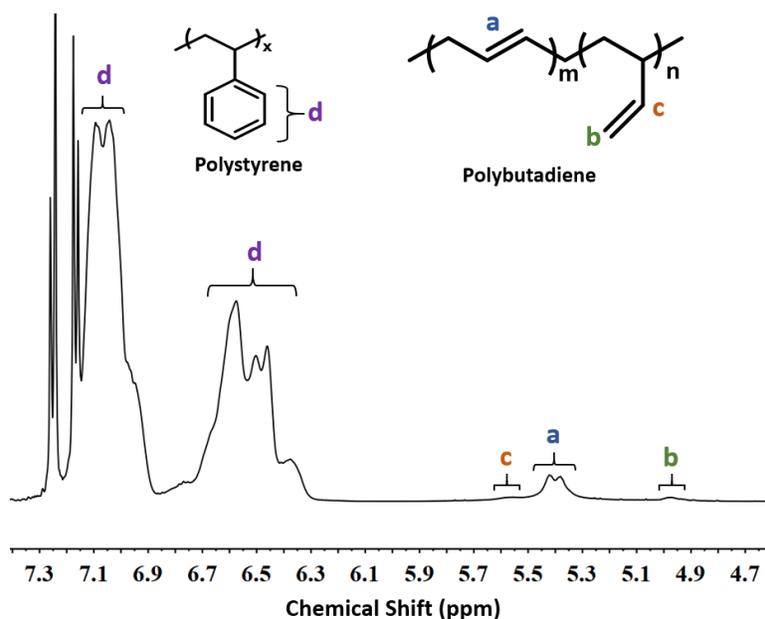
Figure 4.7. ^{1}H-NMR spectrum of high impact polystyrene (HIPS).

The existence of unbroken microcapsules in the self-healing HIPS composites was also evaluated via the presence of EPA fluid in crushed composite specimens containing 7.5 wt.% double walled EPA microcapsules. The crushed specimens were rinsed with CDCl$_3$, and the rinse analyzed by ^{1}H-NMR spectroscopy (Figure 4.8). The ^{1}H-NMR spectrum in Figure 4.8 clearly

shows the presence of EPA through its visible methylene (-CH$_2$-, 3.5 ppm), terminal methylene (-CH$_2$-, 4.25 ppm) and terminal alkyl (-CH$_3$, 1.5 ppm) peaks. This demonstrates the presence of intact EPA-filled microcapsules in the fabricated HIPS composites, verifying the conclusions drawn from the TGA analysis above.
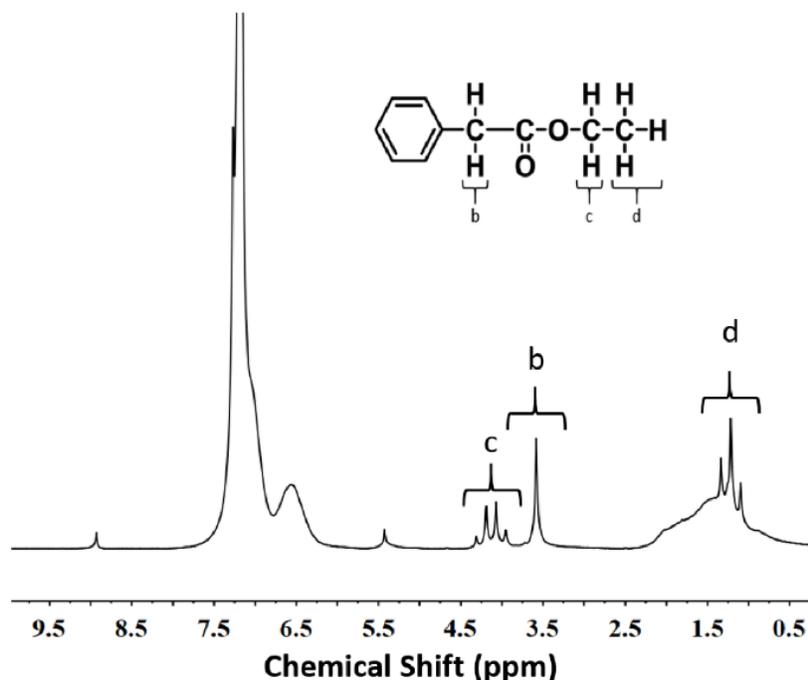
Figure 4.8. ^{1}H-NMR spectrum of EPA extracted from compression molded HIPS composite.

4.3.4. Mechanical Characterization

The impact of microcapsules on composite flexural modulus and flexural strength was examined via three-point bend flexural tests according to ASTM D790 [53]. Slight decreases in both strength and modulus are observed with increasing microcapsule content (Figure 4.9). This result is consistent with the hypothesis that fluid-filled microcapsules act as stress concentrators within the bulk polymer, making the composite more susceptible to material fracture upon loading [61], [62]. The presence of microcapsules can also lead to greater polymer chain mobility decreasing the

modulus [63], [64]. Additionally, analogous decreases in flexural properties have been observed and attributed to agglomeration of microcapsules in the polymer matrix trapping bubbles in the matrix as the viscosity of system increases with microcapsule addition [65], [66].
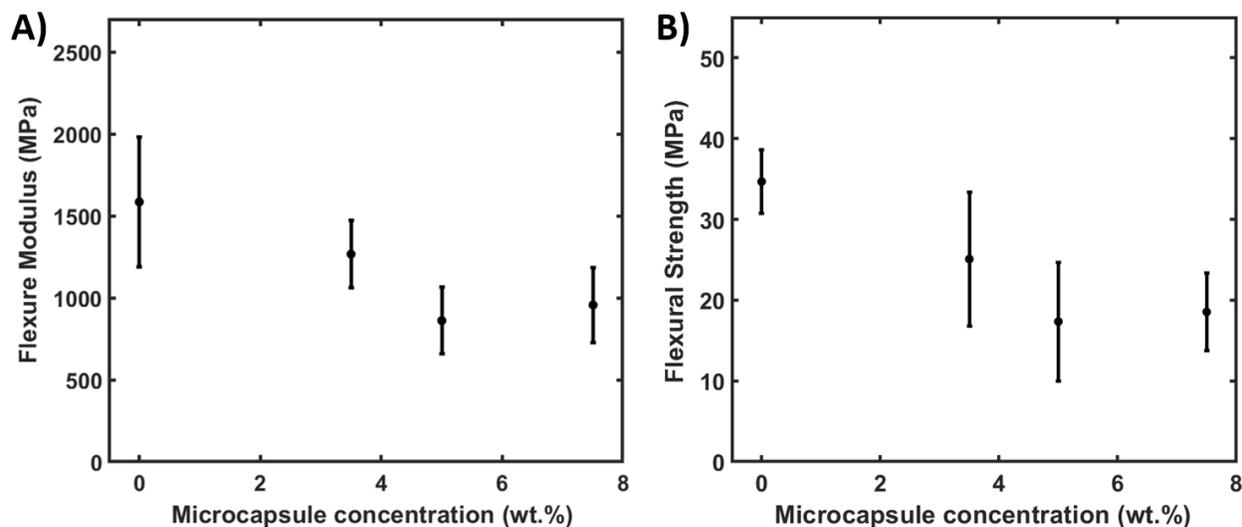
Figure 4.9. A) Flexural modulus and B) flexural strength of HIPS composites with varied microcapsule content. Error bars reflect one standard deviation from four replicates.

The impact of microcapsules on storage modulus (E') and glass transition temperature (Tg) was also probed using DMA and the results are summarized in Table 4.1. In Figure 4.10A, plots of the log(E') of the HIPS composites as a function of temperature show distinct differences as the microcapsule content increases. The incorporation of microcapsules leads to a slight decrease in the storage modulus of the HIPS composites. This can be attributed to an increase in the distance between molecular chains and the network free volume with the addition of microcapsules, leading to a decrease in storage modulus [63], [67]. These results are consistent with the flexural test results. In Figure 4.10B, the tan delta peak estimates the glass transition temperature. Glass transition temperatures of the HIPS composites also decrease with increasing microcapsule

content. Moreover, in Figure 4.10B, only a single transition peak is observed in the tan delta for self-healing HIPS composites, indicating good interfacial adhesion and compatibility between the microcapsules and polymer matrix [68], [69]. Minimal deviations in the storage moduli and glass transition temperatures of the HIPS specimens with and without microcapsules indicate that the addition of microcapsules has only a slight impact on these physical properties of the polymer composite.

Table 4.1. Changes in storage modulus and glass transition temperature of HIPS specimens with increasing microcapsule concentration.

Microcapsule concentration (wt.%)	Storage Modulus (E') (GPa)	Glass Transition Temperature (Tg) (°C)
0	1.92 ± 0.06	113 ± 2
2.5	1.91 ± 0.07	110 ± 1
5.0	1.89 ± 0.05	107 ± 2
7.5	1.88 ± 0.09	102 ± 6
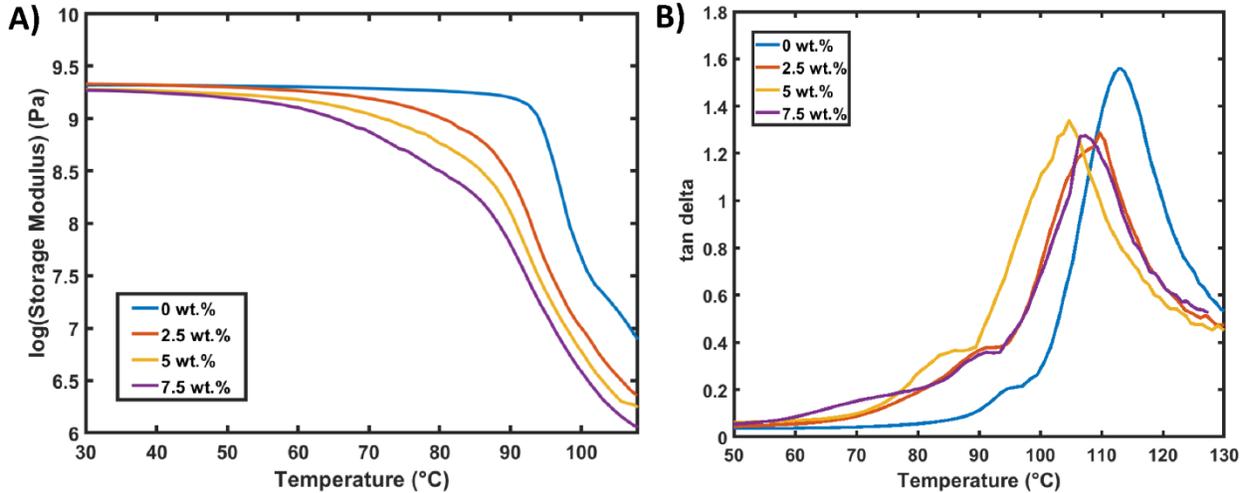
Figure 4.10. Representative DMA plots: A) log storage modulus and B) tan delta of self-healing HIPS composites as functions of temperature.

4.3.5. Characterization of Self-healing

The healing efficiency of specimens with different concentrations of EPA microcapsules was evaluated via the Single Edge Notch Beam (SENB) fracture test. SENB fracture toughness tests provide a standard protocol for monitoring healing efficiency of self-healing composites by monitoring crack growth and fracture toughness before and after a healing event [70], [71]. After initial fracture, the specimens were allowed to heal at room temperature for 24 and 72 hours. These times were chosen to allow sufficient time for fracture toughness recovery and are common temporal benchmarks for self-healing materials [56], [72], [73]. The average fracture toughness of HIPS specimens without microcapsules determined using SENB tests was 3.13 ± 0.47 MPa.m$^{1/2}$. Generally, the inclusion of microcapsules leads to a decrease in fracture toughness of the HIPS composites for all microcapsule contents and this reduced toughness can be attributed to the microcapsules acting as material defects [61].

Chapter 4: Self-healing of High Impact Polystyrene (HIPS) Composites

Using the fracture toughness before and after healing, the healing efficiency is determined for each microcapsule content (Figure 4.11B) for both 24 and 72 hours of healing time. Self-healing is observed for all microcapsule-containing composite specimens with a maximum healing efficiency of 64 % observed after 72 hours for composites with 7.5 wt.% of microcapsules. This observed recovery in fracture toughness is analogous to results demonstrated throughout the self-healing literature where fracture toughness of healing material is shown to increase with microcapsule concentration and healing time [30], [46], [74]-[76]. In particular, these results are comparable to other reports which utilize solvent-based healing systems to impart self-healing behavior to other polymer classes. For instance, up to 89 % recovery of fracture toughness for the thermoplastic polymer poly(methyl methacrylate) has been demonstrated by Celestine et al. using 5 wt.% anisole-containing microcapsules [30]. Caruso et al. utilized 15 wt.% of chlorobenzene-containing microcapsules and observed 78 % recovery of fracture toughness for an epoxy-based thermoset material [74]. Here, the use of EPA as a healing solvent is a less toxic, environmentally friendly alternative to chlorobenzene, or anisole. Previously, EPA was shown to achieve 48 % recovery of fracture toughness for 15 wt.% of microcapsules in an epoxy-based polymer material.[74] The results here are, to our knowledge, the first report of microcapsule-based self-healing of the thermoplastic HIPS and the healing efficiency obtained (up to 64 %) is in line with previous reports using EPA. This demonstrates both the potential and the need for further development to improve both the mechanical behavior of these composites as well as the recovery of fracture toughness after healing.
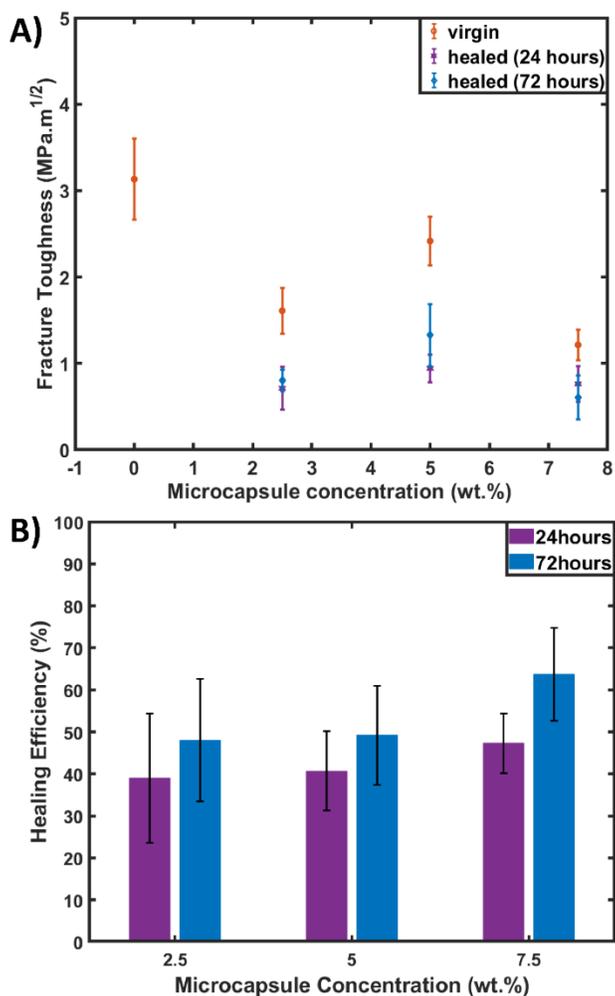
Figure 4.11. A) Fracture toughness before and after healing as a function of microcapsule concentration for 24- and 72-hours healing time. B) Healing efficiency as a function of microcapsule concentration after 24 and 72 hours. Error bars reflect one standard deviation from five replicates.

4.4. Conclusions

This work demonstrates self-healing of a thermoplastic polymer, high impact polystyrene, through the fabrication and evaluation of composites embedded with microcapsules filled with the non-toxic and environmentally friendly solvent EPA. TGA and ^{1}H-NMR spectroscopy analysis

confirm the presence of intact microcapsules in the compression molded HIPS composites. Mechanical characterization via flexural and fracture testing reveals that the addition of microcapsules leads to a decrease in overall mechanical properties with increasing microcapsule content. However, increasing microcapsule content also results in increased healing efficiency, with up to 64% recovery of the fracture toughness achieved at the higher microcapsule loading (7.5 wt.%). This demonstrates the tradeoffs for consideration when translating this approach to target applications. While the general loss in mechanical properties is undesirable, there are still several unexplored tunable system parameters towards minimizing these losses in mechanical properties. As a demonstration of microcapsule-based self-healing for HIPS, our approach of incorporating non-toxic solvent filled microcapsules to incorporate self-healing functionality to readily available and recyclable thermoplastic composites is attractive due to its ease of flexibility and adoption. Overall, this work validates the potential of a microcapsule-based solvent healing approach to self-healing of a common and desirable thermoplastic polymer, HIPS, which has previously not been demonstrated.

4.5. References

[1]   Rajak, D. K.; Pagar, D. D.; Menezes, P. L.; Linul, E. Fiber-Reinforced Polymer Composites: Manufacturing, Properties, and Applications, *Polymers* **2019,** *11*, 1667. https://doi.org/10.3390/polym11101667.

[2]   Sathishkumar, T.; Naveen, J.; Satheeshkumar, S. Hybrid fiber reinforced polymer composites – a review, *J. Reinf. Plast. Comp.* **2014,** *33*, 454–471. https://doi.org/10.1177/0731684413516393.

[3]   Gowda, T. G. Y.; Sanjay, M.R.; Bhat, S.; Madhu, P.; Senthamaraikannan P.; Yogesha, B. Polymer matrix-natural fiber composites: An overview, *Cogent. Eng.*, **2018,** *5*, 1446667. https://doi.org/10.1080/23311916.2018.1446667.

[4]   Clyne, T. W.; Hull, D. *An Introduction to Composite Materials*, **2019.** https://doi.org/10.1017/9781139050586.

[5]   Zagho, M. M.; Hussein, E. A.; Elzatahry, A. A. Recent Overviews in Functional Polymer Composites for Biomedical Applications, *Polymers* **2018,** *10*, 739. https://doi.org/10.3390/polym10070739.

[6]   Singh, S. S.; Chakraborty, P.; Kitey, R. Quasi static compression behavior of glass filled epoxy composites, *Procedia. Struct. Integr.* **2019,** *14*, 915–921. https://doi.org/10.1016/j.prostr.2019.07.071.

[7]   Zafar, M.; Najeeb, S.; Khurshid, Z.; Vazirzadeh, M.; Zohaib, S.; Najeeb, B.; Sefat, F. Potential of Electrospun Nanofibers for Biomedical and Dental Applications, *Materials* **2016,** *9*, 73. https://doi.org/10.3390/ma9020073.

[8]   Qasim, S. B.; Zafar, M. S.; Najeeb, S.; Khurshid, Z.; Shah, A. H.; Husain, S.; Rehman, I. U. Electrospinning of Chitosan-Based Solutions for Tissue Engineering and Regenerative Medicine, *Int. J. Mo. Sci.* **2018,** *19,* 407. https://doi.org/10.3390/ijms19020407.

[9]   Kumar, R.; Ul Haq, M. I.; Raina, A.; Anand, A. Industrial applications of natural fibre-reinforced polymer composites–challenges and opportunities. *Int. J. Sustain. Eng.* **2019**, *12*, 212-220. https://doi.org/10.1080/19397038.2018.1538267.

[10]   Hicks, D. A.; Kirk, A. C.; Stapleton, R. J. Performance of MDI Pour-in-Place Automotive Seating Incorporating Recycled Content, *J. Cell. Plast.* **1996**, *32*, 191–211. https://doi.org/10.1177/0021955x9603200206.

[11] Lebreton, L. C. M.; Van Der Zwet, J.; Damsteeg, J. W.; Slat, B.; Andrady, A.; Reisser, J. River plastic emissions to the world's oceans, *Nat. Commun.* **2017,** *8*, 15611. https://doi.org/10.1038/ncomms15611.

[12] Barnes, D. K. A.; Galgani, F.; Thompson, R. C.; Barlaz, M. Accumulation and fragmentation of plastic debris in global environments, *Philos. Trans. R. Soc. Lond. B. Biol. Sci.* **2009,** *364*, 1985–1998. https://doi.org/10.1098/rstb.2008.0205.

[13] Derraik, J. G. B. The pollution of the marine environment by plastic debris: a review, *Mar. Pollut. Bull.* **2002,** *44*, 842–852. https://doi.org/10.1016/S0025-326X(02)00220-5.

[14] Scaffaro, R.; Maio, A. A green method to prepare nanosilica modified graphene oxide to inhibit nanoparticles re-aggregation during melt processing, *Chem. Eng. J.* **2017,** *308*, 1034–1047. https://doi.org/10.1016/j.cej.2016.09.131.

[15] Scaffaro, R.; Maio, A.; Lopresti, F. Physical properties of green composites based on poly-lactic acid or Mater-Bi® filled with Posidonia Oceanica leaves, *Compos. Part. Appl. Sci. Manuf.* **2018,** *112*, 315–327. https://doi.org/10.1016/j.compositesa.2018.06.024.

[16] Dicker, M. P. M.; Duckworth, P. F.; Baker, A. B.; Francois, G.; Hazzard, M. K.; Weaver, P. M. Green composites: A review of material attributes and complementary applications, *Compos. Part. Appl. Sci. Manuf.* **2014,** *56*, 280–289. https://doi.org/10.1016/j.compositesa.2013.10.014.

[17] da Silva, D. J.; Wiebeck, H. Current options for characterizing, sorting, and recycling polymeric waste. *Prog. Rubber, Plast. Recycl. Technol.* **2020**, *36*, 284-303. https://doi.org/10.1177/1477760620918603.

[18] Martínez-Barrera, G.; Martínez-López, M.; del Coz-Díaz, J. J.; López-Gayarre, F.; Varela-Guerrero, V. Waste Polymers and Gamma Radiation on the Mechanical Improvement of

Polymer Mortars: Experimental and Calculated Results. *Case Stud. Constr. Mater.* **2019**, 11. https://doi.org/10.3390/POLYM12051170.

[19] Okan, M.; Aydin, H. M.; Barsbay, M. Current approaches to waste polymer utilization and minimization: a review. *J. Chem. Technol. Biotechnol.* **2019**, *94*, 8-21. https://doi.org/10.1002/jctb.5778.

[20] Pickering, K. L.; Beg, M. D. H. Management, Recycling and Reuse of Waste Composites, *Mech. Tech. Recycl. Waste. Compos.* **2010,** 303–327.

[21] Grigore, M. E. Methods of Recycling, Properties and Applications of Recycled Thermoplastic Polymers, *Recycl.* **2017,** *2*, 24. https://doi.org/10.3390/recycling2040024.

[22] Yu, K.; Morozov, E. V.; Ashraf, M. A.; Shankar, K. A review of the design and analysis of reinforced thermoplastic pipes for offshore applications, *J. Reinf. Plast. Comp.* **2017**, *36*, 1514–1530. https://doi.org/10.1177/0731684417713666.

[23] Matsuda, A.; Kawahara, S. Applicability of Thermoplastic Elastomers to Impact Load Reduction in Sports Equipment, *Proc.***2020,** *49*, 163. https://doi.org/10.3390/proceedings2020049163.

[24] Oladele, I. O.; Omotosho, T. F.; Adediran, A. A. Polymer-Based Composites: An Indispensable Material for Present and Future Applications, *Int. J. Polym. Sci.* **2020,** 1–12. https://doi.org/10.1155/2020/8834518.

[25] Akca, E.; Gursel, A. A Review on the Matrix Toughness of Thermoplastic Materials, *Period. Eng. Nat. Sci*. **2015,** *3* (2). https://doi.org/10.21533/pen.v3i2.52.

[26] Goettler, L. A. *Mechanical Properties of Reinforced Thermoplastics*, **1986,** 151–204. https://doi.org/10.1007/978-94-009-4193-9_6.

[27] Cheng, L. Zhu, N.; Ni, Z.; Xu, J.; Zhu, X.; Wen, J.; Chen, M. Enhancing the mechanical and thermal properties of waterborne polyurethane composites with thermoset epoxy resin microspheres, *New J. Chem.* **2020,** *44*, 9896–9902. https://doi.org/10.1039/d0nj00143k.

[28] Mazzanti, V.; Malagutti, L.; Santoni, A.; Sbardella, F.; Calzolari, A.; Sarasini, F.; Mollica, F. Correlation between Mechanical Properties and Processing Conditions in Rubber-Toughened Wood Polymer Composites, *Polymers* **2020,** *12*, 1170. https://doi.org/10.3390/POLYM12051170.

[29] Aurilia, M.; Sorrentino, L.; Iannace, S. Improvement of mechanical properties of structural thermoplastic composites using a reactive (low molecular weight) matrix component, *Polym. Compos.* **2010,** *31*, 1762–1769. https://doi.org/10.1002/pc.20967.

[30] Celestine, A.-D. N.; Sottos, N. R.; White, S. R. Autonomic healing of PMMA via microencapsulated solvent, *Polymer* **2015,** *69*, 241–248. https://doi.org/10.1016/j.polymer.2015.03.072.

[31] White, S. R.; Sottos, N. R.; Geubelle, P. H.; Moore, J. S.; Kessler, M. R.; Sriram, S. R.; Brown, E. N.; Viswanathan, S. Autonomic healing of polymer composites*, Nature* **2001,** *409* (6822), 794-797. https://doi.org/10.1038/35057232.

[32] Bond, I.P.; Trask, R.S.; Williams, H.R. Self-healing fiber-reinforced polymer composites, *MRS Bull.* **2008,** *33* (8), 770-774. https://doi.org/10.1557/mrs2008.164.

[33] Trask, R.S.; Williams, H.R.; Bond, I.P. Self-healing polymer composites: mimicking nature to enhance performance*, Bioinspir. Biomim.*, **2007,** *2* (1), 1-9. https://doi.org/10.1088/1748-3182/2/1/P01.

[34] Hager, M. D.; Zechel, S. *Self-Healing Polymer-based Systems* **2020**, 75–94

[35] Blaiszik, B. J.; Kramer, S. L. B.; Olugebefola, S. C.; Moore, J. S.; Sottos, N. R.; White, S. R. Self-Healing Polymers and Composites. *Annu. Rev. Mater. Res.* **2010,** *40*, 179-211. https://doi.org/10.1146/annurev-matsci-070909-104532.

[36] Scheiner, M.; Dickens, T.J.; Okoli, O. Progress towards self-healing polymers for composite structural applications, *Polymer* **2016,** *83*, 260-282. https://doi.org/10.1016/j.polymer.2015.11.008.

[37] Kessler, M.R.; White, S.R. Self-activated healing of delamination damage in woven composites, *Compos. Part. A Appl. Sci. Manuf.* **2001,** *32* (5), 683-699. https://doi.org/10.1016/S1359-835X(00)00149-4.

[38] Kessler, M.R.; Sottos, N.R.; White, S.R. Self-healing structural composite materials, *Compos. Part. A Appl. Sci. Manuf.* **2003,** *34* (8), 743-753. https://doi.org/10.1016/S1359-835X(03)00138-6.

[39] Peterson, A.M.; Palmese, G.R. Reversible Diels–Alder Cycloaddition for the Design of Multifunctional Network Polymers, *Click Chemistry for Biotechnology and Materials Science* **2009,** 195-215. https://doi.org/10.1002/9780470748862.ch9.

[40] Neuser, S.; Michaud, V. Fatigue Response of Solvent-Based Self-Healing Smart Materials, *Exp. Mech.* **2014,** *54* (2), 293-304. https://doi.org/10.1007/s11340-013-9787-5.

[41] Liu, X.; Sheng, X.; Lee, J. K.; Kessler, M. R.; Kim, J. S. Rheokinetic evaluation of self-healing agents polymerized by Grubb's catalyst embedded in various thermosetting systems, *Compos. Sci. Technol.* **2009,** *69* (13), 2102-2107. https://doi.org/10.1016/j.compscitech.2008.08.024.

[42] Urdl, K.; Kandelbauer, A.; Kern, W.; Müller, U.; Thebault, M.; Zikulnig-Rusch, E. Self-healing of densely crosslinked thermoset polymers - a critical review, *Prog. Org. Coat.* **2017,** *104*, 232-249. https://doi.org/10.1016/j.compscitech.2008.08.024.

[43] Gladman, A. S.; Celestine, A.-D. N.; Sottos, N. R.; White, S. R. Self-Healing Materials: Autonomic Healing of Acrylic Bone Cement*, Adv. Healthc. Mater.* **2015,** 4 (2), 170-170. https://doi.org/10.1002/adhm.201570009.

[44] Bekas, D. G.; Tsirka, K.; Baltzis, D.; Paipetis, A. S. Self-healing materials: A review of advances in materials, evaluation, characterization and monitoring techniques*, Compos. B. Eng.* **2016,** *87*, 92-119. https://doi.org/10.1016/j.compositesb.2015.09.057.

[45] Shinde, V. V.; Celestine, A.-D.; Beckingham, L. E.; Beckingham, B. S. Stereolithography 3D Printing of Microcapsule Catalyst-Based Self-Healing Composites, *Acs Appl. Polym. Mater.* **2020,** *2*, 5048–5057. https://doi.org/10.1021/acsapm.0c00872.

[46] Caruso, M. M.; Delafuente, D. A.; Ho, V.; Sottos, N. R.; Moore, J. S.; White, S. R. Solvent-Promoted Self-Healing Epoxy Materials, *Macromolecules*, **2007,** *40*, 8830–8832. https://doi.org/10.1021/ma701992z.

[47] Garcia-Ivars, J.; Wang-Xu, X.; Iborra-Clar, M.-I. Application of post-consumer recycled high-impact polystyrene in the preparation of phase-inversion membranes for low-pressure membrane processes, *Sep. Purif. Technol.*, **2017,** *175*, 340–351. https://doi.org/10.1016/j.seppur.2016.11.061.

[48] Antich, P.; Vázquez, A.; Mondragon, I.; Bernal, C. Mechanical behavior of high impact polystyrene reinforced with short sisal fibers, *Compos. Part. Appl. Sci. Manuf.* **2006,** *37*, 139–150. https://doi.org/10.1016/j.compositesa.2004.12.002.

[49] Bachtiar, D.; Sapuan, S. M.; Khalina, A.; Zainudin, E. S.; Dahlan, K. Z. M. The Flexural, Impact and Thermal Properties of Untreated Short Sugar Palm Fibre Reinforced High Impact Polystyrene (HIPS) Composites, *Polym. Compos.* **2011,** *20*, 493–502. https://doi.org/10.1177/096739111202000510.

[50] Api, A. M.; Belsito, D.; Botelho, D.; Bruze, M.; Burton, G. A.; Buschmann, J.; Dagli, M. L.; Date, M.; Dekant, W.; Deodhar, C.; Francis, M.; Fryer, A. D.; Jones, L.; Joshi, K.; La Cava, S.; Lapczynski, A.; Liebler, D. C.; O'Brien, D.; Patel, A.; Tsang, S. RIFM fragrance ingredient safety assessment, ethyl phenylacetate, CAS Registry Number 101-97-3, *Food Chem. Toxicol.* **2018,** *122*, 192-200. https://doi.org/10.1016/j.fct.2018.08.050.

[51] Trinh, T. ; Bacon, D. R.; Chung, A. H.; Woo, R. A.; Blondin, P. A. US Patent 6001789, **1999.**

[52] Caruso, M. M.; Blaiszik, B. J.; Jin, H.; Schelkopf, S. R.; Stradley, D. S.; Sottos, N. R.; White, S. R.; Moore, J. S. Robust, Double-Walled Microcapsules for Self-Healing Polymeric Materials. *Acs Appl. Mater. Inter.* **2010,** *2*, 1195–1199. https://doi.org/10.1021/am100084k.

[53] ASTM D790: Standard Test Methods for Flexural Properties of Unreinforced and Reinforced Plastics and Electrical Insulating Materials, ASTM International, West Conshohocken, PA, **2017**. https://www.astm.org/d0790-10.html

[54] ASTM D5045: Standard Test Methods for Plane-Strain Fracture Toughness and Strain Energy Release Rate of Plastic Materials, ASTM International, West Conshohocken, PA, **2014.** https://doi.org/10.1520/D5045-14.priate.

[55] Zhu, D.Y.; Rong, M.Z.; Zhang, M.Q. Self-healing polymeric materials based on microencapsulated healing agents: From design to preparation, *Prog. Polym. Sci.* **2015,** *49-50*, 175-220. https://doi.org/10.1016/j.progpolymsci.2015.07.002.

[56] Jiang, S.; Landfester, K.; Crespy, D. Control of the release of functional payloads from redox-responsive nanocapsules, *Rsc Adv.* **2016,** *6*, 104330–104337. https://doi.org/10.1039/c6ra22733c.

[57] Aniskevich, A.; Kulakov, V.; Bulderberga, O.; Knotek, P.; Tedim, J.; Maia, F.; Leisis, V.; Zeleniakiene, D. Experimental characterisation and modelling of mechanical behaviour of microcapsules, *J. Mater. Sci.* **2020,** *55* (27), 13457-13471. https://doi.org/10.1007/s10853-020-04925-8.

[58] Vilaplana, F.; Ribes-Greus, A.; Karlsson, S. Analytical strategies for the quality assessment of recycled high-impact polystyrene: A combination of thermal analysis, vibrational spectroscopy, and chromatography, *Anal. Chim. Acta,* **2007,** *604*, 18–28. https://doi.org/10.1016/j.aca.2007.04.046.

[59] Santee, E.R.; Chang, R.; Morton, M. 300 MHz proton NMR of polybutadiene: Measurement of cis-trans isomeric content. *J. Polym. Sci. Polym. Lett. Ed.* **1973**, *11*, 449-452. https://doi.org/10.1002/pol.1973.130110704.

[60] Carella, J.M.; Graessley, W.W.; Fetters, L.J. Effects of chain microstructure on the viscoelastic properties of linear polymer melts: polybutadiene and hydrogenated polybutadienes, *Macromolecules*, 1984, *17*, 2775-2786. https://doi.org/10.1021/ma00142a059.

[61] Albdiry, M.; Yousif, B. Toughening of brittle polyester with functionalized halloysite nanocomposites, *Compos. B. Eng.,* **2019,** *160*, 94-109. https://doi.org/10.1016/j.compositesb.2018.10.032.

[62] Yang, C.; Huh, H.; Hahn, H. Investigation of effective material properties in composites with internal defect or reinforcement particles*, Int. J. Solids Struct.,* **2005,** *42* (24-25), 6141-6165. https://doi.org/10.1016/j.ijsolstr.2005.06.094.

[63] Guadagno, L.; Raimondo, M.; Vietri, U.; Naddeo, C.; Stojanovic, A.; Sorrentino, A.; Binder, W. H. Evaluation of the Mechanical Properties of Microcapsule-Based Self-Healing Composites, *Int. J. Aerosp. Eng.,* **2016,** 1–10. https://doi.org/10.1155/2016/7817962.

[64] Jud, K.; Kausch, H. H. Load transfer through chain molecules after interpenetration at interfaces, *Polym. Bull.*, **1979,** *1*, 697–707. https://doi.org/10.1007/BF00255445.

[65] Bolimowski, P. A.; Bond, I. P.; Wass, D. F. Robust synthesis of epoxy resin-filled microcapsules for application to self-healing materials, *Philos. Trans. A Math. Phys. Eng. Sci.*, **2016,** *374*, 20150083. https://doi.org/10.1098/rsta.2015.0083.

[66] Ebrahimnezhad-Khaljiri, H.; Eslami-Farsani, R. Experimental investigation of flexural properties of glass fiber–epoxy self-healable composite structures containing capsulated epoxy healing agent and NiCl 2 (imidazole) 4 catalyst, *J. Ind. Text,* **2019,** 152808371989292. https://doi.org/10.1177/1528083719892923.

[67] Katoueizadeh, E.; Zebarjad, S. M.; Janghorban, K. Mechanical properties of epoxy composites embedded with functionalized urea-formaldehyde microcapsules containing an oxidizable oil, *Mater. Chem. Phys.* **2021,** *260*, 124106. https://doi.org/10.1016/j.matchemphys.2020.124106.

[68] L. E. Nielsen; R. F. Landel, *Mechanical Properties of Polymers and Composites*, Marcel Dekker, New York, NY, USA, 2nd edition, **1994.**

[69] Ogunsona, E. O.; Misra, M.; Mohanty, A. K. Impact of interfacial adhesion on the microstructure and property variations of biocarbons reinforced nylon 6 biocomposites. *Compos. Part. Appl. Sci. Manuf.* **2017,** *98*, 32–44. https://doi.org/10.1016/j.compositesa.2017.03.011.

[70] Patrick, J.; Sottos, N.; White, S. Microvascular based self-healing polymeric foam, *Polymer,* **2012,** 53(19), 4231-4240. https://doi.org/10.1016/j.polymer.2012.07.021

[71] Crespy, D.; Landfester, K.; Fickert, J.; Rohwerder, M. *Adv. Polym. Sci.* **2016,** *273*, 247-283.

[72] Fischer, H.; Waindich, A.; Telle, R. Influence of preparation of ceramic SEVNB specimens on fracture toughness testing results, *Dent. Mater.* **2008,** *24*, 618–622. https://doi.org/10.1016/j.dental.2007.06.021.

[73] Wu, J.; Weir, M. D.; Melo, M. A. S.; Xu, H. H. K. Development of novel self-healing and antibacterial dental composite containing calcium phosphate nanoparticles, *J. Dent.*, **2015,** 43, 317–326. https://doi.org/10.1016/j.jdent.2015.01.009.

[74] Caruso, M. M.; Blaiszik, B. J.; White, S. R.; Sottos, N. R.; Moore, J. S. Full Recovery of Fracture Toughness Using a Nontoxic Solvent-Based Self-Healing System, *Adv. Funct. Mater.* **2008,** *18*, 1898–1904. https://doi.org/10.1002/adfm.200800300.

[75] Wool, R. P.; O'Connor, K. M. Time dependence of crack healing, *J. Polym. Sci Polym. Lett. Ed.* **1982,** *20,* 7–16. https://doi.org/10.1002/pol.1982.130200102.

[76] Jud, K.; Kausch, H. H.; Williams, J. G. Fracture mechanics studies of crack healing and welding of polymers, *J. Mater. Sci.* **1981,** *16*, 204–210. https://doi.org/10.1007/BF00552073.

Chapter 5

Fused Filament Fabrication of Self-healing Polymer Composites

5.1. Introduction

3D printing is an advanced technology for fabrication of three dimensional physical objects from 3D CAD designs [1], [2]. Owing to its key advantages including customization of complex and unique designs and operational simplicity as compared to traditional methods, 3D printing finds application in diverse industrial sectors including aerospace, robotics, electronics, automobile, medical, construction, and design [3]–[5]. There is a large variety of 3D printing techniques, as categorized by ASTM International F42, including fused filament fabrication (FFF) which is a class of material extrusion that is the most common and broadly accessible technology due to its affordable costs, with reduced cycle time and user-friendly approach [6], [7]. FFF constructs an object from thin layers of extruded filaments of a semi-melted thermoplastic from 3D CAD models [7], [8]. Currently, FFF is increasingly used for fabricating prototypes and functional spare parts

using polymer materials at the design stage due to its ease of design, short fabrication timelines, and ability to fabricate lighter parts with low cost and high functionality [6], [7].

While great strides are being made, the relatively poor mechanical strength and weak interlayer adhesion between successive layers of FFF printed components can lead to inaccessible damage within the polymer matrix which can lead to higher material failure rates [9]–[11]. Moreover, application of FFF 3D printing is limited by relatively poor surface roughness and accuracy of 3D printed parts [12]–[14]. There are numerous factors responsible for the ultimate mechanical properties, and thereby use-cases and useful lifetimes, of 3D printed components including layer thickness, orientation of filaments during 3D printing, air gaps between layers, and process of filament solidification during extrusion for which ongoing research has sought to optimize the mechanical properties of FFF printed specimens [15], [16]. For instance, the use of reinforcement fillers like carbon nanofibers have enhanced mechanical strength of FFF printed components, although there are remaining challenges including fiber orientation in the polymer matrix, fiber-matrix debonding, and void formation [17], [18]. Another approach to improve 3D printed component lifetimes and reliability is to use a material system which autonomously heals itself, i.e. self-healing [19]–[21].

Self-healing is a phenomenon where material damage caused by external force is repaired through a healing process that restores the material's mechanical properties [22], [23]. Self-healing material systems are generally categorized as capsule-based, vascular-based, or intrinsic self-healing [20], [24], [25]. Intrinsic self-healing materials possess latent functionality within the matrix, that heals fractures in the system triggered by material damage or an external stimuli such as heat, UV light or external force [26]–[29]. Intrinsic self-healing is typically based on molecular level chemical reactions such as hydrogen bonding or reversible polymerization [30]. Application

of intrinsic self-healing materials is limited as it generally requires external stimuli such as heat or UV light to initiate the self-healing process [24] and requires the use of functional (and many times expensive) materials as the matrix which inherently sets the material properties of the system limiting broad use across a range of applications. Microcapsule and microvascular-based autonomous self-healing materials are both extrinsic self-healing approaches, where microcracks in polymer matrices are healed through encapsulated healing agent in the form of either capsules or vascular networks either by polymerization, or entanglement processes [19], [31]–[35]. For instance, White et.al. investigated the performance of healing fluid filled vascular networks to recover mechanical properties in response to large scale damage in polymer systems.[36] Fabrication and integration of vascular networks in 3D printed polymer composites, while feasible, is challenging due to network complexity and chances of creating blockage and large volume void formation after the healing event [35]. However, microcapsule based self-healing systems are highly localized and can recover the fracture damage where it is initiated. For instance, White and group reported self-repairing in epoxy based polymer composites containing dicyclopentadiene (DCPD) monomer filled microcapsules [21]. Another approach is solvent-based self-healing, also microcapsule-based, where microcracks in the polymer matrix rupture the microcapsules and release solvent to the crack site, promoting chain mobility by locally solubilizing polymer chains, and ultimately interlocking cracked surfaces upon solvent diffusion or evaporation away from the crack site [37], [38]. Solvent based self-healing is efficient for thermoplastic polymers as polymer chains mobility in the presence of solvent is feasible (in contrast to thermosets). This is a facile and economical approach without the addition of crosslinker or external catalyst for fracture recovery [37]–[39].

Chapter 5: Fused Filament Fabrication of Self-healing Polymer Composites

Several studies have investigated 3D printing of intrinsic self-healing polymer systems such as hydrogen bonding, ionic interactions, and Diels Alder reactions using stereolithography or direct ink writing 3D printing to fabricate self-healing elastomeric or hydrogel structures [40]–[43]. The 3D printing of thermoset microcapsule-based self-healing polymer composites via stereolithography has also been reported, where monomer-filled microcapsules enable self-healing to restore the polymer mechanical properties with the help of a catalyst by forming a crosslinked network over the fracture site [19], [44]. Here, we demonstrate that microcracks formed in FFF 3D printed thermoplastic high impact polystyrene composites can be autonomically repaired by a non-toxic and "green" organic solvent, ethyl phenylacetate (EPA), restoring mechanical properties after a fracture event. To the extent of our knowledge, FFF 3D printing of an extrinsic, microcapsule based self-healing polymer system has not been previously reported.

We investigate the FFF printing of a self-healing thermoplastic composite system with high impact polystyrene (HIPS), a polymer with high toughness, embedded with non-toxic ethyl phenylacetate (EPA) solvent-filled microcapsules. HIPS is a commonly used and recyclable thermoplastic polymer for 3D printing with high impact strength, easy printability and low cost [45]–[47]. Ethyl phenylacetate (EPA), a low toxicity and non-mutagenic small molecule found in beer, wine and citrus fruits, is used as the healing fluid as it has a high boiling point (229 °C), which is important for enabling the microcapsules to survive the FFF printing process, and a solubility parameter (δ_{EPA} = 5.3 MPa$^{1/2}$) close to that of HIPS (δ_{HIPS} = 5.8 MPa$^{1/2}$) facilitating solvation and ultimately healing [48], [49]. The use of a sustainable healing fluid (EPA) and a recyclable thermoplastic polymer (HIPS) to design and fabricate self-healing polymer composites aims to contribute to a more environmental friendly society, reducing plastic pollution, energy use and cost [50]–[54].

Chapter 5: Fused Filament Fabrication of Self-healing Polymer Composites

EPA-filled microcapsules are prepared, coated onto the surface of commercially available HIPS filament, and used to prepare FFF 3D printed self-healing composites. The survivability of microcapsules after FFF printing is confirmed using low-field ^{1}H-NMR spectroscopy and thermogravimetric analysis (TGA). Microcapsule response to an induced microcrack is demonstrated by scanning electron microscopy (SEM). Mechanical properties of the FFF 3D printed composites containing microcapsules are examined using dynamic mechanical analysis (DMA) and self-healing behavior is examined via fracture testing performed using the single edge notch bend (SENB) test. Overall, these FFF 3D printed self-healing composites show solvent-based autonomous self-healing of up to 81% fracture recovery illustrating their potential for extending the lifetime of FFF 3D printed composites.

5.2. Materials and Methods

5.2.1. Materials

HIPS polymer pellets and filaments of diameter 1.75 mm were from 3DXtech. Polyurethane (PU) prepolymer (Desmodur L 75, in ethyl acetate solvent, equivalent weight = 315 g, isocyanate content = (13.3 ± 0.4) wt.%.) was graciously provided by Covestro. Ethylene-maleic anhydride (EMA) copolymer (Zemac-400, Polyscience, Inc.) was used as a 2.5 wt.% aqueous solution. Dichloromethane (DCM), $CHCl_3$, urea, ammonium chloride, NaOH pellets, and tetrahydrofuran (THF) were obtained from BDH chemicals. HCl (95%, Merck Chemicals), EPA (Sigma-Aldrich), 1-Octanol (Fischer Chemicals), Formaldehyde solution (formalin, 37 w/v %, BTC Chemicals) and $CDCl_3$ (EMD Millipore). All DI water used in this investigation was Type-1 deionized water (DI water) produced by a Waterpro BT Purification System from Labconco® (Kansas City, MO).

5.2.2. Synthesis of PU-UF double-walled microcapsules with EPA core fluid

Self-healing double-walled EPA-filled microcapsules were fabricated following the general procedure of Caruso et al. [31] with slight modifications to synthesize polyurethane/poly-(urea-formaldehyde) (PU-UF) microcapsules in a single batch process via an in-situ interfacial oil-in-water (O/W) emulsion polymerization process as described in Shinde et al. [19] which is reproduced from Reference 19 (Chapter 3 in the dissertation, section 3.2.2). The only change in the synthesis process here is the use of EPA as the core fluid in the organic phase; synthesis process explained in Figure 5.1. Sieved double-walled PU-UF EPA microcapsules with an average diameter of 126 μm ± 20 μm were utilized in this work (collected on the 106 μm sieve tray).
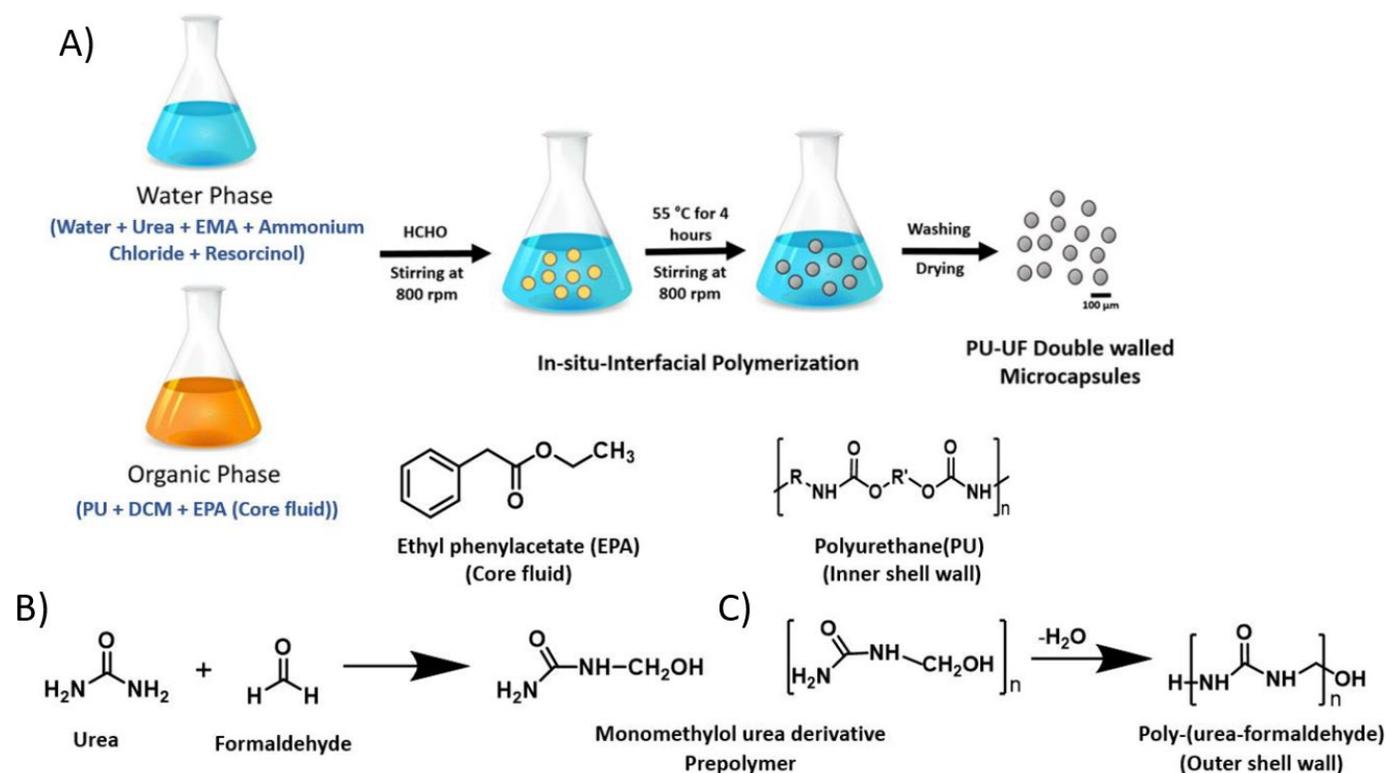
Figure 5.1. Schematic illustration of the in-situ interfacial emulsion polymerization process and chemistry.

5.2.3. Characterization of neat microcapsules

Microcapsule average diameter, presence of healing fluid and microcapsule size distribution of the synthesized batch (150 measurements from 5 different aliquots) and the sieved batch (200 measurements from 4 different aliquots) were evaluated by optical microscopy via an Olympus 52 ×7 microscope at varied magnifications with the use of Cellsens and ImageJ software. The surface images of microcapsules were acquired using a Zeiss EVO50 microscope based Au sputter coated samples. TGA was performed (TA Instruments Q500) to examine thermal stability and operational temperature of microcapsules for the FFF process. The stability of the microcapsules in chemical environments was investigated by visualizing microcapsule morphologies under an optical microscope after soaking in deionized water, pH 4 and pH 10 buffer solution, THF, and chloroform. After 2 days, a small fraction of microcapsule dispersed solution was placed on a glass slide and viewed under microscope. In the case of water and pH solutions, microscopic images showed microcapsules scattered in aqueous media and for organic solvents, it showed dried microcapsules.

5.2.4. FFF 3D printing of self-healing HIPS composites

5.2.4.1. *Preparation of microcapsule coated HIPS filaments*

HIPS pellets (7 g) were dissolved in THF (100 mL) solvent. Once dissolved, double walled EPA microcapsules (7.5 wt. %), were added and the formulation was stirred for 25-30 minutes at 40-45 °C. 7.5 wt. % microcapsules were added into the polymer solution to ensure availability of sufficient concentration of microcapsules coated on polymer filaments for self-healing of microcracks in FFF printed polymer composites. The polymer ink is polymer-microcapsule solution, formulated for microcapsules coating on the 3D printing HIPS filaments. Initially, polymer filaments of 1.75 mm ± 0.05 mm diameter were passed through a manual hand drawn

coater analogous to that utilized by Green et al. (shown in Figure 5.2) [55]. However, to achieve uniform coatings for 3D printing, polymer filaments of 1.75 mm ± 0.05 mm diameter were passed through the microcapsule formulations using a custom-built continuous bath coater (Figure 5.2). Coated polymer filaments were then dried in a vacuum oven at room temperature (24 °C) for at least 1 hour prior to their use for FFF 3D printing. Filament diameter slightly increases upon coating to 1.83 mm ± 0.15 mm, though this is still within the printability specifications of the FFF printer. TGA of microcapsule coated filaments was performed at a heat rate 10 ºC/min from 25 to 500 ºC under nitrogen flow.
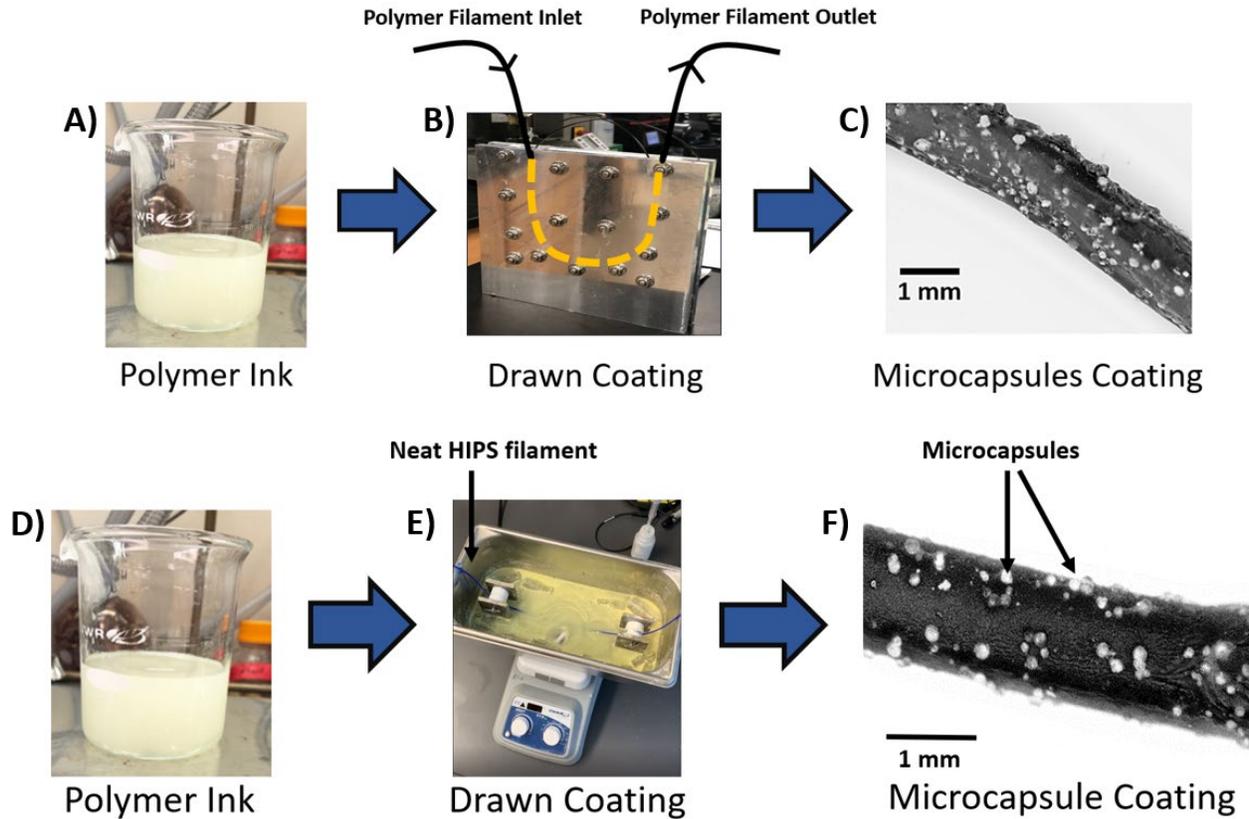
Figure 5.2. HIPS filament coating process. The photographs of A) polymer ink formulation (polymer-microcapsules solution) and, B) Drawn coater (a manual hand drawn coater) illustrating coating of microcapsules on the filament, C) Optical microscopic image of the microcapsules coated HIPS filament; D) polymer ink formulation (polymer-microcapsules solution) and, E) Drawn coater (a continuous bath coater) illustrating coating of microcapsules on the filament, F) Optical microscopic image of the microcapsules coated HIPS filament.

5.2.4.2. 3D printing of microcapsules coated filaments

A spool of microcapsule-coated thermoplastic filaments was mounted onto the FFF Monoprice Maker Select Plus (IIIP) 3D Printer and a STL file of a required 3D structure loaded into the CURA software, provided by Monoprice, to generate a gcode file. A layer thickness of 100 micron was

chosen. When the 3D printer nozzle arrived at the extrusion temperature (extrusion temperature for HIPS is 205 °C), the filament was fed to the extrusion head and in the nozzle where it melted. The extrusion head was appended to a 3-axes framework that enables it to move in all 3 directions, the X, Y and Z directions. The softened material was expelled in thin polymer layers and deposited layer-by-layer on the build plate, where it cooled and set. The cooling of the material was quickened using cooling fans connected on the extrusion head. The Table 5.1 represents 3D printing parameters for fabrication of self-healing HIPS composites. Rectangular self-healing composite specimens with measurements 52.8 mm × 12 mm × 6 mm were fabricated via FFF for mechanical characterization, fracture tests, SEM imaging, and evaluation of microcapsule survivability after 3D printing. Figure 5.3 represents 3D printed HIPS rectangular specimen images.
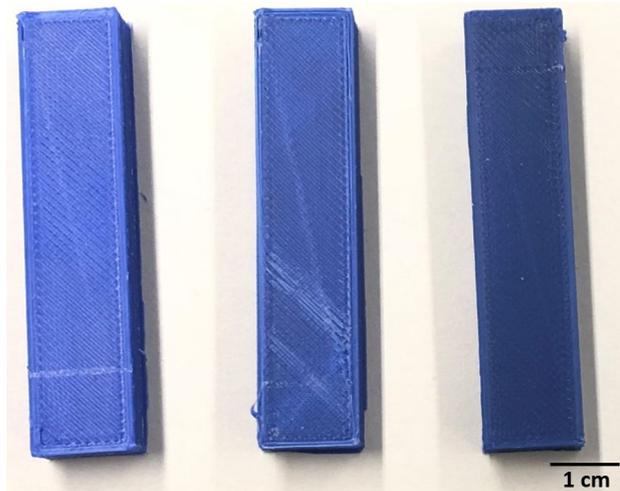
Figure 5.3. 3D printed rectangular specimen (52.8 mm × 12 mm × 6 mm) containing 7.5 wt.% microcapsules.

Table 5.1. 3D Printing parameters for 3D printing of HIPS composites

Printing parameter	Values
Build pattern	Alternating
Print Speed	65 mm/s
Print temperature	205 °C
Bed temperature	105 °C
Infill Density	100 %
Print direction	XY

5.2.5. Characterization of FFF 3D printed self-healing composites

5.2.5.1. *Thermogravimetric Analysis (TGA)*

TGA of microcapsule coated filaments and FFF printed HIPS composite specimens was performed on a TA instruments Q500 at a rate 10 ºC/min from 25 to 600 ºC under nitrogen flow.

5.2.5.2. *^{1}H-NMR Spectroscopy*

Microcapsules survivability after FFF printing was evaluated by ^{1}H-NMR spectroscopy through the release of encapsulated fluid (EPA) after mechanically crushing the specimens. The crushed composite containing 7.5 wt.% microcapsules was rinsed with chloroform. The rinse was filtered using Whatman filter paper to remove undissolved fragments and filtrate was added to an NMR tube and the NMR spectra collected using a PULSAR 60 MHz NMR spectrometer from Oxford Instruments.

5.2.5.3. Scanning Electron Microscopy (SEM)

SEM was performed to visualize healing of microcracks in the FFF printed self-healing composites containing 7.5 wt.% EPA filled microcapsules using a Zeiss EVO50 SEM. Microcrack-healing performance and healing effect of the microcapsules were monitored and evaluated by microfracture repair within 72 hours of healing time.

5.2.5.4. Mechanical Characterization

5.2.5.4.1. Dynamic Mechanical Analysis (DMA)

Thermomechanical properties of 3D printed composites were characterized by DMA (TA instruments RSA III DMA) and fracture testing was carried out using a screw-driven Instron mechanical test frame (Model 5565, 1kN load cell). Room temperature storage modulus (E′) glass-transition temperature (Tg, obtained as the peak value in tan delta curve) were determined using a dynamic temperature ramp test with heat rate of 5 °C/min and a frequency of 1 Hz.

5.2.5.4.2. Fracture Toughness Single Edge Notch Beam Test

The performance of microcapsules to recover fracture toughness, K_Q, in FFF 3D printed self-healing HIPS composites was evaluated using the single-edge notched bend (SENB) fracture test as per ASTM D5045 [56]. FFF printed specimens (52.8 mm x 12 mm x 6 mm) with 7.5 wt.% of microcapsules were first pre-notched using a diamond tipped saw blade, process described in Ref. 37) [37]. The fracture toughness test is described in Shinde et al. [37] (reproduced in its entirety from Reference 37; chapter 4 in the dissertation, section 4.2.7-*Fracture testing*). The crack length to width (*a/W*) ratio was kept between 0.45 and 0.55 as per the ASTM protocol [56]. In this work, the initial microcrack length including pre-notch and pre-crack length in each specimen was approximately 6 mm, corresponding to *a/W* = 0.5. Displacement controlled SENB tests were

performed via Instron at a strain rate of 5 mm/min with fracture toughness (K_Q, MPa.m$^{1/2}$) determined as

$$K_Q = \left(\frac{P_Q}{BW^{\frac{1}{2}}}\right) f(x) \tag{1}$$

$$f(x) = 6x^{1/2} \frac{[1.99 - x(1-x)(2.15 - 3.93 + 2.7x^2)]}{(1+2x)(1-x)^{3/2}} \tag{2}$$

where P_Q is the fracture load (kN), B and W are the specimen thickness and width (cm) respectively, and x is the crack to width ratio (a/W). Healing efficiency, η, was investigated by allowing the fractured specimens to heal undisturbed for 24 and 72 hours at room temperature followed by a second fracture test and calculated as the ratio of healed fracture toughness (K_Q^{healed}) to virgin (initial) fracture toughness (K_Q^{virgin}); Equation 3. Four replicates were studied for each specimen and the average and standard deviation reported.

$$\eta \ (\%) = \left\{ \frac{(K_{QIc}^{healed})}{(K_{QIc}^{virgin})} \times 100 \right\} (\%) \tag{3}$$

5.3. Results and Discussion

5.3.1. Microcapsule Characterization

Double shell walled microcapsules are targeted for their better mechanical strength as compared to single walled microcapsules. This is primarily due to their thicker shell walls (as previously reported by Caruso *et. al.,* average shell wall thickness typically around (530 ± 30) nm for double shell-walled PU-UF microcapsules compared to (175 ± 33) nm for single shell-walled PUF microcapsules), which are critical for long term shelf life of the microcapsules and microcapsule survivability at elevated temperatures and pressures such as those present in fused filament fabrication (FFF) of polymer composites [31], [57]. Here, double shell walled microcapsules

encapsulating ethyl phenylacetate (EPA) with polyurethane as the inner shell wall and poly(urea-formaldehyde) as the outer shell wall were fabricated using an interfacial polymerization process adopted from Caruso et. al. [31]. An in-situ interfacial polymerization process ensures successful synthesis of microcapsules and their integration within polymer matrices for FFF 3D printing, as it allows isolation of core fluid, good interfacial adhesion with polymer matrices due to a rough microcapsule outer surface and better mechanical interlocking of microcapsules with polymer surfaces, along with fast release of curing agent from microcapsules during damage event due to capillary action and low viscosity of core fluid [19], [21], [37], [58], [59]. First, the polyurethane shell wall is formed encapsulating the core fluid, EPA. Meanwhile, urea reacts with formaldehyde in two stages; first under alkaline conditions, it forms urea-formaldehyde prepolymer derivative, and in the second step, the urea-formaldehyde derivative under polycondensation reaction, forms poly(urea-formaldehyde) (See Figure 5.1) [60]. As the molecular weight of the formed poly(urea-formaldehyde) increases, it deposits onto the polyurethane shell wall, forming the outer shell wall.

As-synthesized microcapsules are visualized under an optical microscope and shown in Figure 5.4A, B. The successful encapsulation of core fluid after microcapsule synthesis was verified by mechanically crushing the microcapsules and confirming the release of core fluid under the microscope as demonstrated in Figure 5.4B. The surface morphology of microcapsules was also examined using SEM which confirmed spherical microcapsules were obtained, see Figure 5.4C, D. From the SEM images in Figure 5.4D, the outside surface of the EPA-filled microcapsules appears rough, which helps improve surface adhesion between the microcapsules and polymer matrix in the 3D printed specimens, promoting the release of healing fluid upon microcracking and stimulating faster recovery of fracture [61]. The rougher exterior surface of microcapsules is due to accumulation of excess urea-formaldehyde (UF) on the exterior wall [60]. It is also clear

from both the optical images in Figure 5.4A and the SEM image in Figure 5.4C that microcapsules with a wide range of sizes are produced. A non-uniform size distribution can occur due to differences in flow characteristics of the emulsion as the emulsified solution flows rapidly around the propeller in the agitation process. Consequently, the microcapsules further away from the propeller have larger diameters, while the microcapsules closer to the propeller are smaller.[61] Therefore, investigation of microcapsule size distribution is important to evaluate the microcapsule size range and to isolate the target size for 3D printing.
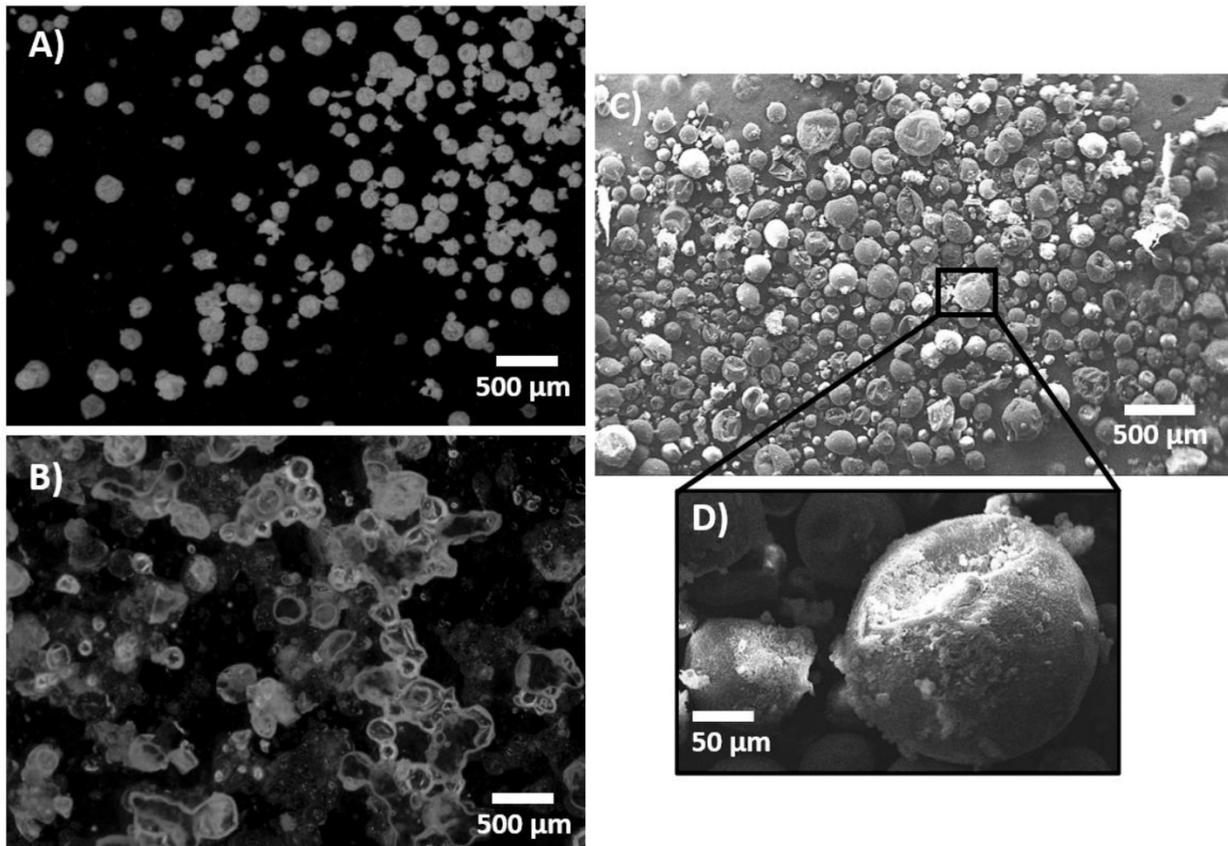
Figure 5.4. Visualization of microcapsules (A) optical microscopy image displaying intact microcapsules, (B) microcapsules crushed under a cover slip showing release of core fluid, EPA, (C) SEM image of microcapsules showing spherical particles of different sizes, and (D) SEM image of a single microcapsule.

Microcapsule particle size distribution of the sieved microcapsules (see Figure 5.5) was evaluated by measuring microcapsule diameters from optical micrographs (see Figure 5.5A). Here, the diameters of 200 randomly selected microcapsules from 5 different aliquots were measured from optical microscopic images and a size distribution constructed. The sieved microcapsules (collected on a 106 µm sieve tray) size distribution is shown in Figure 5.5B. These microcapsules have an average diameter of 126 µm ± 20 µm and were used for the entire work in this study.
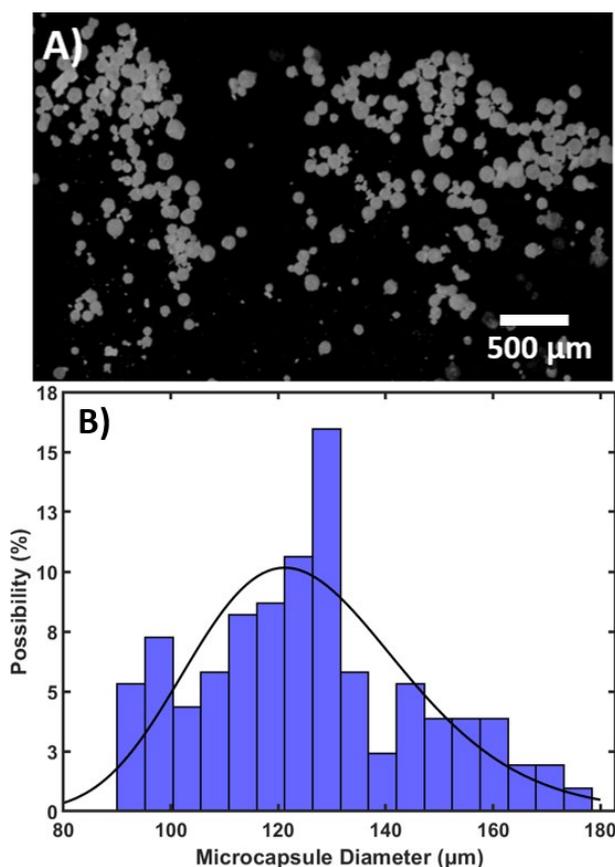
Figure 5.5. Optical microscopic image of A) sieved microcapsules, and particle size distribution of (B) sieved batch of microcapsules (average diameter: 126 µm ± 20 µm) where solid black lines denote normal distribution for sieved batch.

5.3.2. Microcapsule thermal stability

Microcapsule thermal stability was investigated by TGA; Figure 5.6. The microcapsules are thermally stable up to around 210 °C, after which there is a decrease in sample mass with 5 wt.% loss obtained at 225 °C and 95 wt.% mass loss observed at 271 °C. The precipitous drop in weight at approximately 225 °C corresponds to microcapsule rupture and loss of EPA core fluid as vapor near EPA's normal boiling temperature (229 °C). The volatilization of the encapsulated solvent EPA leads to rapid expansion, loss of microcapsule mechanical integrity, and corresponding weight loss of EPA. As encapsulated solvent is the major component of the microcapsules by mass, the observed weight loss near its boiling point also verifies successful encapsulation of EPA.
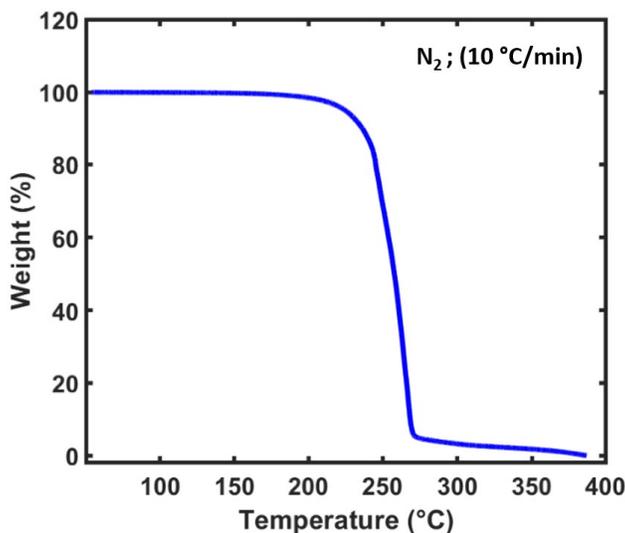
Figure 5.6. Thermogravimetric (TGA) curve of EPA-filled microcapsules.

5.3.3. Microcapsule chemical stability

Microcapsule stability in solvents is evaluated for aqueous solutions of varied pH and a series of organic solvents as exposure to solvents can degrade the microcapsule shell walls during microcapsule solution preparation for coating microcapsules onto surfaces or, the focus here,

polymer filaments. Moreover, it is important to study the chemical stability of microcapsules to understand microcapsule storage stability which is directly related to the surrounding chemical environment (temperature, humidity, pH, etc.) and stability of the core fluid with the encapsulating matrix or shell material [62]. For instance, Sun. et al. noted that the thermosetting shell walls of double-layered polyurea microcapsules swell through imbibition after immersion in organic solvents including acetone, hexane, xylene, and dimethyl sulfoxide (DMSO), which can cause a change in microcapsule morphology [63]. Here, 1 wt.% of microcapsules were immersed in DI water, pH 4 and pH 10 water, chloroform, acetone, and tetrahydrofuran (THF). Optical microscopic images were taken after soaking in these solutions for 48 hours (shown in Figure 5.7). No deflation or breaking of microcapsules was observed in water, acidic, and basic solutions (Figure 5.7A-C). Moreover, the formation of agglomerations was not observed, and microcapsules remained segregated in these aqueous solutions. Similarly, in the organic solvents chloroform and THF, microcapsules retained their shape, observed from microscopic images (Figure 5.7D, E). However, in the case of acetone, the microcapsules showed some deflation (Figure 5.7F), suggesting that this solvent should be avoided for microcapsule processing or processing of 3D printed specimens containing these microcapsules; an observation consistent with the findings of Sun et al. [63].
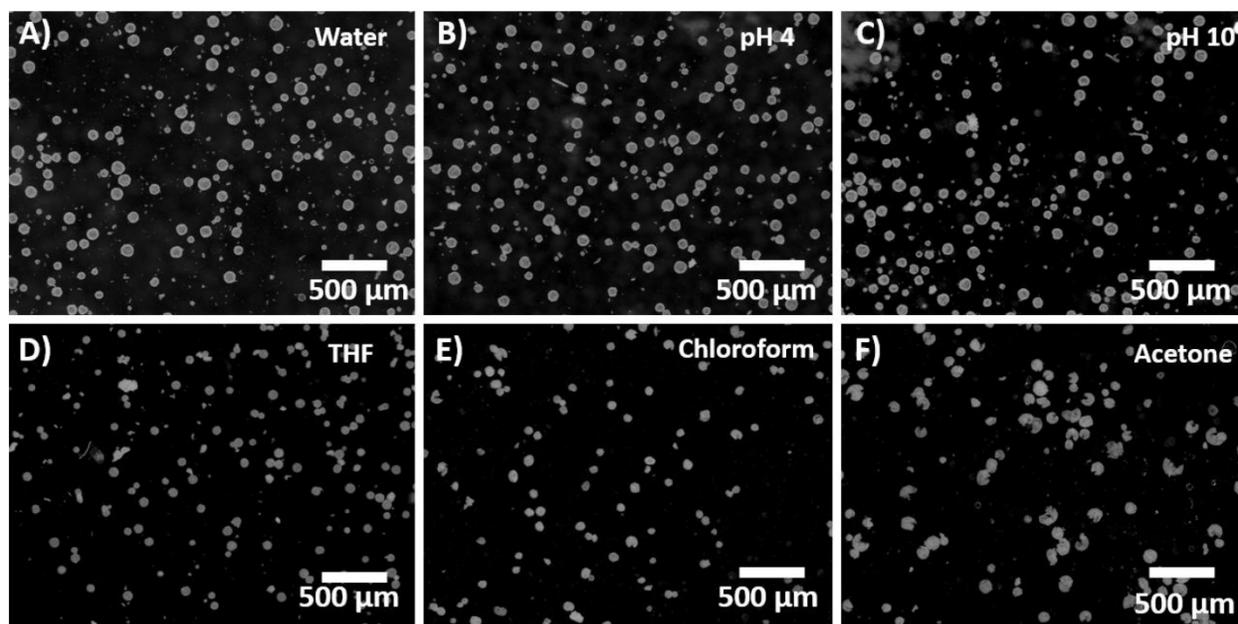
Figure 5.7. Optical microscope images of microcapsules after incubation in (A) water, (B) pH 4 water, (C) pH 10 water, (D) THF, (E) chloroform, and (F) acetone.

5.3.4. Microcapsule survivability after coating and 3D printing process

TGA was performed on microcapsules-coated HIPS filaments to confirm the presence of intact microcapsules. Here, we focus on the initial 10 wt.% mass loss up to 350 °C; Figure 5.8B, however full thermogram is shown in Figure 5.8A. The thermograms in Figure 5.8B show the virgin HIPS filament (without microcapsules- 0 wt.%) is stable, and no substantial weight loss (less than 1 wt.% mass loss) is observed until above 300 °C. Meanwhile, microcapsule-coated filament with 2 wt.% microcapsules exhibit mass loss starting between 170 and 190 °C and approximately 1.9 wt.% loss up to 270 °C. This corresponds to the loss of EPA core fluid through boiling, vaporization, and microcapsule rupture, and EPA fluid release, as it primarily occurs near EPA's boiling temperature (~ 229 °C), (see section 3.2 above, Figure 5.6) [37]. Similar behavior is observed for the microcapsule-coated filaments with 2.5 wt.% and 7.5 wt.% microcapsules; with

2.5 wt.%, and 6.6 wt.% mass loss at around 270 °C, respectively. Overall, the mass loss observed

in these filament specimens roughly tracks their relative microcapsule concentration and thereby

their EPA content.
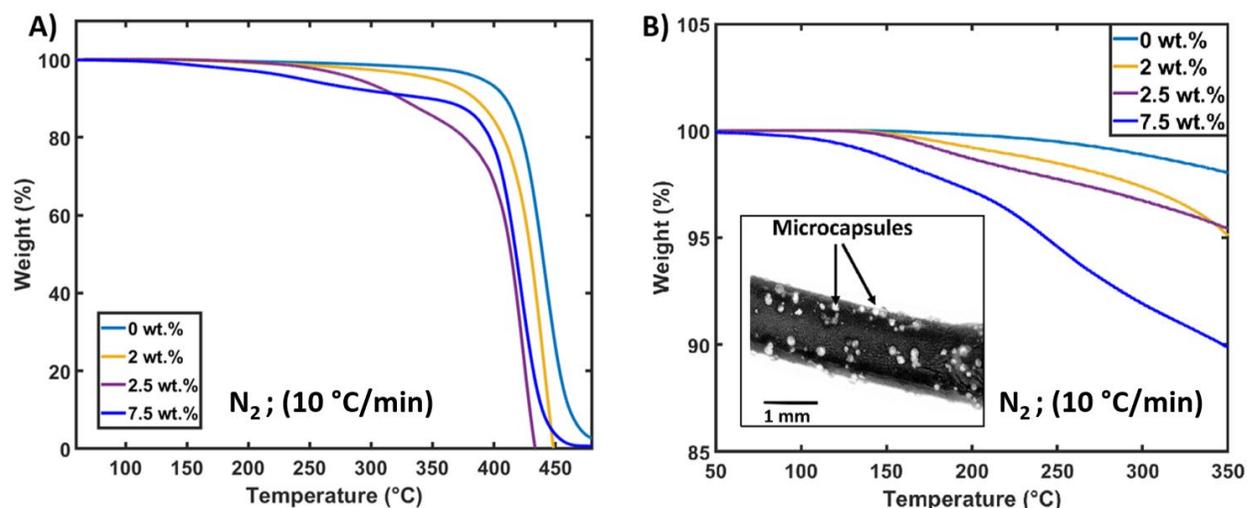
Figure 5.8. TGA thermograms of microcapsule coated filaments with increasing concentration

of microcapsules (0, 2, 2.5, 7.5 wt.%) A) Full thermogram, B) Thermogram representing initial

10 wt.% mass loss up to 350 °C.

To assess the capability of self-healing microcapsules to survive the FFF printing process,

specimens were 3D printed using microcapsule coated filament containing 7.5 wt.%

microcapsules. The presence of unbroken microcapsules after 3D printing was then evaluated by

mechanically crushing the specimen, rinsing with chloroform, and characterizing the presence of

EPA fluid in the chloroform rinse via ^{1}H-NMR spectroscopy. In the resulting ^{1}H-NMR spectrum

shown in Figure 5.9, the presence of EPA is confirmed from the known methylene (-C**H$_2$-**, 3.5

ppm), terminal methylene (-C**H$_2$-**, 4.25 ppm) and terminal alkyl (-C**H$_3$**, 1.5 ppm) peaks for EPA.

As expected, the spectrum also shows characteristic peaks corresponding to the aromatic ring of

polystyrene in the range of 6.3 – 7.2 ppm. Overall, this simple experiment confirms that

microcapsules remain intact after the FFF 3D printing process performed at elevated temperature (205 °C).
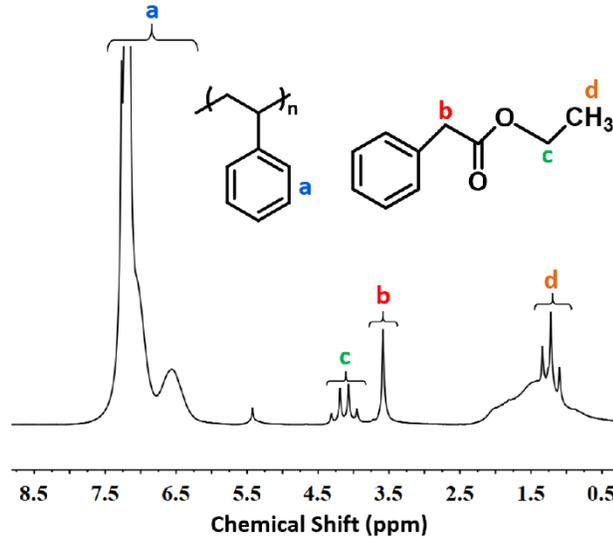
Figure 5.9. ^{1}H-NMR spectrum of crushed FFF printed specimen showing the presence of EPA and thereby intact microcapsules in the printed specimen.

5.3.5. Dynamic Mechanical analysis

The impact of microcapsules on storage modulus (E') and Tg was evaluated using DMA with 3 replicates of each printed specimen type. As shown in Table 5.2, the presence of microcapsules in 3D printed composites slightly decreases both the storage modulus (microcapsules act as small defects and increases stress concentration zones in the polymer matrix decreasing E') [37], [64]. and the observed Tg; obtained from peak value of tan delta curve of the HIPS composites. To investigate the extent of these impacts on E' and Tg, the mean and standard deviation of all values of both specimen (0 and 7.5 wt.%) were calculated to find the coefficient of variance (CV, the ratio of standard deviation to mean). A CV of 0.346 for E' and 0.05 for Tg were obtained. Such low values of CV (less than 0.5) for storage modulus and the obtained small standard deviations (Table

5.2) indicate low data spread or variation in values. Overall, while the addition of microcapsules

impacts both *E'* and *Tg*, the impact is relatively small.

Table 5.2. Storage modulus (E') and glass transition temperature (Tg) of FFF printed HIPS

composites

Microcapsule Loading (wt.%)	$E' \times 10^8$ (Pa)	Tg (°C)
0	2.23 ± 0.29	111 ± 2
7.5	1.26 ± 0.25	103 ± 4

5.3.6. Self-healing behavior

Evidence of microcrack healing in 3D printed self-healing polymer composites was first assessed

through SEM imaging of a 3D printed composite containing 7.5 wt.% microcapsules before and

after crack healing (Figure 5.10). After healing (Figure 5.10D) a thin layer of polymer film has

formed over the crack surface, closing the gap and recovering the fracture toughness. However, it

is also clear in Figure 5.10D that this particular crack is not completely healed, likely due to the

size of the fracture and not enough solvent being released from microcapsules at the crack site.

This type of partial healing limits the resulting fracture toughness after healing (discussed below)

and could potentially be improved with higher loadings of microcapsules.
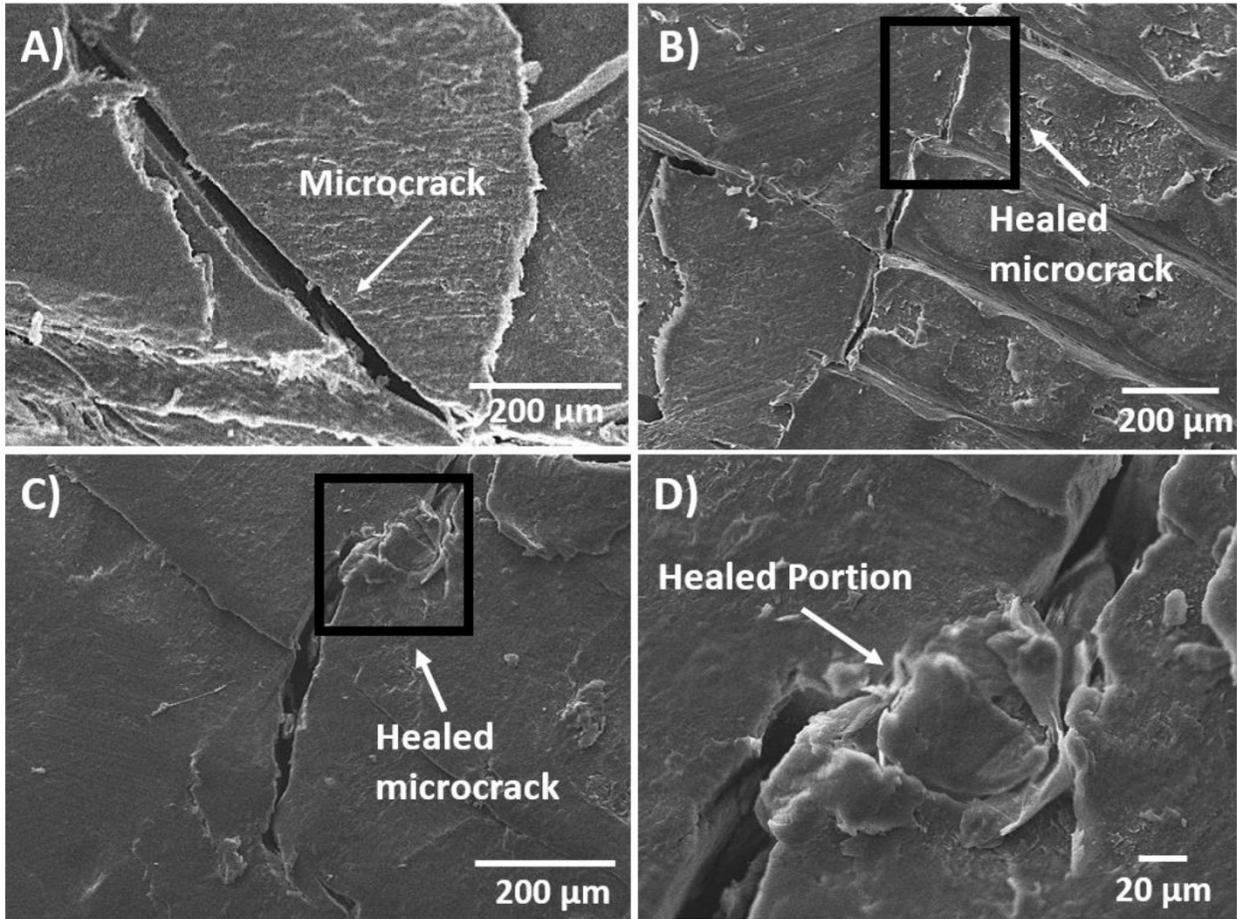
Figure 5.10. SEM images of A) microcrack prior to healing, B) microcrack post- healing, C) and D) enlarged images of healed microcrack.

The fracture recovery in specimens printed with 7.5 wt.% EPA microcapsule-loaded filament were determined via single edge notch beam (SENB) test. SENB is a fracture toughness test, commonly used to investigate fracture toughness in polymer materials and in metals [19]. A schematic of the fracture test performed for FFF printed polymer composite is shown in Figure 5.11. After the fracture event, pre-notched and pre-cracked composites were allowed to heal at room temperature (24 °C) for 24 and 72 hours. Here, Fracture toughness after "healing" of specimens without microcapsules wasn't performed as once tested samples without self-healing

148

microcapsules are fractured and further fracture testing along those fracture planes is precluded. Here, specimens without microcapsules are used to show the difference in initial fracture toughness between specimens with self-healing composites (microcapsule loaded fracture toughness) and those without microcapsules but prepared similarly. As seen in Table 5.3, the fracture toughness of the virgin FFF printed HIPS composites decreases in the presence of microcapsules. This behavior has been observed with other composites and it is believed that the microcapsules act as small defects in the polymer matrix, thus affecting overall fracture toughness of self-healing composites [65]–[67]. However, the self-healing impact of the microcapsules is clearly visible after the HIPS composites were allowed to heal for certain healing times. HIPS self-healing composites showed fracture toughness recovery after 24 and 72 hours with 67 % and 81 % healing efficiency, respectively. The material behavior is therefore somewhat of a tradeoff between the ultimate fracture toughness and the ability to self-heal which must then be considered when assessing the ultimate potential lifetime of these materials for applications or use cases. The increased fracture recovery with increase in healing time is consistent with other literature results on related self-healing polymer materials [39], [68].

These fracture recovery results are comparable to other reports which utilized the 3D printing approach to incorporate self-healing functionality in polymer materials. For self-healing of thermoplastic polymers, Villajos et. al. reported on poly(ethylene-co-methacrylic acid) (EMAA) copolymers reinforced with carbon nanotubes for 3D printing of self-healing composites and observed 66% fracture toughness recovery [69]. Here, there is a limitation in material choice as intrinsic self-healing systems typically require modifications to the polymer chemistry to include moieties that undergo reversible bond formation ability such as hydrogen bonding, ionic interactions, and disulfide bonds. For example, Ritzen et. al. utilized polyurethane polymer and an

intrinsic self-healing mechanism where hydrogen bonding forms at the broken interface among urethane units with full recovery of fracture toughness after damage event [70]. In our work, we achieve 81% healing efficiency for, to the best of our knowledge, the first reported autonomous microcapsule-based self-healing of FFF 3D printed HIPS composites.
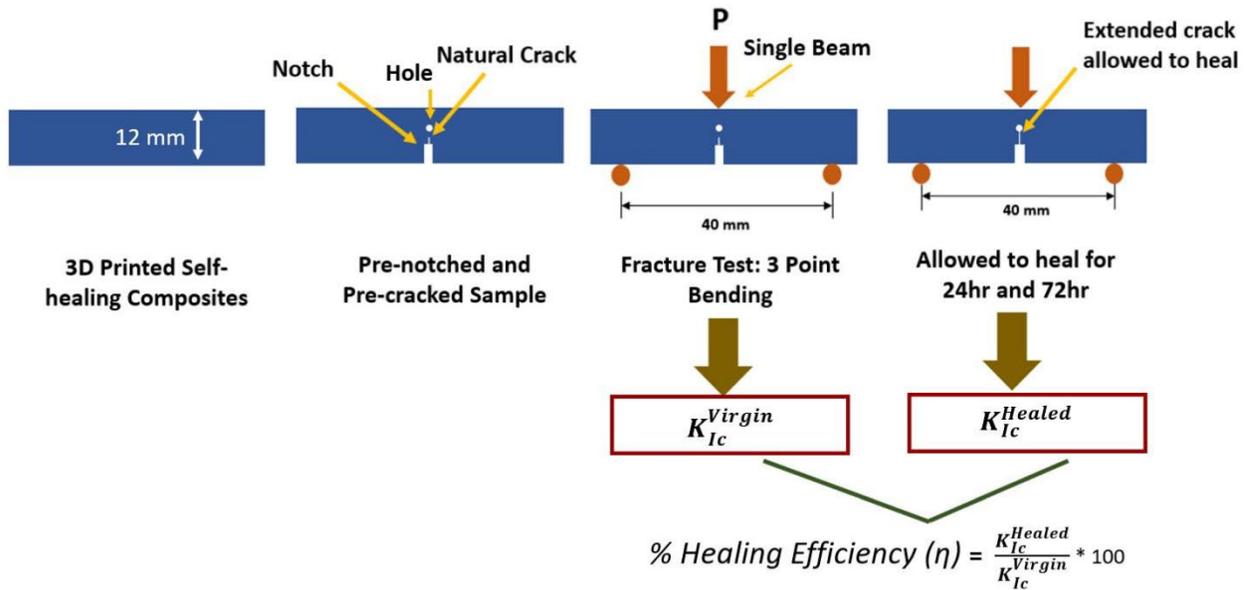
Figure 5.11. A schematic of single edge notch beam (SENB) fracture toughness test.

Table 5.3. Pre-healing and post healing fracture toughness of 3D printed HIPS composites.

Microcapsule Loading (wt.%)	Pre-healing Fracture Toughness (MPa.m$^{1/2}$)	Post Healing Fracture Toughness (MPa.m$^{1/2}$)	Healing efficiency (%)	Post Healing Fracture Toughness (MPa.m$^{1/2}$)	Healing efficiency (%)
		24 hours		72 hours	
0	4.23 ± 0.94	-	-	-	-
7.5	3.36 ± 0.34	2.24 ± 0.31	67	2.73 ± 0.02	81

5.4. Conclusion

In this work, double-walled microcapsules containing the environmentally friendly green solvent ethyl phenylacetate were synthesized, incorporated in FFF printed HIPS composites, and the efficacy of their solvent-based self-healing investigated. Microcapsules were coated on HIPS filaments using a continuous bath coating process, and microcapsule-coated filaments were used to 3D print HIPS composites. ^{1}H-NMR and thermogravimetric analysis showed the presence of intact microcapsules after coating and after the 3D printing process. Fracture toughness of virgin and healed HIPS composites was investigated via single edge notch beam (SENB) tests and a maximum healing efficiency of 81% was obtained by HIPS composites containing 7.5 wt.% microcapsules. Enhancement in fracture toughness recovery in FFF printed structures implies that microcapsules coating on polymer filaments can allow 3D printing of self-healing polymer composites and extend material lifetime and reliability. This study provides a platform for self-healing of other thermoplastic polymer materials via solvent-based self-healing approach.

5.5. References

[1]   Gross, B. C.; Erkal, J. L.; Lockwood, S. Y.; Chen, C.; Spence, D. M. Evaluation of 3D Printing and Its Potential Impact on Biotechnology and the Chemical Sciences. *Anal. Chem.* **2014**, *86* (7), 3240-3253. https://doi.org/10.1021/ac403397r.

[2]   Hofmann, M. 3D Printing Gets a Boost and Opportunities with Polymer Materials. *ACS Macro Letters*. **2014**, 3, 382-386. https://doi.org/10.1021/mz4006556.

[3]   Lee, C.; Kim, M.; Kim, Y. J.; Hong, N.; Ryu, S.; Kim, H. J.; Kim, S. Soft Robot Review. *International Journal of Control, Automation and Systems*. *Institute of Control, Robotics and Systems* **2017**, 3–15. https://doi.org/10.1007/s12555-016-0462-3.

[4]   Dodziuk, H. Applications of 3D Printing in Healthcare. *Kardiochirurgia i Torakochirurgia Pol.* **2016**, *13* (3), 283–293. https://doi.org/10.5114/kitp.2016.62625.

[5]   Lee, J. Y.; An, J.; Chua, C. K. Fundamentals and Applications of 3D Printing for Novel Materials. *Appl. Mater. Today* **2017**, *7*, 120–133. https://doi.org/10.1016/j.apmt.2017.02.004.

[6]   Long, J.; Gholizadeh, H.; Lu, J.; Bunt, C.; Seyfoddin, A. Application of Fused Deposition Modelling (FDM) Method of 3D Printing in Drug Delivery. *Curr. Pharm. Des.* **2016**, *23* (3),433-439. https://doi.org/10.2174/1381612822666161026162707.

[7]   Sathies, T.; Senthil, P.; Anoop, M. S. A Review on Advancements in Applications of Fused Deposition Modelling Process. *Rapid Prototyping Journal*. 2020, pp 669–687. https://doi.org/10.1108/RPJ-08-2018-0199.

[8]   Dul, S.; Fambri, L.; Pegoretti, A. Fused Deposition Modelling with ABS-Graphene Nanocomposites. *Compos. Part A Appl. Sci. Manuf.* **2016**, *85,* 181-191. https://doi.org/10.1016/j.compositesa.2016.03.013.

[9]   Boschetto, A.; Bottini, L. Accuracy Prediction in Fused Deposition Modeling. *Int. J. Adv. Manuf. Technol.* **2014**, *73* (5–8). https://doi.org/10.1007/s00170-014-5886-4.

[10]   Wickramasinghe, S.; Do, T.; Tran, P. FDM-Based 3D Printing of Polymer and Associated Composite: A Review on Mechanical Properties, Defects and Treatments, *Polymers*. **2020**, 1529.https://doi.org/10.3390/polym12071529.

[11]   Wolf, M.; Elser, A.; Riedel, O.; Verl, A. A Software Architecture for a Multi-Axis Additive Manufacturing Path-Planning Tool. In *Procedia CIRP*; **2020;** Vol. 88, 433-438. https://doi.org/10.1016/j.procir.2020.05.075.

[12]   Chohan, J. S.; Singh, R.; Boparai, K. S.; Penna, R.; Fraternali, F. Dimensional Accuracy

Analysis of Coupled Fused Deposition Modeling and Vapour Smoothing Operations for Biomedical Applications. *Compos. Part B Eng.* **2017**, *117*, 138-149.https://doi.org/10.1016/j.compositesb.2017.02.045.

[13] Rajpurohit, S. R.; Dave, H. K. Analysis of Tensile Strength of a Fused Filament Fabricated PLA Part Using an Open-Source 3D Printer. *Int. J. Adv. Manuf. Technol.* **2019**, *101* (5–8). https://doi.org/10.1007/s00170-018-3047-x.

[14] WANG, P.; ZOU, B.; DING, S.; LI, L.; HUANG, C. Effects of FDM-3D Printing Parameters on Mechanical Properties and Microstructure of CF/PEEK and GF/PEEK. *Chinese J. Aeronaut.* **2020**, *34(9)*, 236-243 https://doi.org/10.1016/j.cja.2020.05.040.

[15] Ngo, T. D.; Kashani, A.; Imbalzano, G.; Nguyen, K. T. Q.; Hui, D. Additive Manufacturing (3D Printing): A Review of Materials, Methods, Applications and Challenges. *Composites Part B: Engineering.* **2018**, *143*, 172-196 https://doi.org/10.1016/j.compositesb.2018.02.012.

[16] Mohamed, O. A.; Masood, S. H.; Bhowmik, J. L. Optimization of Fused Deposition Modeling Process Parameters: A Review of Current Research and Future Prospects. *Adv. Manuf.* **2015**, *3* (1), 42-53. https://doi.org/10.1007/s40436-014-0097-7.

[17] Parandoush, P.; Lin, D. A Review on Additive Manufacturing of Polymer-Fiber Composites. *Composite Structures*. **2017**. https://doi.org/10.1016/j.compstruct.2017.08.088.

[18] Brenken, B.; Barocio, E.; Favaloro, A.; Kunc, V.; Pipes, R. B. Fused Filament Fabrication of Fiber-Reinforced Polymers: A Review. *Additive Manufacturing.* **2018**, *(21)*, 1-16. https://doi.org/10.1016/j.addma.2018.01.002.

[19] Shinde, V. V.; Celestine, A. D.; Beckingham, L. E.; Beckingham, B. S. Stereolithography

3D Printing of Microcapsule Catalyst-Based Self-Healing Composites. *ACS Appl. Polym. Mater.* **2020**, *2* (11), 5048-5057 . https://doi.org/10.1021/acsapm.0c00872.

[20] Gladman, A. S.; Celestine, A.-D. N.; Sottos, N. R.; White, S. R. Self-Healing Materials: Autonomic Healing of Acrylic Bone Cement (Adv. Healthcare Mater. 2/2015). *Adv. Healthc. Mater.* **2015**, *4* (2), 170–170. https://doi.org/10.1002/adhm.201570009.

[21] White, S. R.; Sottos, N. R.; Geubelle, P. H.; Moore, J. S.; Kessler, M. R.; Sriram, S. R.; Brown, E. N.; Viswanathan, S. Autonomic Healing of Polymer Composites. *Nature*. **2001,** *409*, 794-797. https://doi.org/10.1038/35057232.

[22] Zhang, F.; Ju, P.; Pan, M.; Zhang, D.; Huang, Y.; Li, G.; Li, X. Self-Healing Mechanisms in Smart Protective Coatings: A Review. *Corrosion Science*. **2018**, *144*, 74-88. https://doi.org/10.1016/j.corsci.2018.08.005.

[23] Mihashi, H.; Nishiwaki, T. Development of Engineered Self-Healing and Self-Repairing Concrete-State-of-the-Art Report. *Journal of Advanced Concrete Technology*. **2012**, *10(5)*, 170-184.https://doi.org/10.3151/jact.10.170.

[24] Blaiszik, B. J.; Kramer, S. L. B.; Olugebefola, S. C.; Moore, J. S.; Sottos, N. R.; White, S. R. Self-Healing Polymers and Composites. *Annu. Rev. Mater. Res.* **2010**, *40,* 179-211. https://doi.org/10.1146/annurev-matsci-070909-104532.

[25] *Self-Healing Polymer-Based Systems*; Elsevier, **2020**. https://doi.org/10.1016/c2018-0-03002-9.

[26] Hia, I. L.; Vahedi, V.; Pasbakhsh, P. Self-Healing Polymer Composites: Prospects, Challenges, and Applications. *Polymer Reviews*. **2016**, 225-261. https://doi.org/10.1080/15583724.2015.1106555.

[27] Chen, X.; Dam, M. A.; Ono, K.; Mal, A.; Shen, H.; Nutt, S. R.; Sheran, K.; Wudl, F. A

Thermally Re-Mendable Cross-Linked Polymeric Material. *Science (80-.).* **2002**, *295* (5560), 1698-1702. https://doi.org/10.1126/science.1065879.

[28] Dell'Olio, C.; Yuan, Q.; Varley, R. J. Epoxy/Poly(Ethylene-Co-Methacrylic Acid) Blends as Thermally Activated Healing Agents in an Epoxy/Amine Network. *Macromol. Mater. Eng.* **2015**, *300* (1), 70-79. https://doi.org/10.1002/mame.201400126.

[29] Ling, J.; Rong, M. Z.; Zhang, M. Q. Coumarin Imparts Repeated Photochemical Remendability to Polyurethane. *J. Mater. Chem.* **2011**, *21* (45), 18373-18380. https://doi.org/10.1039/c1jm13467a.

[30] Utrera-Barrios, S.; Verdejo, R.; López-Manchado, M. A.; Hernández Santana, M. Evolution of Self-Healing Elastomers, from Extrinsic to Combined Intrinsic Mechanisms: A Review. *Materials Horizons*. **2020**, 2882-2902. https://doi.org/10.1039/d0mh00535e.

[31] Caruso, M. M.; Blaiszik, B. J.; Jin, H.; Schelkopf, S. R.; Stradley, D. S.; Sottos, N. R.; White, S. R.; Moore, J. S. Robust, Double-Walled Microcapsules for Self-Healing Polymeric Materials. *ACS Appl. Mater. Interfaces* **2010**, *2* (4), 1195-1199. https://doi.org/10.1021/am100084k.

[32] Ullah, H.; Azizli, K. A. M.; Man, Z. B.; Che Ismail, M. B.; Khan, M. I. The Potential of Microencapsulated Self-Healing Materials for Microcracks Recovery in Self-Healing Composite Systems: A Review. *Polymer Reviews*. **2016**, 429-485. https://doi.org/10.1080/15583724.2015.1107098.

[33] Kim, D. M.; Song, I. H.; Choi, J. Y.; Jin, S. W.; Nam, K. N.; Chung, C. M. Self-Healing Coatings Based on Linseed-Oil-Loaded Microcapsules for Protection of Cementitious Materials. *Coatings* **2018**, *8* (11), 404. https://doi.org/10.3390/COATINGS8110404.

[34] Gao, L.; He, J.; Hu, J.; Wang, C. Photoresponsive Self-Healing Polymer Composite with

Photoabsorbing Hybrid Microcapsules. *ACS Appl. Mater. Interfaces* **2015**, *7* (45), 25546-25552. https://doi.org/10.1021/acsami.5b09121.

[35] Shields, Y.; De Belie, N.; Jefferson, A.; Van Tittelboom, K. A Review of Vascular Networks for Self-Healing Applications. *Smart Materials and Structures*. **2021**, 063001. https://doi.org/10.1088/1361-665X/abf41d.

[36] White, S. R.; Moore, J. S.; Sottos, N. R.; Krull, B. P.; Santa Cruz, W. A.; Gergely, R. C. R. Restoration of Large Damage Volumes in Polymers. *Science (80-.).* **2014**, *344* (6184), 620–623. https://doi.org/10.1126/science.1251135.

[37] Shinde, V. V.; Shelke, S. D.; Celestine, A. N.; Beckingham, B. S. Self-healing in High Impact Polystyrene (HIPS) Composites via Embedded Non-toxic Solvent-filled Microcapsules . *J. Appl. Polym. Sci.* **2021**, *139* (2), 51463. https://doi.org/10.1002/app.51463.

[38] Caruso, M. M.; Delafuente, D. A.; Ho, V.; Sottos, N. R.; Moore, J. S.; White, S. R. Solvent-Promoted Self-Healing Epoxy Materials. *Macromolecules* **2007**, *40* (25), 8830-8832. https://doi.org/10.1021/ma701992z.

[39] Celestine, A. D. N.; Sottos, N. R.; White, S. R. Autonomic Healing of PMMA via Microencapsulated Solvent. *Polymer (Guildf).* **2015**, *69,* 1-8. https://doi.org/10.1016/j.polymer.2015.03.072.

[40] Li, S.; Yerneni, S. S.; Feinberg, A. W.; Campbell, P. G. Three-Dimensional Printable Hydrogel Precursor Bioinks as Growth Factor Delivery Vehicles. In *Transactions of the Annual Meeting of the Society for Biomaterials and the Annual International Biomaterials Symposium*; **2019**; Vol. 40.

[41] Kuang, X.; Chen, K.; Dunn, C. K.; Wu, J.; Li, V. C. F.; Qi, H. J. 3D Printing of Highly

Stretchable, Shape-Memory, and Self-Healing Elastomer toward Novel 4D Printing. *ACS Appl. Mater. Interfaces* **2018**, *10* (8), 7381-7388. https://doi.org/10.1021/acsami.7b18265.

[42] Nadgorny, M.; Xiao, Z.; Connal, L. A. 2D and 3D-Printing of Self-Healing Gels: Design and Extrusion of Self-Rolling Objects. *Mol. Syst. Des. Eng.* **2017**, *2* (3), 283-292. https://doi.org/10.1039/c7me00023e.

[43] Liu, S.; Li, L. Ultrastretchable and Self-Healing Double-Network Hydrogel for 3D Printing and Strain Sensor. *ACS Appl. Mater. Interfaces* **2017**, *9* (31), 26429-26437. https://doi.org/10.1021/acsami.7b07445.

[44] Sanders, P.; Young, A. J.; Qin, Y.; Fancey, K. S.; Reithofer, M. R.; Guillet-Nicolas, R.; Kleitz, F.; Pamme, N.; Chin, J. M. Stereolithographic 3D Printing of Extrinsically Self-Healing Composites. *Sci. Rep.* **2019**, *9* (1). https://doi.org/10.1038/s41598-018-36828-9.

[45] Singh, J.; Chawla, K.; Singh, R. Applications of Thermoplastic Polymers in 3D Printing. In *Reference Module in Materials Science and Materials Engineering*; **2020**. https://doi.org/10.1016/b978-0-12-820352-1.00010-9.

[46] Garcia-Ivars, J.; Wang-Xu, X.; Iborra-Clar, M. I. Application of Post-Consumer Recycled High-Impact Polystyrene in the Preparation of Phase-Inversion Membranes for Low-Pressure Membrane Processes. *Sep. Purif. Technol.* **2017**, *175,* 340-351. https://doi.org/10.1016/j.seppur.2016.11.061.

[47] Valino, A. D.; Dizon, J. R. C.; Espera, A. H.; Chen, Q.; Messman, J.; Advincula, R. C. Advances in 3D Printing of Thermoplastic Polymer Composites and Nanocomposites. *Progress in Polymer Science*. **2019**, *98*, 101162 https://doi.org/10.1016/j.progpolymsci.2019.101162.

[48] Hansen, C. M. *Hansen Solubility Parameters: A User's Handbook: Second Edition*; **2007**.

https://doi.org/10.1201/9781420006834.

[49] Venkatram, S.; Kim, C.; Chandrasekaran, A.; Ramprasad, R. Critical Assessment of the Hildebrand and Hansen Solubility Parameters for Polymers. *J. Chem. Inf. Model.* **2019**, 4188-4194. https://doi.org/10.1021/acs.jcim.9b00656.

[50] Pickering, S. J. *Management, Recycling and Reuse of Waste Composites*; Elsevier, **2010**.

[51] da Silva, D. J.; Wiebeck, H. Current Options for Characterizing, Sorting, and Recycling Polymeric Waste. *Progress in Rubber, Plastics and Recycling Technology*. **2020**, *36(4)*, 1-20 https://doi.org/10.1177/1477760620918603.

[52] Narancic, T.; Cerrone, F.; Beagan, N.; O'Connor, K. E. Recent Advances in Bioplastics: Application and Biodegradation. *Polymers*. **2020**, *12(4)*, 920https://doi.org/10.3390/POLYM12040920.

[53] Ignatyev, I. A.; Thielemans, W.; Vander Beke, B. Recycling of Polymers: A Review. *ChemSusChem*. **2014**, 7(6), 1579-1593. https://doi.org/10.1002/cssc.201300898.

[54] Chiplunkar, P. P.; Shinde, V. V.; Pratap, A. P. Synthesis and Application of Palm Fatty Acid Distillate Based Alkyd Resin in Liquid Detergent. *J. Surfactants Deterg.* **2017**, *20* (1), 137–149. https://doi.org/10.1007/s11743-016-1905-9.

[55] Sweeney, C. B.; Lackey, B. A.; Pospisil, M. J.; Achee, T. C.; Hicks, V. K.; Moran, A. G.; Teipel, B. R.; Saed, M. A.; Green, M. J. Welding of 3D-Printed Carbon Nanotube–Polymer Composites by Locally Induced Microwave Heating. *Sci. Adv.* **2017**, *3* (6), 1–7. https://doi.org/10.1126/sciadv.1700262.

[56] ASTM International. (ASTM D 5054) - Standard Test Methods for Plane-Strain Fracture Toughness and Strain Energy Release Rate of Plastic Materials. *ASTM B. Stand.* **2013**, *99* (Reapproved 2007), 1–9. https://doi.org/10.1520/D5045-14.priate.

[57] Mwema, F. M.; Akinlabi, E. T. Basics of Fused Deposition Modelling (FDM). In *SpringerBriefs in Applied Sciences and Technology*; **2020**, 1-15. https://doi.org/10.1007/978-3-030-48259-6_1.

[58] Caruso, M. M.; Blaiszik, B. J.; White, S. R.; Sottos, N. R.; Moore, J. S. Full Recovery of Fracture Toughness Using a Nontoxic Solvent-Based Self-Healing System. *Adv. Funct. Mater.* **2008**, *18* (13), 1898-1904. https://doi.org/10.1002/adfm.200800300.

[59] Blaiszik, B. J.; Kramer, S. L. B.; Olugebefola, S. C.; Moore, J. S.; Sottos, N. R.; White, S. R. Self-Healing Polymers and Composites. *Annu. Rev. Mater. Res.* **2010**, *40*, 179–211. https://doi.org/10.1146/annurev-matsci-070909-104532.

[60] Brown, E. N.; Kessler, M. R.; Sottos, N. R.; White, S. R. In Situ Poly(Urea-Formaldehyde) Microencapsulation of Dicyclopentadiene. *J. Microencapsul.* **2003**, *20* (6), 719-730. https://doi.org/10.1080/0265204031000154160.

[61] Kosarli, M.; Bekas, D. G.; Tsirka, K.; Baltzis, D.; Vaimakis-Tsogkas, D.; Orfanidis, S.; Papavassiliou, G.; Paipetis, A. S. Microcapsule-Based Self-Healing Materials: Healing Efficiency and Toughness Reduction vs. Capsule Size. *Compos. Part B Eng.* **2019**, *171,* 78-86. https://doi.org/10.1016/j.compositesb.2019.04.030.

[62] Kang, S.; Baginska, M.; White, S. R.; Sottos, N. R. Core-Shell Polymeric Microcapsules with Superior Thermal and Solvent Stability. *ACS Appl. Mater. Interfaces* **2015**, *7* (20), 10952-10956. https://doi.org/10.1021/acsami.5b02169.

[63] Sun, D.; An, J.; Wu, G.; Yang, J. Double-Layered Reactive Microcapsules with Excellent Thermal and Non-Polar Solvent Resistance for Self-Healing Coatings. *J. Mater. Chem. A* **2015**, *3* (8), 4435-4444. https://doi.org/10.1039/c4ta05339g.

[64] Heo, Y.; Malakooti, M. H.; Sodano, H. A. Self-Healing Polymers and Composites for

Extreme Environments. *J. Mater. Chem. A* **2016**, *4* (44), 17403-17411.

https://doi.org/10.1039/c6ta06213j.

[65]   Antich, P.; Vázquez, A.; Mondragon, I.; Bernal, C. Mechanical Behavior of High Impact

Polystyrene Reinforced with Short Sisal Fibers. *Compos. Part A Appl. Sci. Manuf.* **2006**, *37*

(1), 139-150. https://doi.org/10.1016/j.compositesa.2004.12.002.

[66]   Albdiry, M. T.; Yousif, B. F. Toughening of Brittle Polyester with Functionalized

Halloysite Nanocomposites. *Compos. Part B Eng.* **2019**, *160,* 94-109.

https://doi.org/10.1016/j.compositesb.2018.10.032.

[67]   Brown, E. N.; White, S. R.; Sottos, N. R. Fatigue Crack Propagation in Microcapsule-

Toughened Epoxy. *J. Mater. Sci.* **2006**, *41* (19), 6266-6273.

https://doi.org/10.1007/s10853-006-0512-y.

[68]   Neuser, S.; Michaud, V.; White, S. R. Improving Solvent-Based Self-Healing Materials

through Shape Memory Alloys. *Polymer (Guildf).* **2012**, *53* (2), 370-378.

https://doi.org/10.1016/j.polymer.2011.12.020.

[69]   Calderón-Villajos, R.; López, A. J.; Peponi, L.; Manzano-Santamaría, J.; Ureña, A. 3D-

Printed Self-Healing Composite Polymer Reinforced with Carbon Nanotubes. *Mater. Lett.*

2019, *249,* 91-94. https://doi.org/10.1016/j.matlet.2019.04.069.

[70]   Ritzen, L.; Montano, V.; Garcia, S. J. 3d Printing of a Self-Healing Thermoplastic

Polyurethane through Fdm: From Polymer Slab to Mechanical Assessment. *Polymers*

(Basel). **2021**, *13* (2), 305. https://doi.org/10.3390/polym13020305.

Chapter 6

3D Printing of Reactive Porous Media

Collaborative work with Dr. Lauren Beckingham and PhD student Abdullah Al Nahian.

6.1. Introduction

Increased atmospheric carbon dioxide (CO_2) which captures outgoing infrared (IR) radiation from Earth's surface has led to a subsequent increase in near-surface global temperatures [1], [2] Therefore, scientists are trying various ways to reduce the amount of CO_2 released into the atmosphere and to capture atmospheric CO_2 in the subsurface systems. Geologic carbon sequestration secures CO_2 in deep geologic formations to prevent its release to the atmosphere and from contributing to climate change [3]–[6]. However, geological systems are heterogeneous, containing different layers of rock, differentiating in pores and grains [7], [8]. Hence, to ensure the environmental sustainability of CO_2 in geologic storage, we must understand the rates and mechanisms of essential geochemical reactions that occur in the presence of CO_2. Another issue is scaling; in oil and gas reservoirs, scales of salts deposited in the porous media near the wellbore area result in substantial reduction of the porosity and permeability of the rock formations, causing flow blockage; creating a barrier to the oil extraction process [9]–[11]. The most encountered scales in oil reservoirs consist of calcium carbonate ($CaCO_3$) and calcium sulfate ($CaSO_4$) and calcium phosphate ($Ca_3(PO_4)_2$) salts formed by oil field water, which are mainly produced due to pressure and temperature alterations, respectively [12]. Therefore, understanding the impacts of

porous media properties on geochemical reactions is important but challenging due to the highly heterogeneous nature of rock samples and consequently lack of replication across samples [13]–[15]. In such heterogenous rocks, different geochemical reactions can have a consequential impact on the chemical and physical properties, such as fluid chemistry and evolution of porosity and permeability which increases complexity of the rock properties more. Understanding of these properties in the real rock samples is thereby necessary. One potential way to replicate these reactive rock samples and investigate the impact of mineral dissolution and precipitation on porosity and permeability is 3D printing. 3D printing allows for fabrication of complex 3D objects from X-ray Nano CT images [16]–[18].

A major goal of this project is to understand mineral dissolution and precipitation reactions and impacts on porosity and permeability in porous media using 3D printing approach. This study uses fused filament fabrication (FFF) 3D printing to fabricate multiple replicates of identical pore structures. To incorporate reactive minerals (i.e., calcite) into the structure, a surface functionalization and calcite growth approach is used. According to literature, sulphonated polystyrene was found to be the suitable platform for calcite crystal growth [19]. High impact polystyrene (HIPS) is used as the material for porous media fabrication via FFF, and is subsequently treated to present sulfonic acid moieties on the surface to seed the growth of calcite. Here, to investigate the capability of precipitating calcite crystals on a 3D printed polymer surface, 2D polymer films are used for this study. Fabrication, and surface functionalization of 2D polymer films has successfully shown the presence of desired surface functional groups by ^{1}H-NMR and FTIR spectroscopy. The precipitation of calcite crystals on these reactive 2D HIPS films is performed and evaluated by X-ray Nano CT and X-ray diffraction confirming the growth of calcite. The growth of the precipitated crystals was continuously monitored by optical microscopy

and the rate of crystal growth measured with respect to time. This approach will in the future, be extended to surface functionalization and precipitation of calcite crystals within 3D printed pore structures. Overall, this study provides a platform to use a 3D printing approach for creating reactive rock sample replicates to evaluate mineral reaction and precipitation within porous structures, mimicking geochemical reactions from geochemical systems.

6.2. Materials and Methods

6.2.1. Materials

High Impact Polystyrene (HIPS) thermoplastic polymer pellets were purchased from 3DXTech. Sulfuric acid (98% purity) was purchased from Fisher Scientific. Stock solutions of calcium chloride (0.2 M) and sodium bicarbonate (0.2 M) were prepared from crystalline calcium chloride dihydrate ($CaCl_2 \cdot 2H_2O$) and sodium bicarbonate ($NaHCO_3$) (purchased from BDH chemicals) using deionized, distilled water. The calcium carbonate supersaturated solutions were prepared by in-situ mixing equal volumes of solutions of calcium chloride and sodium bicarbonate. The supersaturated solution was filtered through Whatman filter paper. Deuterated chloroform ($CDCl_3$) was purchased from EMD Millipore.

6.2.2. Experimental Methods

6.2.2.1. Preparation, Functionalization and Characterization of 2D Reactive Polymer films

High Impact polystyrene (HIPS) films were fabricated by compression molding with a Carver (Model 4389) manual heated press at 180 °C. Films were then contacted with 11 M sulfuric acid (98 % pure sulfuric acid diluted to 70 % acid concentration with DI water) at room temperature for different time intervals (2hr, 4hr, 8hr, 1d, 2d). Acid treated films are analyzed for the presence

of sulfonic acid group using FTIR and ^{1}H-NMR spectroscopy. FTIR measurements were performed using a Thermo Scientific Nicolet 6700 FTIR instrument equipped with attenuated total reflection (ATR). ^{1}H-NMR spectroscopy was performed by dissolving acid treated and untreated HIPS films in chloroform, and ^{1}H-NMR spectra were collected on an Oxford Instruments Pulsar 60 MHz spectrometer. Compression molded and acid treated polymer films were visualized under optical microscopy using an Olympus 52x7 microscope with Cellsens software.

6.2.2.2. Calcite Crystal Growth Experiments on 2D polymer films.

The calcite solution (0.2 M) was allowed to flow through acid treated polymer films for 4, 8, 16, 24, 32 and 48 hours at constant flow rate 0.8 ml/min using experimental setup shown in Figure 6.1. The calcite precipitated films' surface was examined post-experiment optically under optical microscope, with ATR-FTIR spectroscopy, X-ray diffraction (XRD), and X-ray Nano CT. X-ray CT analysis of calcite grown HIPS films were performed at voxel resolution of 0.7 micron and obtained using 155 Zeiss 620 Versa located at Auburn University. Obtained images were cropped to obtain a $765 \times 783 \times 783$ voxel cube. Calcium carbonate crystal growth on the 2D polymer film was monitored through an optical microscope (Olympus 52x7 microscope) connected to a computer. Images of the precipitated crystals were captured at distinct time intervals, and the average size of the first observed crystal in each experiment was measured for the investigation of the rates of crystal growth with respect to time.

Metering Pump

Effluent Collector

Polymer film placed inside 3D printed sample holder

Calcite Solution
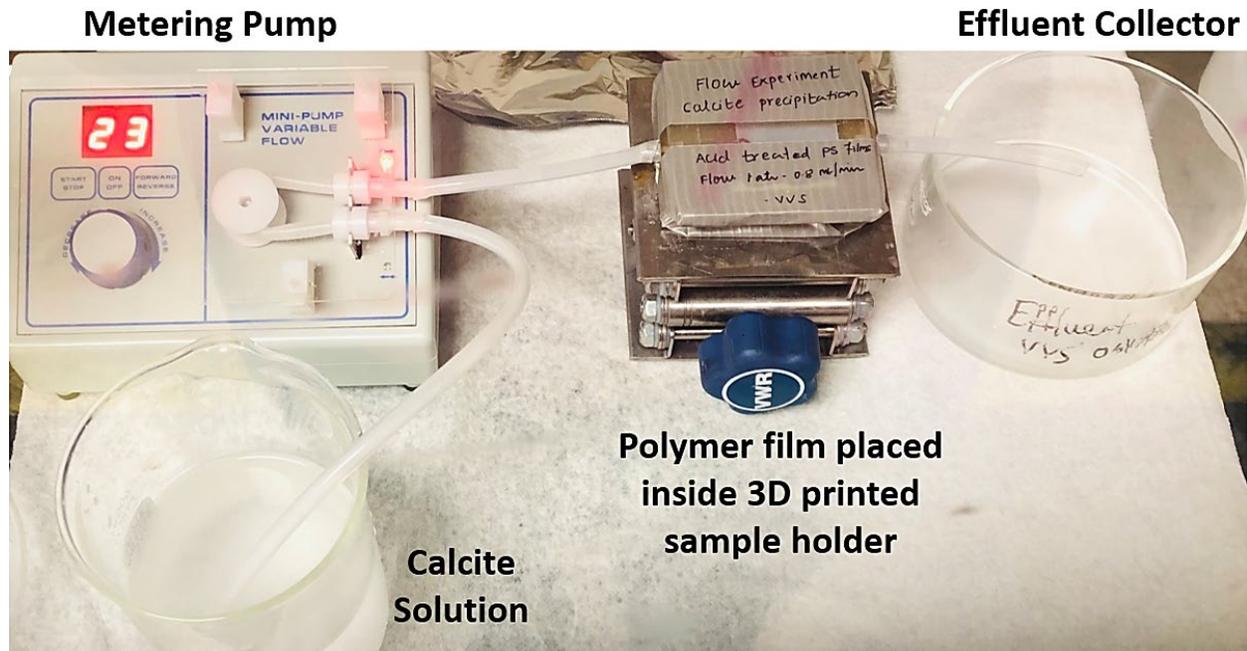
Figure 6.1. Experimental setup for calcite crystal growth on the acid treated polymer films.

6.2.2.3 Generate mesh from CT image of rock and 3D Printing

In this study, a Bentheimer sandstone sample was selected as the basis for the 3D CAD model for FFF 3D printing. 3D Micro-computed Tomography (MicroCT) images were obtained from Digital Rock Portal (Neumann et al., 2020) and cropped into cylinder of 1 mm diameter from original images, Figure 6.2 A, [20]. CT images were segmented into grain and pore space using ImageJ software. A region of interest is selected and 3D volumes in cylindrical form cropped to the uniform size. A mesh based on the grains is generated with Dragonfly software shown Figure 6.2B. The resulting mesh was then enlarged by 7.8, 15 and 20 times to print 3 different sized porous specimens and to ensure that all the pores are reproduced properly. The mesh is converted to a stereolithography (.stl) file to serve as the 3D printing mesh. Cropped grain meshes were printed with high impact polystyrene polymer filament (1.75 mm diameter) using Monoprice IIIP 3D printer and Prusa MK3S shown in Figure 6.2C. Extrusion temperature and bed temperature were

230 -240 °C and 105 °C, respectively. Infill density used was 100%. Porosity value of 3D printed cores was evaluated and compared with the original sandstone core sample porosity value. 3D printed samples fabricated with varying printed parameters are considered (Table 6.2), and the printing parameters that increase the accuracy of replicated rock samples are determined.
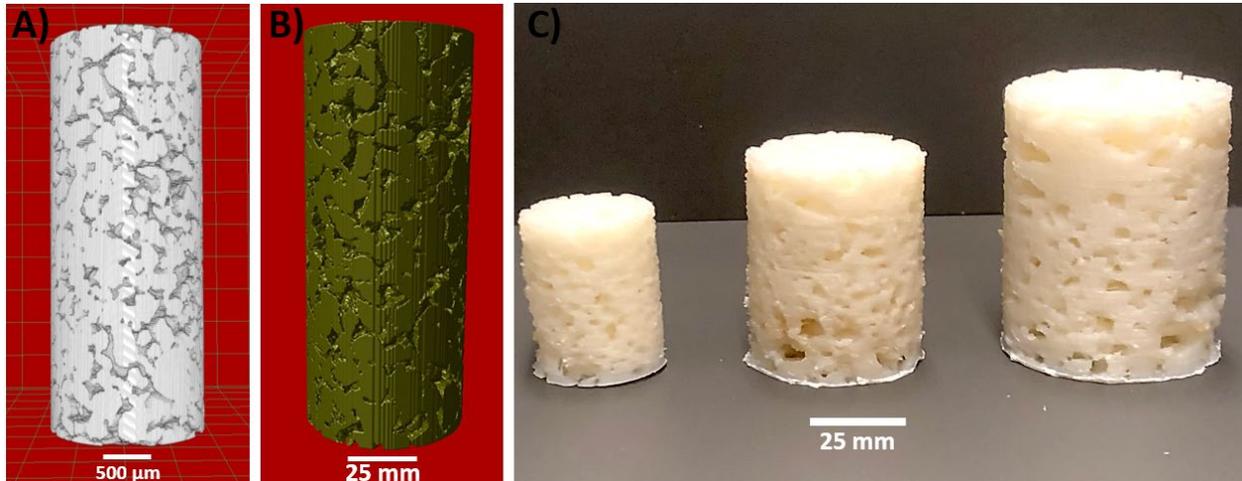
Figure 6.2. A) Thresholded 3D X-ray CT image of Bentheimer sandstone with grains in white, B) 3D stl mesh generated from X-ray CT images corresponding to grains, C) X-ray CT images of 3-D printed samples printed with High Impact Polystyrene filament.

6.3. Results and Discussion

6.3.1. Fabrication and Characterization of 2D reactive polymer films

6.3.1.1. Surface Functionalization of 2D polymer films

Here, to fabricate reactive porous media, a surface functionalization approach is used. We used high impact polystyrene (HIPS) polymer for surface treatment via sulfonation to present sulfonic acid moieties to seed the growth of calcite. Sulfonation of HIPS films with sulfuric acid (98 % purity) was performed over the period of time to yield sulfonated surfaces and increase number of

sulfonic acid groups to enhance polymer hydrophilicity to seed calcite crystals on the polymer surface. After acid treatment, films were weighed and there was no change in weight or surface degradation was observed (shown in Figure 6.3A, 6.3B). Acid treated films (acid treatment for 2 days) are analyzed for presence of sulfonic acid group using ATR-FTIR (Figure 6.3C) and ^{1}H-NMR spectroscopy (Figure 6.3D). The FTIR spectrum of acid treated HIPS in Figure 6.3C shows absorption at 1027 cm^{-1} related to symmetric stretching bond (O=S=O) in SO$_3$H, and band found at 1178 cm^{-1} is referred to (-SO$_2$-O-). The FTIR spectrum showed weak absorption of sulfonic acid groups detected by weak signals. The ^{1}H-NMR spectrum (Figure 6.3D) of sulfonated HIPS showed signal at 7.07 ppm which indicates partial sulfonation of benzene ring in high impact polystyrene.
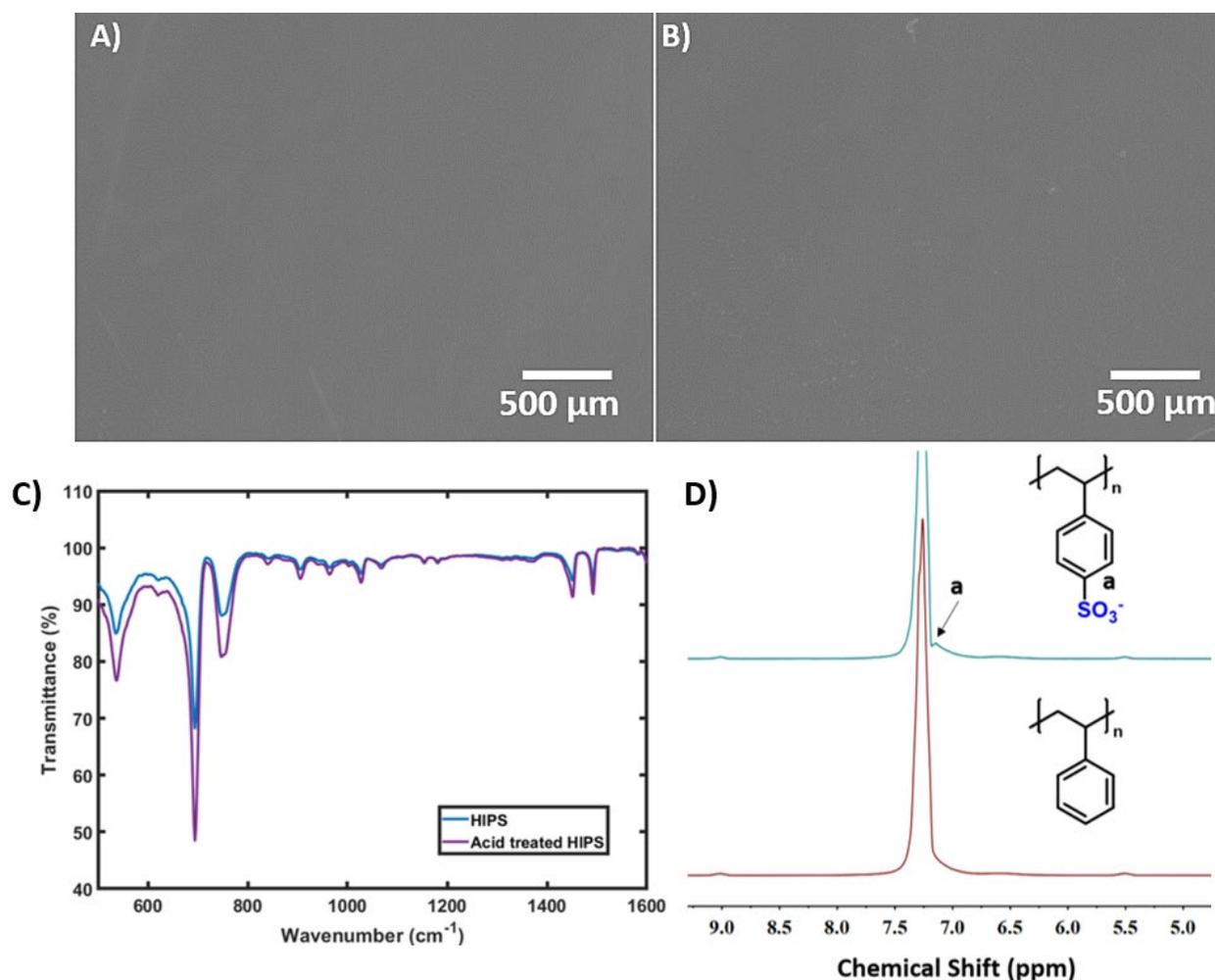
Figure 6.3. Optical microscopic images of 2D HIPS films A) as fabricated, B) after acid treatment in sulfuric acid solution; C) FTIR spectrum of HIPS film (blue) and acid treated HIPS (violet), D) NMR spectrum of HIPS (red), and acid treated HIPS (green).

6.3.1.2. Calcite Crystal Growth

After surface functionalization, precipitation of calcium carbonate from calcite solutions (0.2 M) was investigated on 2D acid treated polymer films' surface. The calcite precipitated films' surface was then examined optically (Figure 6.4D and 6.4E), with ATR FTIR spectroscopy (Figure 6.4A),

X-ray diffraction (Figure 6.4B), and X-ray CT (Figure 6.4C). In optical microscopy images, calcite crystallites are observed in the range of 15-25 μm. From microscopic images, the increase in acid treatment time during sulfonation also leads to an increased numbers of crystallites formed. The ATR-FTIR (Figure 6.4A) spectrum shows strong absorption at 715 cm^{-1},875 cm^{-1}, and broad absorption peak at 1400-1430 cm^{-1}, indicating presence of calcite crystals on the acid treated HIPS specimens. From XRD analysis (Figure 6.4B), a sharp peak signal at 29.5 2-theta corresponding to calcite phase is observed in acid treated HIPS specimens. Therefore, the polymer surface has calcite crystal growth based on this peak location in comparison with bulk calcite powder. Lastly, 3D X-ray CT analysis of calcite grown HIPS films were performed at voxel resolution of 0.7 micron. Obtained images were cropped to obtain a 765 × 783 × 783 voxel cube. In 3D stack image (Figure 6.4C), a yellow voxel corresponds to calcite crystals. Here, we demonstrated the capability of precipitating calcite on 2D HIPS films and approach to enhance calcite crystal growth on polymer surface. We will extend this approach to the surface functionalization and precipitation within 3D printed structures in the future work.
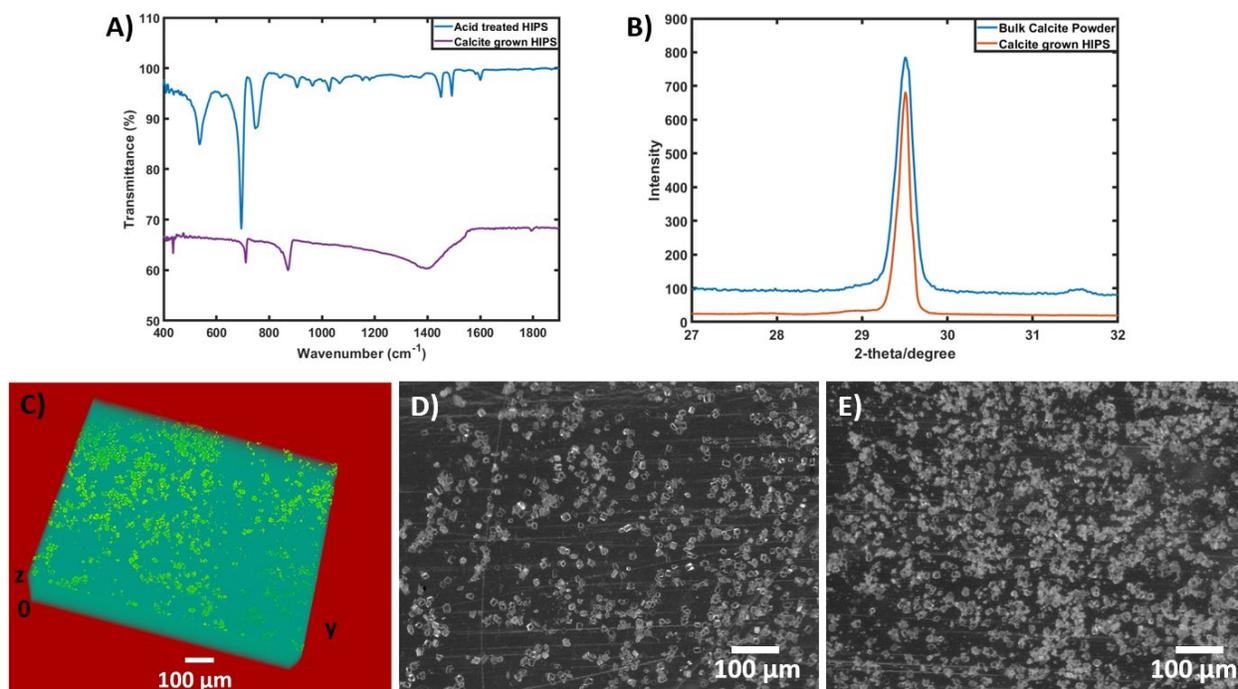
Figure 6.4. Characterization of calcite grown polymer films A) ATR FTIR spectra of acid treated HIPS film (blue) and calcium carbonate treated HIPS film (violet), B) XRD pattern of HIPS film and calcium carbonate treated HIPS film, C) X-ray CT 3D image stack of calcium carbonate treated HIPS films, Optical microscopic images of 2D HIPS films D) after Calcite precipitation for 1 day with 0.2 M calcite solution (1 day acid treated film), E) after Calcite precipitation for 1 day with 0.2 M calcite solution (2-day acid treated film).

Moreover, the growth of the precipitated calcite crystals was continuously monitored by optical microscopy and the rate of crystal growth was measured with respect to time. Figure 6.5 shows the growth of a crystal area (μm^2) as a function of time (hours) at ambient temperature. The surface coverage of 2.57 mm^2 of the polymer film was captured under the microscope. Calcite crystal surface area increased with respect to time and, after 32 hours, the increase of the crystal area reached a plateau value, moving to equilibrium. The final size of the crystal was typically around 17 μm^2.
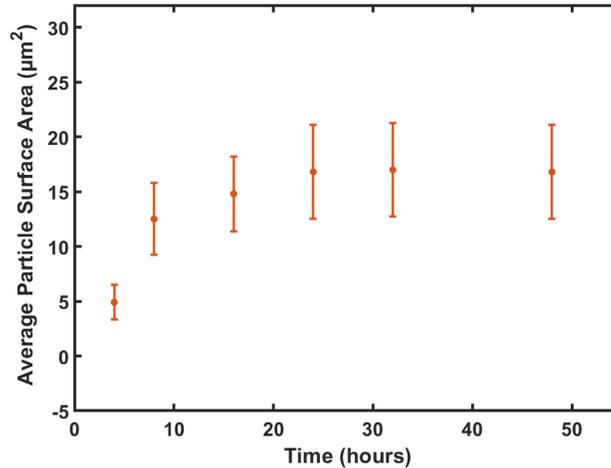
Figure 6.5. Calcite crystal surface area evolution (μm^2) as a function of time (hours) during the precipitation of $CaCO_3$ experiment.

6.3.2. 3D printing of porous media structures

Here, fused filament fabrication 3D printing is used to fabricate sets of physically identical porous media specimen based on real porous media structures. Fused filament fabrication of porous structures with different 3D printing parameters using HIPS filaments are conducted. Sample 1 from Table 6.2, with 100 µm printing resolution, 60 mm/s printing speed resulted into good quality print with some internal printing defects within grains. The measured porosity (32.93%) of 3D printed rock (sample 1 from Table 6.2) differed from the porosity of actual rock sample (the porosity was 24%) (shown in Table 6.1). This suggests that 3D printed rock has several defected regions which increases the pores area significantly. There are other reasons associated with change in porosity of 3D printed porous structures as compared to actual rock sample which are magnification of mesh file for 3D printing, cropping of actual segmented file for mesh file generation and trapping of a polymer layers within micropores while 3D printing. Currently, work to establish the impact of the model creation process on porosity is underway. Due to printing speed, printing resolutions and mesh magnification dissimilarity might happen in between the real

171

rock samples and 3D printed rock samples. The higher porosity obtained can be due to increase in internal defects and poor interlayer adhesion during 3D printing, which was also evident in the X-ray CT images of the sample (Figure 6.6).
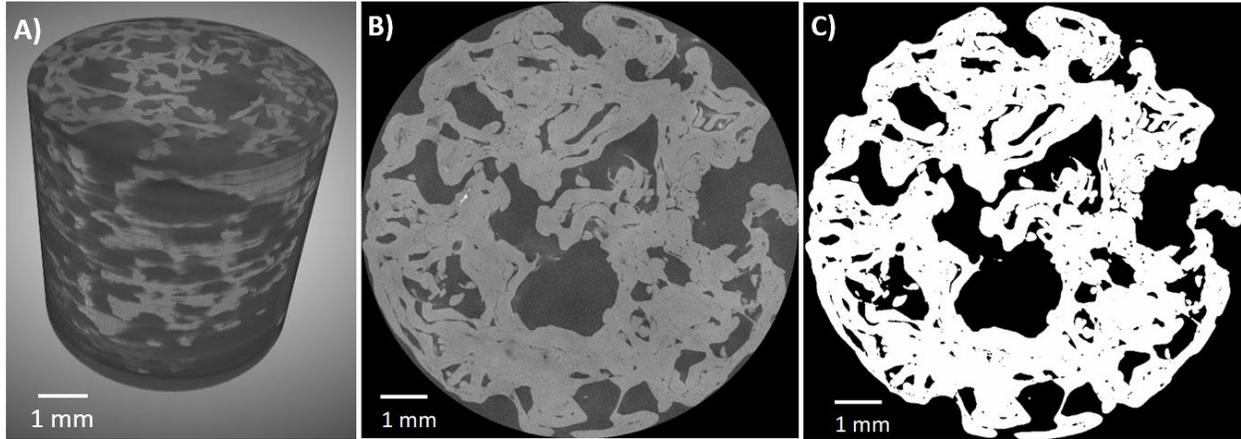
Figure 6.6. X-ray CT image of compiled 2D slices in 3D cylinder, B) X-ray CT image slice of 3D sample, C) X-ray CT image slice of 3D sample after segmentation. (Images collected by graduate student Abdullah Al Nahian, Dr. Lauren Beckingham research group).

Table 6.1. Sample Properties Calculated from the X-ray CT Images of the 3-D Printed Samples (Data generated by graduate student Abdullah Al Nahian, Dr. Lauren Beckingham research group).

Sample	Voxel resolution (µm)	Porosity
Bentheimer sandstone	3.998	24%
3D printed	17.97	32.93%

Therefore, the printing speed, resolution, extrusion temperature, bed temperature and mesh magnification parameters were used to obtain indistinguishable 3D printed rock samples from the real rocks (see Table 6.2). Minimizing the printing speed to 10 % and maximizing the printing resolution and optimizing mesh magnification resulted into better printing quality with minimal internal defects within grains and pores (shown in Figure 6.7). Sample 8, 9 and 10, with optimal 3D printing parameters showed better printability with minimum printing defects.

Table 6.2. 3D printing parameters to fabricate porous media specimens.

Sample No.	Measurement (X, Y, Z) (mm)	Magnification	Print size (X, Y, Z) (mm)	Resolution (μm)	Printing speed (%)	Extrusion Temperature (°C)	Orientation	Result
1	1.811, 1.3099, 3.6411	20X	36.22, 26.198, 72.822	100	60	225	Vertical	Moderate[1]
2	1.811, 1.3099, 3.6411	5X	9.055, 6.5495, 18.2055	100	20	225	Horizontal	Poor[2]
3	1.811, 1.3099, 3.6411	5X	9.055, 6.5495, 18.2055	100	10	225	Horizontal	Poor
4	1.811, 1.3099, 3.6411	60X	108.66, 78.594, 3.6411	100	10	225	Vertical	Stretched[3]
5	0.6423, 0.6409, 1.229	45X	28.9035, 28.8405, 55.305	100	10	225	Vertical	Moderate
6	0.6423, 0.6409, 1.229	45X	28.9035, 28.8405, 55.305	100	20	225	Vertical	Poor
7	0.6423, 0.6409, 1.229	20X	12.846, 12.818, 24.58	100	10	240	Vertical	Moderate
8	0.6423, 0.6409, 1.229	25X	16.0575, 16.0245, 30.7277	100	10	240	Vertical	Good[4]
9	0.6423, 0.6409, 1.229	20X	12.846, 12.818, 24.58	75	50	240	Vertical	Good
10	0.6423, 0.6409, 1.229	20X	12.846, 12.818, 24.58	75	10	240	Vertical	Good

[1] Moderate printability indicates some internal 3D printing defects within the grains and pores.

[2] Poor printability indicates maximum internal printing defects.

[3] Stretched print indicates improper mesh and size magnification of stl file.

[4] Good printability indicates minimal internal defects with less to no defects within the grains and pores.
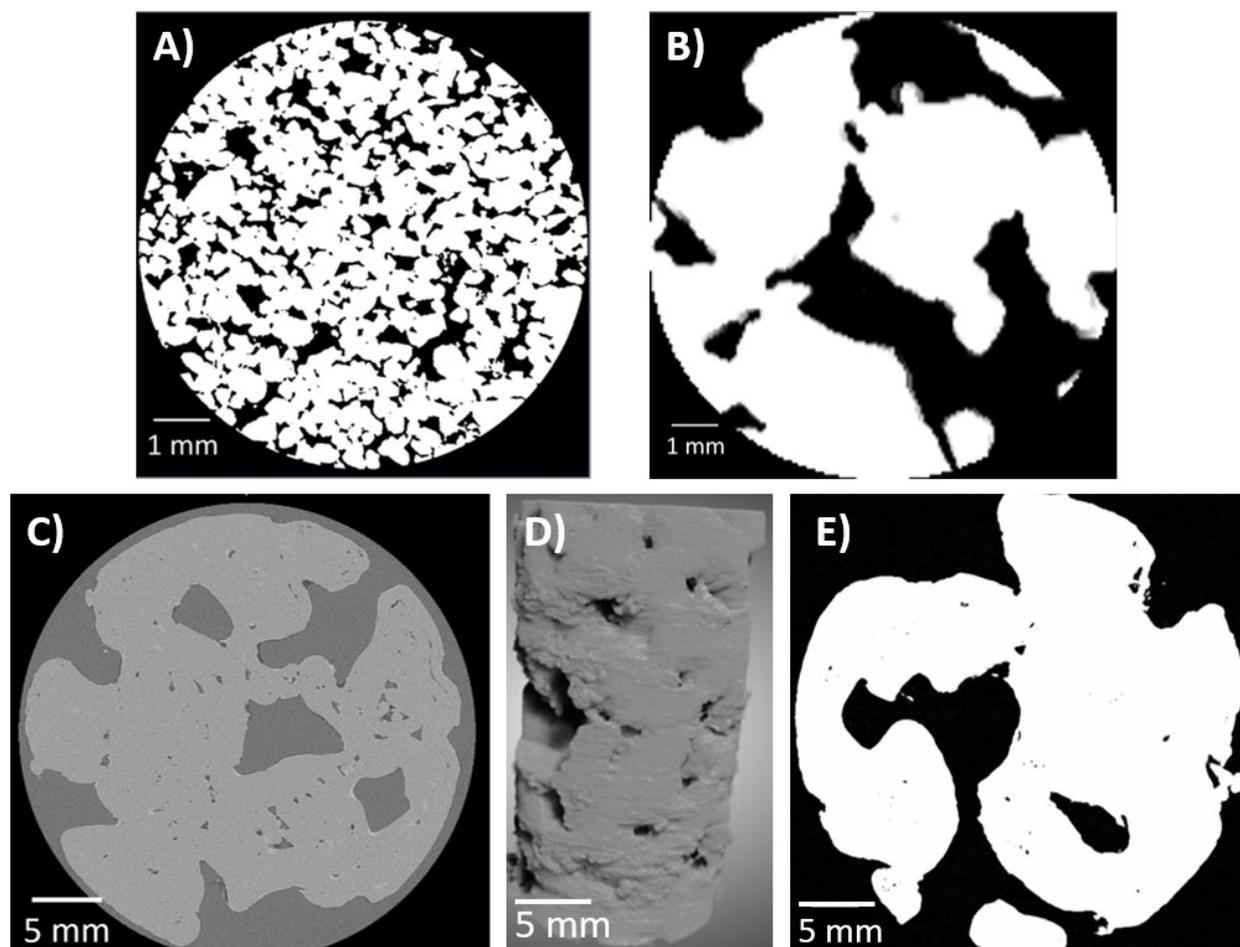
Figure 6.7. A) Thresholded X-ray CT image of Bentheimer sandstone with grains in white, B) cropped 3D X-ray CT image of Bentheimer sandstone with grains in white (thresholded), C) X-ray CT image slice of 3D sample (sample 9 from table 6.2), D) X-ray CT image of compiled 2D slices in 3D cylinder, and E) thresholded X-ray CT slice of 3D printed sample (Sample 9 from table 6.2). (Images collected by graduate student Abdullah Al Nahian, Dr. Lauren Beckingham research group).

6.4. Conclusion

This work investigates the viability of 3D printing samples to grow reactive minerals (calcite) and to reflect properties those of natural geochemical samples. Rock structure images with pore networks based on natural samples can be easily extracted from 3D X-ray CT images and serve as the basis for fused filament fabrication printing. Primarily, the goal of this work was to demonstrate the ability to grow calcite crystals on polymer surfaces This was investigated by using HIPS polymer and functionalizing the polymer surface by acid treatment. The calcite growth was then demonstrated by precipitation of calcite crystals on acid treated polymer surfaces. Fabrication and surface functionalization of 2D polymer films showed presence of polar groups (SO_3H). The capability of precipitating calcite on 2D reactive HIPS films and approach to enhance calcite crystal growth on polymer surface was also demonstrated. Through CT image analysis and image segmentation of sandstone sample scans, the mesh and 3D print replicate were created, that can be utilized in a series of replicate experiments to evaluate mineral dissolution and precipitation reactions with changing conditions. Besides, other petrophysical properties, such us connected pores, grain surface area, total accessible surface area and pore size distribution etc. will be determined in future work to better understand the properties of 3D printed rock samples.

6.5. References

[1] Valentová, A.; Bostik, V. Climate Change and Human Health. *Military Medical Science Letters (Vojenske Zdravotnicke Listy)* **2021**, *90* (2), 93-99. https://doi.org/10.31482/mmsl.2021.010.

[2] Malhi, Y.; Franklin, J.; Seddon, N.; Solan, M.; Turner, M. G.; Field, C. B.; Knowlton, N. Climate Change and Ecosystems: Threats, Opportunities and Solutions. *Philosophical*

Transactions of the Royal Society B: Biological Sciences **2020**, *375*, 20190104. https://doi.org/10.1098/rstb.2019.0104.

[3] Ozotta, O.; Ostadhassan, M.; Liu, K.; Liu, B.; Kolawole, O.; Hadavimoghaddam, F. Reassessment of CO2 Sequestration in Tight Reservoirs and Associated Formations. *Journal of Petroleum Science and Engineering* **2021**, *206*, 109071. https://doi.org/10.1016/j.petrol.2021.109071.

[4] Saran, R. K.; Arora, V.; Yadav, S. Co2 Sequestration by Mineral Carbonation: A Review. *Global Nest Journal* **2018**, *20*, 497-503 https://doi.org/10.30955/gnj.002597.

[5] Jessen, K.; Kovscek, A. R.; Orr Jr, F. M. Increasing CO2 Storage in Oil Recovery. *Energy Convers. Manag.* **2005**, *46* (2), 293–311.

[6] Bachu, S. Sequestration of CO2 in Geological Media: Criteria and Approach for Site Selection in Response to Climate Change. *Energy Convers. Manag.* **2000**, *41* (9), 953–970. https://doi.org/10.1016/S0196-8904(99)00149-1.

[7] Sadeq, Q. M.; Bin Wan Yusoff, W. I. Porosity and Permeability Analysis from Well Logs and Core in Fracture, Vugy and Intercrystalline Carbonate Reservoirs. *J. Aquac. Res. Dev.* **2015**, *6* (10), 1000371. https://doi.org/10.4172/2155-9546.1000371.

[8] Min, T.; Gao, Y.; Chen, L.; Kang, Q.; Tao, W. Changes in Porosity, Permeability and Surface Area during Rock Dissolution: Effects of Mineralogical Heterogeneity. *Int. J. Heat Mass Transf.* **2016**, *103*, 900–913.

[9] Moghadasi, J.; Müller-Steinhagen, H.; Jamialahmadi, M.; Sharif, A. Model Study on the Kinetics of Oil Field Formation Damage Due to Salt Precipitation from Injection. *J. Pet. Sci. Eng.* **2004**, *43* (3–4), 201–217. https://doi.org/10.1016/j.petrol.2004.02.014.

[10] Bin Merdhah, A. B.; Mohd Yassin, A. A. Scale Formation in Oil Reservoir during Water

Injection at High-Salinity Formation Water. *J. Appl. Sci.* **2007**, *7* (21), 3198-3207. https://doi.org/10.3923/jas.2007.3198.3207.

[11] Crabtree, M.; Johnson, A.; Eslinger, D.; Fletcher, P.; Miller, M.; Johnson, A.; King, G. Fighting Scale — Removal and Prevention. *Oilf. Rev.* **1999**, 30-45.

[12] Moghadasi, J.; Müller-Steinhagen, H.; Jamialahmadi, M.; Sharif, A. Prediction of Scale Formation Problems in Oil Reservoirs and Production Equipment Due to Injection of Incompatible Waters. *Dev. Chem. Eng. Miner. Process.* **2006**, *14* (3–4), 545-566. https://doi.org/10.1002/apj.5500140319.

[13] Revil, A.; Schwaeger, H.; Cathles, L. M.; Manhardt, P. D. Streaming Potential in Porous Media 2. Theory and Application to Geothermal Systems. *J. Geophys. Res. Solid Earth* **1999**, *104* (B9), 20033-20048. https://doi.org/10.1029/1999jb900090.

[14] Iloejesi, C. O.; Beckingham, L. E. Assessment of Geochemical Limitations to Utilizing CO_2 as a Cushion Gas in Compressed Energy Storage Systems. *Environ. Eng. Sci.* **2021**, *38* (3), 115-126. https://doi.org/10.1089/ees.2020.0345.

[15] Beckingham, L. E.; Winningham, L. Critical Knowledge Gaps for Understanding Water-Rock-Working Phase Interactions for Compressed Energy Storage in Porous Formations. *ACS Sustain. Chem. Eng.* **2020**, *8* (1), 2-11. https://doi.org/10.1021/acssuschemeng.9b05388.

[16] Ishutov, S.; Hasiuk, F. J.; Harding, C.; Gray, J. N. 3D Printing Sandstone Porosity Models. *Interpretation* **2015**, *3* (3), 49–61. https://doi.org/10.1190/INT-2014-0266.1.

[17] Almetwally, A. G.; Jabbari, H. 3D-Printing Replication of Porous Media for Lab-Scale Characterization Research. *ACS Omega* **2021**, *6* (4), 2655–2664. https://doi.org/10.1021/acsomega.0c04825.

[18] Almetwally, A. G.; Jabbari, H. Experimental Investigation of 3D Printed Rock Samples Replicas. *J. Nat. Gas Sci. Eng.* **2020**, *76*, 103192. https://doi.org/10.1016/j.jngse.2020.103192.

[19] Dalas, E.; Kallitsis, J.; Koutsoukos, P. G. The Crystallization of Calcium Carbonate on Polymeric Substrates. *J. Cryst. Growth* **1988**, *89* (2–3), 287–294. https://doi.org/10.1016/0022-0248(88)90412-5.

[20] Neumann, R.; Andreeta, M.; Lucas-Oliveira, E. *11 Sandstones: raw, filtered and segmented data*. **2020**.

Chapter 7

Summary and Future Work

Chapter 7. Summary and Future Work

This dissertation provided a comprehensive platform for extending the lifetimes of 3D printed materials by incorporating self-healing properties in polymer composites to advance the development of safer, reliable, long-lasting, low-cost, and sustainable polymer materials with a wide range of properties and functionalities. The complex nature of self-healing and 3D printing methods for polymer composites demands an understanding of multi-level molecular and macroscopic events. Different 3D printing technologies have found applications for the manufacturing of prototypes and customized functional parts for automobile, aerospace, electronics, and biomedical applications, and the use of 3D printing in industrial manufacturing is expected to increase as materials and methods advance. However, compared to parts fabricated by traditional methods, 3D printed composites typically show poorer mechanical strength and thereby increased potential for material damage and failure during fabrication and use. The key contributions of this work were the introduction of different polymer materials and research approaches for improving material durability, sustainability, chemistry, morphology, and processing for 3D printing of multi-functional and multi-phase systems and the practical utility of additive manufacturing technologies via a self-healing approach. It focused on fabricating self-

healing systems by using two dominant 3D printing techniques, i.e., fused filament fabrication (FFF) and stereolithography (SLA), via a microcapsule-based self-healing approach.

The key contributions of the stereolithographic (SLA) 3D printing of self-healing composites research were the first successful fabrication of SLA 3D printed self-healing composites based on microcapsule-catalyst autonomous self-healing, and enhanced understanding of self-healing mechanisms for microcracks recovery within 3D printed composite structures and ability of self-healing materials in retention of material matrix integrity towards preventing or delaying mechanical failure. Initial reports on 3D printing of self-healing systems involved using intrinsic physical and chemical properties of the matrix polymer or external triggers such as heat and light to initiate self-healing. A novel approach to capsule-catalyst based self-healing for SLA 3D printing overcame the initial challenges, such as dependency on the latent functionality of a polymer material for self-healing and limitations in using different chemistries of thermoset resins. The other challenges like uniform microcapsules distribution in the polymer matrix, recovery of brittle fractures, and negative impact of microcapsule addition on polymers' physical properties were overcome by uniform mixing of microcapsules and catalyst in polymer resin, the optimization of microcapsule size and concentration, and investigation of microcapsules' ability to recover microcracks at room temperature. Overall, this investigation presented SLA 3D printed self-healing composites based on microcapsule-catalyst autonomous self-healing and provided a promising and flexible approach for fabricating 3D objects with self-healing characteristics.

The second part of the research, self-healing of thermoplastic polymer composites, provided an understanding of the microcapsules filled with the non-toxic and environmentally friendly solvent, EPA, for developing sustainable self-healing of a thermoplastic polymer, high

impact polystyrene composites, through compression molding and fused filament fabrication. The key contributions of this research work were the utilization of low toxicity, non-genotoxic, green solvent, ethyl phenylacetate for investigating the self-healing in thermoplastic high impact polystyrene (HIPS) via a solvent-based self-healing approach. The challenges in FFF 3D printing as the relatively poor mechanical strength and weak interlayer adhesion between successive layers of FFF printed components leading to inaccessible damages within the polymer matrix were overcome by solvent-filled microcapsules integration within the HIPS polymer matrix and microcracks recovery with the solvent release at the crack site and interlocking cracked surfaces by the entanglement of polymer chains upon solvent diffusion. Overall, these FFF 3D printed self-healing composites presented solvent-based autonomous self-healing of up to 81% fracture recovery, illustrating their potential for extending the lifetime of FFF 3D printed composites. The preliminary research explored potential methods for maximizing healing efficiency and optimizing mechanical strength of FFF printed parts in the presence of microcapsules, but further improvement will be conducted in future research.

In the last portion of the dissertation, 3D printing of reactive porous media enhanced the understanding of geochemical reactions in porous media. Replication of natural samples using FFF 3D printing of thermoplastic polymer filaments provided a platform for replicating the physical, hydraulic, mechanical, and chemical properties of natural samples and understanding mineral dissolution and precipitation reactions in subsurface systems. The key contributions of this research were the ability to fabricate heterogeneous porous structures similar to original rock samples via FFF 3D printing and the utilization of polymer material design in optimizing mineral precipitation within porous structures.

Organization

In 7.1-7.3 sections of this chapter, overall work based on synthesis of microcapsules and its incorporation in different classes of polymer i.e., thermoplastics and thermoset polymers for construction of 3D printed self-healing composites is summarized and specific goals of future projects are discussed based on results and additional preliminary work. Section 7.4 of this chapter summarizes the results obtained so far and the suggestions for the future work. Lastly, section 7.5 summarizes broadly the research findings of the dissertation and describes how this work contributes to scientific advancement.

7.1. Stereolithographic (SLA) 3D printing of self-healing composites

In this study, we have shown SLA 3D printing of a self-healing composites through incorporation of monomer filled microcapsules into a thermoset resin matrix. We used commercial photo-resin to incorporate microcapsules for 3D printing application. Dicyclopentadiene (DCPD) monomer was used as the healing fluid in conjunction with Grubbs' catalyst due to its ability to polymerize at room temperature [1]. Resin formulations for SLA 3D printing were made with microcapsules concentration of 5 wt. % and catalyst concentration of 0.5 wt. %.

Self-healing composites printed by stereolithographic 3D printing showed positive results in terms of microcapsules survivability after 3D printing evaluated by TGA and ^{1}H-NMR and also in terms of recovery of mechanical properties such as fracture toughness and storage modulus. In TGA, a sudden drop in the sample mass near the boiling point of the healing fluid confirms the microcapsules survivability after 3D printing. The ^{1}H-NMR spectra of healing fluid extracted from crushed self-healing composites also confirmed this finding. Thermomechanical analysis of these

self-healing composites was performed by DMA to investigate effects of microcapsules on storage modulus and glass transition temperature and results showed that addition of microcapsules has a negligible effect on storage modulus and glass transition temperature of self-healing composites. However, more work on mechanical properties should be performed in future using three-point bending test (ASTM D790) to study effect of microcapsules in different wt. % on mechanical properties.

The fracture toughness and healing efficiency of microcapsules loaded composite materials were evaluated using the single-edged notched beam (SENB) test. From fracture toughness tests, it was observed that presence of microcapsules decreases fracture toughness value of composite material. This can happen as microcapsules act as voids or defects in a polymeric material. In fracture toughness test, after the damage event, composite materials containing 5 wt. % of microcapsules were allowed to heal for 24 hours and 48 hours. Although it was observed that self-healing composites with 5 wt. % of microcapsules showed maximum healing efficiency up to 73% after 2 days of healing.

In future, further investigation to improve healing efficiency of composite materials should be done by varying microcapsule and catalyst concentrations. Also, composite materials should be allowed to heal for different time periods (especially shorter times) to investigate healing behavior further. Towards the end, microcapsules with DCPD as a core agent has been fabricated via in-situ interfacial emulsion polymerization as explained in Chapter 3, and sieved in different sizes including 25 µm, 50 µm, 75 µm and 100 µm. Self-healing composite structures have been 3D printed via stereolithography using different microcapsules' size and concentration (0 – 10 wt.

%) and 0.5 wt. % of Grubbs' catalyst. Figure 7.1 shows particle size distribution of 4 different sizes of microcapsules synthesized.
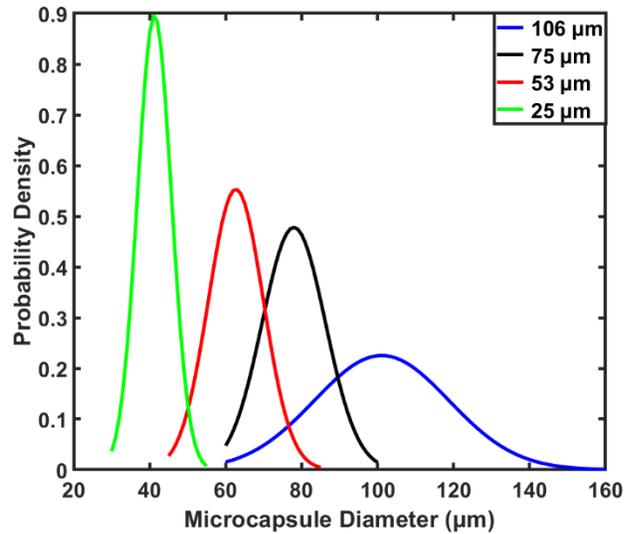
 Figure 7.1. Particle size distribution of DCPD filled microcapsules' representing different sizes.

These microcapsules with varied sizes and concentrations should be utilized in the future to investigate the following specific aims:

Specific aims

Investigation of how capsule content impacts mechanical properties and self-healing behavior. Impact of microcapsule content and size on mechanical properties should be examined using flexural strength, flexural modulus, and yield strength of composite materials by three-point bending test. To study role of capsule concentration on healing efficiency of composite materials, fracture toughness of self-healing composites using different wt.%. of monomer filled microcapsules such as 2.5, 5, 7.5 and 10 wt. % should be studied in order to determine whether increasing capsule concentration can achieve higher recovery of fracture toughness leading to

higher healing efficiencies and if this behavior has trade-offs with composite mechanical properties in general.

Investigate the role of catalyst concentration on healing efficiency of composite materials. Fracture toughness and flexural test of self-healing composites using different wt.%. of catalyst should be performed in order to ascertain whether increasing catalyst concentration can achieve higher recovery of fracture toughness leading to higher healing efficiencies or if catalyst concentration may be lowered (lowering cost) while achieving analogous healing efficiency.

7.2. Self-healing of High Impact Polystyrene Composites

7.2.1. Self-healing of High Impact Polystyrene composites fabricated by compression molding

This work investigated microcapsule-based self-healing of thermoplastic high impact polystyrene (HIPS) composites using a environmentally friendly solvent, ethyl phenylacetate (EPA). EPA was incorporated within double-walled polyurethane-poly(urea-formaldehyde) (PU-UF) microcapsules which were then integrated within the HIPS specimens. These self-healing polymer composites have the ability to intrinsically heal damage. TGA and ^{1}H-NMR spectroscopy analysis validated the presence of intact microcapsules in compression molded HIPS composites. Mechanical characterization via flexural and fracture testing reveals that the addition of microcapsules leads to a decrease in overall mechanical properties with increasing microcapsule content. However, increasing microcapsule content also results in increased healing efficiency, with up to 64 % recovery of the fracture toughness achieved at the higher microcapsule loading (7.5 wt.%). This demonstrates the tradeoffs for consideration when translating this approach to

target applications Therefore, there are still several unexplored tunable system parameters towards minimizing these losses in mechanical properties which can be optimized in the future. Overall, this work demonstrated inclusion of self-healing properties in a commercially important polymer material with a non-toxic and environmentally friendly solvent and motivates further development of thermoplastic self-healing composites for industrial applications. A similar approach is extended to FFF 3D printing of HIPS composites containing EPA filled microcapsules.

7.2.2. Fused filament fabrication of self-healing high impact polystyrene (HIPS) composites

In this study, we demonstrated FFF 3D printing of a self-healing composites through incorporation of solvent filled microcapsules into thermoplastic polymer matrices. We used high impact polystyrene (HIPS) the material of interest to incorporate microcapsules for 3D printing. HIPS is a low-cost material commonly used for 3D printing due its high impact strength and easy machinability and fabrication [2]. Ethyl phenyl acetate (EPA) was the healing fluid used for self-healing of HIPS composite materials due to its ability dissolve HIPS at room temperature as their solubility parameters are close to each other. The solvent-based healing approach was utilized for self-healing of thermoplastics as thermoplastic polymers in presence of solvent shows chain mobility for the solvent-welding mechanism.

A filament coating method was used to coat a thin layer containing microcapsules onto polymer filaments. One drawback of this method is the volatile solvent used to suspend the coating polymer and microcapsules which adds cost and environmental impact. Additionally, a large volume fraction of solvent can be required, and the fast evaporation rate of the solvent limits the use of the prepared polymer ink to a relatively short time period. An alternative method to

incorporate microcapsules into polymer matrices can be extruding them directly into polymer filaments with varied microcapsules content. Preliminary work on extrusion of filaments containing microcapsules showed that more microcapsule quantity is required to have microcapsules mixed throughout with HIPS pellets for extrusion. In application, this would add to cost, and in the lab scale experiment, it leads to the ability to produce smaller quantities of filament per microcapsule batch. Additionally, once the HIPS filaments with integrated microcapsules were extruded, single screw extrusion did not result in dispersing the microcapsules uniformly within the extruded HIPS filaments. Due to blending issues at the extruder scale when mixing HIPS pellets and microcapsules, much of the filaments produced had inconsistent microcapsule loading along their length and was not as circular in cross-section as commercial HIPS filament. Due to these challenges, microcapsule coating on the filament using polymer ink prepared in the solvent via a drawn coating approach was used to place microcapsules at the interlayers via 3D printing.

Preliminary work on self-healing of HIPS composites containing solvent-filled microcapsules showed positive results in terms of both microcapsules survivability after 3D printing evaluated by ^{1}H-NMR and TGA and in terms of recovery of fracture toughness evaluated by fracture test (ASTM D5045-14). Thermomechanical analysis of these self-healing composites showed that addition of microcapsules showed negligible change in the bulk storage modulus and glass transition temperature of the composite material. Three-point bending tests should be used in the future to characterize the mechanical properties including flexural strength, flexural modulus and young's modulus to understand the effect of different wt. % (0-10 wt. %) of microcapsules on composites' mechanical properties.

It was observed that the presence of microcapsules decreases fracture toughness of HIPS composites, analogous to the behavior observed in SLA printed composites. Self-healing composites with 7.5 wt. % microcapsules showed a maximum healing efficiency of 81 % after 72 hours of healing. Additional fracture toughness experiments should be conducted with varying microcapsules content to examine the relationships between microcapsule content, bulk mechanical properties, healing efficiency and healing time.

Potential specific aims of future work on these materials could include the following:

Specific aims

Investigate survivability of microcapsules in a melt extrusion method. Filament extrusion should be attempted varying the temperature and microcapsule concentration and survivability of microcapsules assessed by TGA and ^{1}H NMR experiments.

Impact of microcapsule concentration on mechanical properties of self-healing composite materials. Composites of varied microcapsule content can be prepared and tested for mechanical properties. The flexural strength, flexural modulus and yield strength of composite materials should be evaluated by flexural test.

Investigate role of self-healing microcapsule concentration on healing efficiency of composite materials. Varied microcapsule content such as 2.5, 5, 7.5 and 10 wt. % should be used in order to understand whether increasing capsule concentration could achieve higher recovery of fracture toughness leading to higher healing efficiencies.

7.3. Stereolithographic 3D printing of bio-based self-healing composites

As mentioned in Chapter 3, stereolithography is economical and simpler way to prepare composites using thermoset resin material. A preliminary study was done with commercial resin from the petroleum sources to prepare self-healing composites containing microcapsules and catalyst. Although SLA self-healing polymer composites showed positive results in terms of recovery of fracture toughness, they lack in a biocompatibility and renewability. Due to increase in the environmental pollution and carbon emissions, bio-based systems are one opportunity to decrease reliance on petroleum byproducts [3]. Also, fabrication of a biomedical devices or prototypes using 3D printing innovations is gaining an industrial attention [4]. SLA 3D printing of bio-based resin systems has been reported for biomedical applications [5-7]. Also, research in the field of bio-resins where acrylates are blended with the epoxy material synthesized from vegetable oil to make it eco-friendly have been reported [8]. Drawback of this process is, some of the epoxy networks remains uncured due to fast curing of acrylates that can affect the properties of the 3D printed materials. Moreover, the blend of epoxy and acrylate requires two initiators which can make the process costly and complicated for 3D printing application. Although 3D printing of bio-based self-healing composite materials has not been reported yet to best of our knowledge. Thus, in this study, acrylate-based bio-resins were tested for their potential application in 3D printing and self-healing.

Two different types of acrylates, isoboronyl acrylate and 1,10-decanediol diacrylate were purchased from Sartomer Co. Ltd. and used to make blends of different mole ratios (20:80, 50:50 and 80:20). The monomer and their blend viscosities were characterized using a conical plate geometry where viscosity measured as a function of shear rate shown in a Table 7.1. Viscosity

data of bio-resins samples showed Newtonian behavior where with increasing shear rate, viscosity was not changed. For stereolithographic 3D printing process, resin viscosity is an important parameter. Commercial resins for the Formlabs 3D printers have viscosities in the range of 1.6 and 7.3 Pa·s, respectively and for Anycubic 3D printers in the range of 150-300 MPa.s. From Table 7.1, resin blends viscosity is comparably very low; therefore, addition of a viscosity modifier such as an oligomer should be explored to increase resin viscosity prior to 3D printing.

Table 7.1 Viscosity data of uncured resin samples

Resin	Isoboronyl acrylate (wt. / wt. %)	1,10-decanediol diacrylate (wt. / wt. %)	Viscosity (η) (Pa.s)
Sample 1	100	0	0.0099
Sample 2	0	100	0.0077
Blend 1	20	80	0.0089
Blend 2	50	50	0.0084
Blend 3	80	20	0.0077

However, the ability to photo-cure these monomers was investigated by polymerization of thin films under a UV lamp (405 nm) with diphenyl (2, 4, and 6- trimethyl benzoyl) phosphine oxide (TPO) as a photoinitiator and 2, 5-bis (5-tert-butyl-benzoxazol-2-yl) thiophene (BBOT) as an optical absorber as shown in Figure 7.2A. A double layered film was also prepared to ascertain the compatibility of resin formulations for SLA 3D printing in a layer-by-layer fashion. FTIR of

uncured samples and cured films was performed to confirm consumption of the anticipated double

bonds during the curing process (Figure 7.2B).
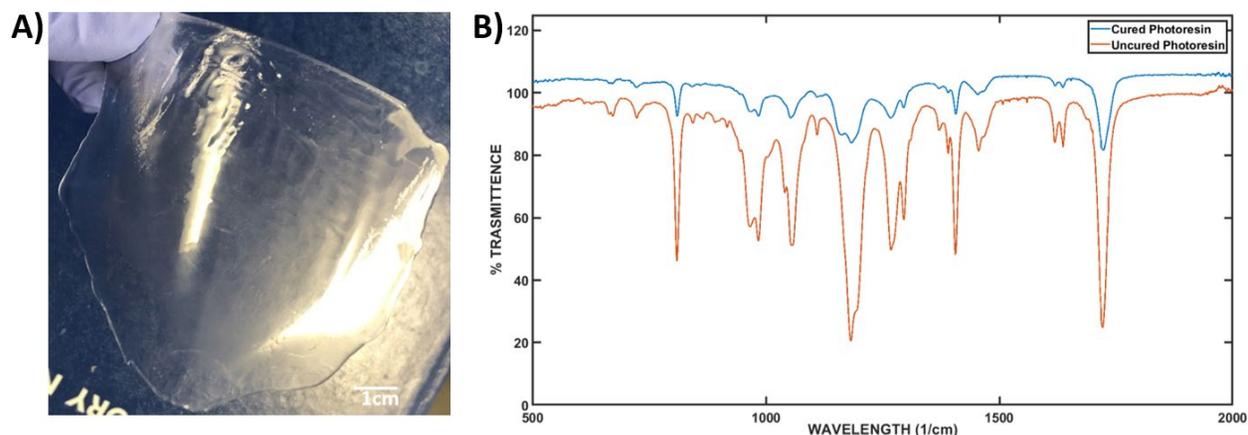
Figure 7.2 A) Photocured 2D film of bio-resin, B) FTIR spectrum of cured photoresin (blue), and

uncured photoresin (orange).

To extend this preliminary work towards development of biobased resins for vat 3D printing, the

following specific aims are suggested:

Specific aims

Improvement in the viscosity of resin blend. All formulations should demonstrate significant

viscosity and should be readily polymerizable by the UV-laser-based SLA process. High-viscosity

resins tend to lead to higher resolution. Cellulose based esters or acrylate-based oligomers of high

viscosities could be added to the resin blends to increase the viscosity of the resin formulation.

Investigation of mechanical properties of 3D printed photocured samples. SLA 3D printing

of bio-based resin formulations can be performed to prepare bars for mechanical testing. The

flexural strength, flexural modulus and yield strength of composite materials should be evaluated

by flexural test and results should be compared with mechanical properties of commercial ANYCUBIC resin and other commercial petrochemical-based resins.

Study mechanical performance of 3D printed photocured samples. Long chain oligomers (preferably bio-based) in different concentration should be added to bioresin formulations to enhance strength and elastic modulus of the 3D printed materials. Oligomers have higher C=C concentration as compared to monomer which provides higher crosslinking density after photocuring which can also improve the strength and modulus of 3D printed materials.

Investigate application of self-healing to photocured bio-based samples. Self-healing materials i.e., microcapsules containing one of the bio-resin as a core fluid can be synthesized. This embedded monomer can be able to use residual catalyst from the photocured resin for damage repair upon capsule burst. A multi-capsule-based system can also be studied where catalyst and core fluid are encapsulated separately if residual catalyst does not achieve maximum recovery of fracture toughness.

7.4. 3D Printing of Reactive Porous Media

This study was conducted in collaboration with Dr. Lauren Beckingham research and her group. A major goal of this project is to understand mineral dissolution and precipitation reactions and impacts on porosity and permeability in porous media using FFF 3D printing approach. However, to achieve that, the first objective of this research is to utilize 3D printing to fabricate reactive porous media and study the impact of variations in porous media structures and flow rates on where, within individual pores, mineral reactions occur and the corresponding change in porosity and permeability. This work investigates the viability of FFF 3D printing samples to grow

reactive minerals (calcite) and to reflect properties those of natural geochemical samples. Rock structure images with pore networks based on natural samples have been extracted from 3D X-ray CT images and serve as the basis for fused filament fabrication printing. A polymer suitable for 3D printing and precipitation of calcite crystals was found by fabrication of 2D polymer films and acid treating them to promote the growth of calcite crystals.

Fabrication and surface functionalization of 2D polymer films showed presence of sulfonic acid groups, verified by FTIR and ^{1}H-NMR spectroscopy. The capability of precipitating calcite on 2D reactive HIPS films and approach to enhance calcite crystal growth on a polymer surface was also demonstrated using FTIR, XRD, Nano CT and Optical Microscopy. Through CT image analysis and image segmentation of the sandstone sample scans, the mesh file was created, and replicates were 3D printed.

To extend these findings the following specific aims are suggested for future investigations:

Specific aims

Fabrication of reactive porous media. FFF 3D printing should be used to fabricate sets of physically replicate samples based on real porous media structures should be functionalized to promote calcium carbonate precipitation and used to investigate the growth of calcite within these specimens. Whole calcite growth on 2D films was represented that the complex flow experiment within the porous media may lead to differences across calcite growth experiments. 3D X-ray CT imaging should be used to examine the resulting precipitate growth and change in porosity in individual pores and pore-throats.

7.5. Contribution to Sustainable Polymer Composites

The dissertation discussed new design challenges and strategies for incorporating self-healing materials in 3D printed systems with better stability, higher reactivity, and faster kinetics. For instance, the capsule-catalyst based self-healing approach for SLA 3D printing showed the ability of the healing fluid (DCPD monomer) to quickly polymerize in the presence of catalyst after a fracture event at room temperature without external stimulus to recover structural function. In addition, self-healing systems (microcapsule-based self-healing) for 3D printing demonstrated in this dissertation involve targeted and uniform distribution of self-healing components for localized fracture recovery to maximize healing efficiency while minimizing cost and detrimental effects to the polymer matrix material. However, many challenges remain, for example, in terms of repeatability, reproducibility, and consistency in the 3D printed parts and comparative analysis with standard products based on accuracy and precision. This dissertation can help to point the reader and researcher in the directions these self-healing materials could follow in the future as it discusses the simplified approach in understanding these mechanisms. Finally, the outcomes and understanding of this dissertation provide insights into the material design for additive manufacturing of multi-functional and sustainable polymer systems. The 3D printing techniques and material chemistries studied in this research will deliver the foundation for developing large-scale economical, and durable 3D printed parts for industrial applications in the future.

7.6. References

[1]   Blaiszik, B. J.; Kramer, S. L. B.; Olugebefola, S. C.; Moore, J. S.; Sottos, N. R.; White, S. R. Self-Healing Polymers and Composites. *Annu. Rev. Mater. Res.* **2010**, *40*, 179–211. https://doi.org/10.1146/annurev-matsci-070909-104532.

[2]   Pi Chang, E.; Takahashi, A. Factors Influencing the Impact Strength of High Impact Polystyrene. *Polym. Eng. Sci.* **1978**, *18* (5), 350-354. https://doi.org/10.1002/pen.760180503.

[3]   Schuster, J.; Govignon, Q.; Bickerton, S. Processability of Biobased Thermoset Resins and Flax Fibres Reinforcements Using Vacuum Assisted Resin Transfer Moulding. *Open J. Compos. Mater.* **2014**, *04* (01), 1-11. https://doi.org/10.4236/ojcm.2014.41001.

[4]   Ramírez López, D. V.; Peña-Reyes, C.; Rojas, Á. J. Agent-Based Modeling of Mesenchymal Stem Cells on a 3D-Printed Bio-Device for the Regenerative Treatment of the Infarcted Myocardium. In *Proceedings - IEEE International Conference on Bioinformatics and Biomedicine, BIBM 2018*. https://doi.org/10.1109/BIBM.2018.8621314.

[5]   Voet, V. S. D.; Strating, T.; Schnelting, G. H. M.; Dijkstra, P.; Tietema, M.; Xu, J.; Woortman, A. J. J.; Loos, K.; Jager, J.; Folkersma, R. Biobased Acrylate Photocurable Resin Formulation for Stereolithography 3D Printing. *ACS Omega* **2018**, *3* (2), 1403-1408 . https://doi.org/10.1021/acsomega.7b01648.

[6]   Yu, R.; Yang, X.; Zhang, Y.; Zhao, X.; Wu, X.; Zhao, T.; Zhao, Y.; Huang, W. Three-Dimensional Printing of Shape Memory Composites with Epoxy-Acrylate Hybrid Photopolymer. *ACS Appl. Mater. Interfaces* **2017**, *9* (2), 1820-1829. https://doi.org/10.1021/acsami.6b13531.

[7] Melchels, F. P. W.; Feijen, J.; Grijpma, D. W. A Review on Stereolithography and Its Applications in Biomedical Engineering. *Biomaterials* **2010**, *31* (24), 6121–6130. https://doi.org/10.1016/j.biomaterials.2010.04.050.

[8] Lantean, S.; Roppolo, I.; Sangermano, M.; Pirri, C. F.; Chiappone, A. Development of New Hybrid Acrylic/Epoxy DLP-3D Printable Materials. *Inventions* **2018**, *3* (2), 29. https://doi.org/10.3390/inventions3020029.